



Norwegian University of Life Sciences
Faculty of Science and Technology

Philosophiae Doctor (PhD)
Thesis 2020:3

Chaos Enhanced Light Trapping in Optically Thin Solar Cells

Auka ljøsfanging med kaos i optisk
tynne solceller

Eivind Seim

Chaos Enhanced Light Trapping in Optically Thin Solar Cells

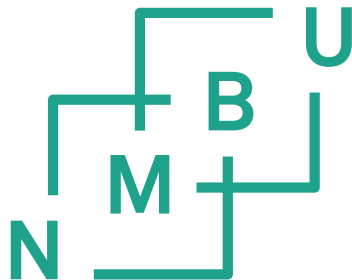
Auka ljoffangning med kaos i optisk tynne solceller

Philosophiae Doctor (PhD) Thesis

Eivind Seim

Norwegian University of Life Sciences
Faculty of Science and Technology

Ås 2019



Thesis number 2020:3

ISSN 1894-6402

ISBN 978-82-575-1670-3

“No human is limited”

—Eliud Kipchoge

Abstract

Photovoltaics is one of the most important sources of renewable energy. Solar cells with thin absorbing layers can be more cost-effective and leave a smaller environmental footprint than the current commercial technology. Light trapping is a key component for improving the absorption efficiency in thin solar cells. The longer the incoming light is trapped inside the solar cell, the greater is the chance of absorption. There are many approaches on how to trap light to achieve efficient management of light. The goals of the PhD project has been to perform ray and wave simulations on optically thin solar cell model systems to study their dynamics for improved absorption efficiency. The effect of chaotic scattering dynamics on absorption efficiency has been the central theme in this work. The dynamics of both classical ray chaos and quantum (wave) chaos have been studied in the context of improving light trapping in optically thin solar cells.

An exact ray formalism for stacks of one-dimensional absorbing planar films was developed. The formalism is equivalent with Maxwell's equations when phases are attached to each of the rays. Analytic expressions were derived for single film systems, and a hierarchical summation scheme was invented to correctly sum the truncated conditionally convergent sums necessary for multilayer film stacks. Some rays proved to be contributing more to absorption than others depending on the system. A Fourier transform of the reflection amplitude revealed the path length of the more contributing rays, from which their trajectories were deduced.

The classical ray dynamics in a surface structured solar cell model, the film+dome system, were studied using a tailor-made ray tracer code. The film+dome system was found to undergo a transition from regular to chaotic scattering dynamics as the index of refraction in the dome surface structure was increased past a certain value. The dynamics were characterized by the fractal dimension of its invariant set of long-lived trajectories. The transition to chaos was systematically accompanied with a rapid increase in the absorption efficiency, modeled with Beer-Lambert's law. This correlation was found to be structurally stable with respect to the film thickness.

The results from classical ray dynamics were confirmed in wave film+dome systems. Chaotic scattering dynamics were found in film+dome systems at refractive indices comparable to what classical ray simulations showed. Analogously to classical calculations, a structurally stable correlation between the absorption cross section and onset of chaotic behavior was demonstrated. In addition, the dwell time of rays were extracted from the scattering matrix, and was shown to correspond to increased ray lifetime, thus improved light trapping, at the onset of chaos.

Samandrag

Fotovoltaiske solceller er ei av dei viktigaste kjeldene til fornybar energi. Solceller med tynne absorberande lag kan vera meir kostnadseffektive og ha eit mindre miljøavtrykk enn gjeldande kommersiell teknologi. Ljosfangning er ein nøkkelkomponent for å forbetra absorpsjonseffektiviteten til tynne solceller. Jo lengre det innkomande ljuset er fanga inni solcella, jo større er sjansen for absorpsjon. Det finst mange tilnærmingar for å fanga ljøs for å oppnå effektiv ljøsstyring. Måla med PhD-prosjektet har vore å gjera stråle- og bylgjesimuleringar på modellsystem for optisk tynne solceller for å studera dynamikken deira for auka absorpsjonseffektivitet. Effekten av kaotisk spreingsdynamikk på absorpsjonseffektiviteten har vore eit sentralt tema i dette arbeidet. Dynamikken til både klassisk strålekaos og kvantekaos (bylgjekaos) har blitt studert i kontekst av å forbetra ljøsfanginga i optisk tynne solceller.

Ein eksakt stråleformalisme for stablar av eindimensjonale absorberande flate filmar vart utvikla. Formalismen er ekvivalent med Maxwells likningar når fasar er festa til kvar av strålane. Analytiske uttrykk vart utleia for enkeltfilmsystem, og ein hierarkisk summasjonsmetode vart laga for å summera avkorta summer som er konvergente på vilkår på korrekt måte, naudsynt for multilagssystem. Avhenging av systemet, så synte nokre strålar seg å bidra meir til absorpsjon enn andre. Ein Fouriertransformasjon av refleksjonsamplituden avdekte veglengda til dei strålane som bidrog mest, og frå dette blei strålebanane deira dedusert.

Den klassiske dynamikken i ein solcellemodell med overflatestruktur, film+kuppel-systemet, vart studert med ein skreddarsydd kode for strålesporing. Det vart funne at film+kuppel-systemet går over frå regulær til kaotisk spreingsdynamikk når brytingsindeksen i den kuppelforma overflatestrukturen vert auka over ein viss verdi. Dynamikken vart karakterisert med fraktaldimensjonen til det invariante settet av strålar med lang levetid. Overgangen til kaos var systematisk etterfylgd av ei rask auke i absorpsjonseffektiviteten, som var modellert med Beer-Lamberts lov. Denne korrelasjonen vart funnen til å vera strukturstabil med hensyn til tjukkeleiken til filmen.

Resultata frå klassisk stråledynamikk vart stadfesta i bylgje film+kuppel-system. Kaotisk spreingsdynamikk vart funnen i film+kuppel-system ved brytingsindeksar samanliknbare med det som vart funne i klassiske strålesimuleringar. Analogt til klassiske utrekningar, så vart det demonstrert ein strukturstabil korrelasjon mellom absorpsjonstverrsnittet og byrjinga av kaotisk oppførsel. I tillegg vart opphaldstida til strålane funnen frå spreingsmatrisa, og vart synt til å korrelera med auka levetid for strålane, og dermed forbetra ljøsfanging ved byrjinga av kaos.

Preface

The thesis presents an introduction to the papers and manuscript written during my time as a PhD student from 2016 to 2019 at the Norwegian University of Life Sciences (NMBU), REALTEK, in the group Biospec Norway. The PhD was funded by NMBU in support of the FRINATEK project “Development of a new ray model for understanding the coupling between dielectric spheres for photovoltaics with higher efficiency” - No: 250678 financed by The Research Council of Norway. The PhD has been supervised by main supervisor Achim Kohler together with Rozalia Lukacs, Reinhold Blümel, Erik Stensrud Marstein and Espen Olsen.

I consider the thesis and the work presented as a team effort. Without the team of supervisors it would not have been possible. I want to thank Achim Kohler for the supervision, knowledge and time that he has given to me. My time in the Biospec group has been fantastic. Not only have I learned a lot, but I have also been part of an incredibly inclusive group. I will always remember the times Achim has opened up his house or cabin for social events. My most sincere thanks for all the effort you have put in to make the group what it is.

I thank Rozalia Lukacs for the supervision and all the support she has given to me during my stay at NMBU. I have enjoyed the hikes we have had together with our families in Østfold and all over Connecticut. My thanks for the times you have been baby sitting Isaac cannot be expressed enough.

Reinhold Blümel is a physics encyclopedia in human form. His excellent ability to explain difficult concepts in simple terms is incredible. I thank him for the supervision, his great sense of humor and for the stays at Middletown, USA.

My two co-supervisors Espen Olsen and Erik Stensrud Marstein have helped the PhD project to have a connection to the real world with their vast knowledge about solar cells. This application has given an otherwise theoretical project more meaning. I am most thankful for the valuable input they have provided.

Maren Anna Brandsrud has been a fellow PhD student in the same NFR project as I have been. I am very grateful for all the discussions, suggestions, jokes and good times we have had together. We have often joked that we are each other’s “verge”. It has been a fun and challenging journey to do a PhD, and I am happy that we have shared all the ups and downs over the last years. My feet will never forget the 40000+ steps hike in San Francisco. Thank you for being an inspiration for me to become a more organized person!

I also want to thank the rest of the Biospec group for making my time at NMBU so pleasant. A special thanks goes out to my office buddies Maren Anna Brandsrud, Vlad Blazhko, Johanne Heitmann Solheim, Tiril Aurora Lintvedt, Gergely Kosa, and Aurora Rosvoll Grøndahl. It has been a pleasure to have shared office with

you.

I am grateful for my many friends. Their support through hardships and struggles has been very important to me. I want to thank Andrew Dibbs, Emilie Lund Johnsrud and Kyle Lapointe for countless hilarious moments and precious memories; Jozef Dzurenda, Simona Dzurendová and Johanne Heitmann Solheim for dinner parties, Overcooked and late night walks on campus; Kristian Kvamsøe, Nils Olav Hole, Rune Haugen and Sindre Gjerde for the time we shared in Trondheim and for really long gaming nights; the Moerveien gang for parties and color-changing tea; Sindre Lindheim-Minde and Knut Seim for our life-long friendship and to Åsmund Hommedal Blikås for always sending me something funny in our chat.

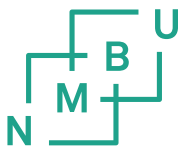
Running has become important to me for maintaining my sanity and not growing completely attached to my office chair. I want to thank Achim Kohler, Johanna Blomqvist, Anders Dahlberg and Boris Zimmermann for re-igniting the passion that I had for running, and for the adventures we have had participating in various races.

I want to give a huge thanks to Andrew Dibbs, Iselin Minde Kufoalor and Berit Hauger Lindstad for helping me with proofreading the PhD thesis.

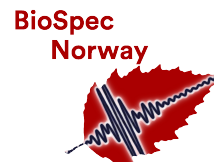
Finally, I want to thank my family for their support and the interest they show in what I do. The most special thanks goes to my wife Anja and son Isaac, who always cheer me up after a long day at work. I am grateful for having them to take my mind off work and making my life a lot more fun.

Eivind Seim

Ås, October 2019



Norwegian University
of Life Sciences



Contents

Abstract	i
Samandrag	iii
Preface	v
List of Papers	ix
Additional Scientific Work	x
List of Abbreviations	xiii
1 Introduction	1
1.1 Motivation	1
1.1.1 Light trapping for photovoltaics	1
1.1.2 Chaotic dynamics	3
1.1.3 Open questions	5
1.2 Objective	6
2 Theory and Methods	7
2.1 The photovoltaic effect and solar cells	7
2.2 Absorbing films in one dimension	9
2.3 Ray splitting in one dimension	11
2.4 Absorbing films with surface structures in two dimensions	12
2.4.1 The film+dome model system	13
2.5 Classical ray dynamics in two dimensions	14
2.5.1 Absorption efficiency	15
2.5.2 Fractal dimension of scattering fractals	17
2.6 Wave dynamics in the film+dome system	20
2.6.1 Exact wave solution for a planar film	21
2.6.2 Nearest neighbor eigenangle statistics	23
3 Results and discussions	25

3.1	Paper I	27
3.2	Paper II	29
3.3	Paper III	31
4	Conclusion	35
5	Further Research	37
	References	37
	Appendices	49
A	Paper I	49
B	Paper II	65
C	Paper III	79
	Errata	95

List of Papers

Paper I

- [1] M.A. Brandsrud, E. Seim, R. Lukacs, A. Kohler, E.S. Marstein, E. Olsen, and R. Blümel. Exact ray theory for the calculation of the optical generation rate in optically thin solar cells. *Physica E: Low-dimensional Systems and Nanostructures*, 105:125 – 138, 2019

Paper II

- [2] E. Seim, A. Kohler, R. Lukacs, M. A. Brandsrud, E. S. Marstein, E. Olsen, and R. Blümel. Chaos: A new mechanism for enhancing the optical generation rate in optically thin solar cells. *Chaos: An Interdisciplinary Journal of Nonlinear Science*, 29(9):093132, 2019

Paper III

- [3] E. Seim, A. Kohler, R. Lukacs, M.A. Brandsrud, E.S. Marstein, E. Olsen, and R. Blümel. Wave chaos enhanced light-trapping in optically thin solar cells. *Chaos: An Interdisciplinary Journal of Nonlinear Science*, submitted Oct 2019

Additional Scientific Work



Papers

- [4] M.A. Brandsrud, R. Lukacs, R. Blümel, E. Seim, E.S. Marstein, E. Olsen, and A. Kohler. An exact ray model for oblique incident light on planar films. work in progress
- [5] M.A Brandsrud, R. Lukacs, R. Blümel, E. Seim, E.S. Marstein, E. Olsen, and A. Kohler. Resonance structures in layers of planar films. work in progress






Conference Proceedings

- [6] E. Seim, A. Kohler, R. Lukacs, M.A. Brandsrud, E.S. Marstein, E. Olsen, and R. Blümel. Chaos: a new mechanism for enhancing the optical generation rate in optically thin solar cells. In Alexandre Freundlich, Laurent Lombez, and Masakazu Sugiyama, editors, *Physics, Simulation, and Photonic Engineering of Photovoltaic Devices VIII*, volume 10913, pages 213 – 221. International Society for Optics and Photonics, SPIE, 2019
- [7] M.A Brandsrud, R. Lukacs, R. Blümel, E. Seim, E.S. Marstein, E. Olsen, and A. Kohler. Optimized solar cells based on changes in resonance structure as a function of the refractive index and the thickness. In Alexandre Freundlich, Laurent Lombez, and Masakazu Sugiyama, editors, *Physics, Simulation, and Photonic Engineering of Photovoltaic Devices VIII*, volume 10913, pages 64 – 75. International Society for Optics and Photonics, SPIE, 2019

Oral Presentations

-  E. Seim, A. Kohler, R. Lukacs, M.A. Brandsrud, E.S. Marstein, E. Olsen, and R. Blümel. Wave chaos: A new mechanism for enhancing the absorption cross section of optically thin solar cells. Presented at: *Norwegian Solar Cell Conference* 2019-05-20–2019-05-21
-  M.A. Brandsrud, R. Lukacs, R. Blümel, E. Seim, E.S. Marstein, E. Olsen, and A. Kohler. Optimized solar cells based on changes in resonance structure as a function of the refractive index and the thickness. Presented at: *SPIE Photonics West* 2019-02-01–2019-02-06

Poster Presentations

-  M.A. Brandsrud, E. Seim, J.H. Solheim, R. Blümel, and A. Kohler. Does chaotic scattering affect the extinction efficiency in quasi-spherical scatterers? Presented at: *BioSpecMLC* 2019-04-18–2019-08-21
-  M.A. Brandsrud, R. Lukacs, R. Blümel, E. Seim, E.S. Marstein, E. Olsen, and A. Kohler. Two-dimensional ray theory for optically thin solar cells. Presented at: *Norwegian Solar Cell Conference* 2019-05-20–2019-05-21
-  E. Seim, A. Kohler, R. Lukacs, M.A. Brandsrud, E.S. Marstein, E. Olsen, and R. Blümel. Chaos: A new mechanism for enhancing the optical generation rate in thin-film solar cells. Presented at: *SPIE Photonics West* 2019-02-01–2019-02-06
-  E. Seim, A. Kohler, R. Blümel, M.A. Brandsrud, and R. Lukacs. Light trapping by structured surfaces in the regular and chaotic scattering regime. Presented at: *Norwegian Solar Cell Conference* 2017-05-09–2017-05-10
-  M.A. Brandsrud, A. Kohler, R. Blümel, E. Seim, and R. Lukacs. The importance of coupling between spheres for the efficiency enhancement of periodically structured solar cells. Presented at: *Norwegian Solar Cell Conference* 2017-05-09–2017-05-10

List of Abbreviations

E&M	Electromagnetic
FDTD	Finite-difference time-domain
GFM	Green's function method
GOE	Gaussian orthogonal ensemble
HSS	Hierarchical Summation Scheme
PSOS	Poincaré surface of section
PV	Photovoltaics

Chapter 1

Introduction

1.1 Motivation

Improving upon existing renewable energy technologies is considered to be of great importance in order to deal with ongoing climate change. In the European Union's 2030 climate and energy framework it is stated that the renewable energy target is at least 32% of the final energy consumption [15]. In 2017 the share of renewable energy was 17.5% in the EU energy mix, i.e. the share needs to almost double in the span of 13 years in order to reach the 2030 target. Photovoltaic solar cells (PV) are a renewable source of energy that has become increasingly popular. With efforts to decrease the PV production costs over the last decade, the average price of solar modules decreased from 2013 to 2018 by 61%, 50% and 34% in China, USA, and Germany, respectively [16]. The total installed PV energy production capacity increased from 40 GW_p in 2010 to over 500 GW_p in 2018 [17]. Today the share of PV is 4.3% of the total electricity demand in Europe and 2.6% globally.

1.1.1 Light trapping for photovoltaics

A plethora of different solar cell technologies and designs are being actively researched today. Solar cell technologies are often divided into three generations [18]. The first generation constitutes solar cells based on single-junction silicon technology. The second generation introduced the thin film solar cell concept which aims to lower the material costs [19]. The third generation aims to lower costs and to improve the conversion efficiency using advanced solar cell concepts such as multi-junction cells [20–23], hot-carrier solar cells [24], quantum dot solar cells [25], and intermediate band solar cells [26]. One especially interesting technology, which might not fit the usual generation classification, is solar cells based on perovskite materials [27]. Single-junction silicon photovoltaics is the most used technology today. The current record holding single-junction lab cell has a conversion efficiency of 26.7% [28, 29], which is close to the theoretical maximum of 29% determined by the Shockley-Queisser limit for single-junction silicon solar cells [30, 31]. It is therefore natural to look at cheaper alternatives or alternatives with higher potential efficiency. Both are necessary to reach the 2030 EU goal of having 32% PV in the energy mix. If solar cells are to become cheaper, more efficient and faster to produce, new technology needs to be developed. One interesting approach, which

is based upon existing silicon wafer technology, is the combination of a silicon solar cell with an additional, often thin, film structure on top to form a multijunction cell [32–34].

Making optically thin solar cells, including thin films, is an attractive approach to producing cheaper and more efficient solar cells. For starters, thin solar cells require less materials. A reduction of material is important, even for solar cells based on silicon, which is the second most abundant element in the Earth’s crust. Before being used in solar cells, silicon needs to go through an extensive purifying process. Solar cell grade silicon needs to be of at least “4N” purity, which means $10^{-4}\%$ or less impurities. All contaminants present in the silicon crystals contribute to a lower conversion efficiency. Producing such high-purity silicon requires a large amount of energy. Thus, lower material usage is an advantage of thin solar cells. There are also performance advantages to thin solar cells. Less bulk volume mean less bulk recombination of electron-hole pairs. Lower recombination rates yield in return higher open-circuit voltages [35]. Thin films are also in many cases flexible which potentially enables greater design freedom and creativity for engineers and designers when it comes to implementing solar modules in curved structures, building facades and roof tiles.

However, there are considerable challenges of thin film technology that need to be overcome. In general, the absorption of light in a solar cell is a function of its thickness. Rays of light incident on a solar cell need to enter and stay inside long enough to be absorbed. By reducing the thickness of the cell, the average path length, i.e. lifetime, of the rays is reduced, thus the ability to absorb photons is also reduced. This is especially important for crystalline silicon PV and other PV materials with an indirect bandgap, which has lower absorption coefficients [36] than materials with a direct band gap. Smart light management is therefore needed to keep the conversion efficiency high. Conventional “thick” solar cells may also benefit from improved light management, since reflection of rays from the front side is known to cause a loss of efficiency.

The idea of trapping light to enhance absorption in solar cells dates back to the 1970s [37] by taking advantage of the fact that light can be totally reflected when it strikes an interface at an angle greater than some critical angle. The escape cone is twice the critical angle which is dependent on the relative index of refraction across the interface. Light rays with long path lengths, thus long lifetimes, are desired. If the likelihood of total reflection is maximized, the average path length of the light rays is increased. This can be achieved by shaping the geometry of the front, back or both surfaces of the solar cell. Light trapping has been treated in the ray optics paradigm or “ray picture” in many publications [38–44]. However, ray optics is only a valid approximation in the short wavelength limit where the geometry is much larger than the wavelength of the light. Therefore, different methods are used in the light trapping literature depending on the size scale. For extremely thin solar cells on the nanoscale, or when nanoscale structures are used, full-field electromagnetic simulations are used [45]. Using thin films that are on

the order of tens of nanometers, may seem counterproductive since absorption efficiency decreases together with the film thickness. However, it has been shown that by increasing the local density of optical states in the absorber material, the ray optics trapping limit can be exceeded, even with ultrathin absorbers [46–48]. Nanoscale structures, usually called nanostructures, are a key factor to realize this potential [49]. Nanostructures have been subjected to numerous experimental and computational studies. Grandidier [50, 51] et al. have shown how whispering gallery modes can be employed to significantly increase absorption in a-Si thin film solar cells by placing resonant SiO₂ spheres on top of a solar cell. Garnett *et al.* has demonstrated large-area fabrication of silicon nanowire arrays with radial p-n junctions [52].

Creating random, or irregular, surface structures is a common approach for enhancing light trapping. Solar cells based on commercial technologies use chemical etching techniques to produce irregular pyramid textures for light trapping and anti-reflection [53]. Irregular needle structures have seen great success in reducing reflectance with “black silicon” being a prime example [54, 55]. The name lends itself to the excellent anti-reflectance capabilities which makes silicon look pitch black. Reflectance values as low as 0.1% have been reported using silicon nanowires arranged in a random fractal geometry for specific wavelengths and under 1% in the 200 nm to 700 nm range [56]. However, even though the world record holding solar cells use random structures, some reports claim that periodic structures may outperform random structures [38, 57].

Let us return to the ray optics regime and consider light impinging orthogonally on the surface of a planar slab material with index of refraction n . Yablonovitch showed in 1982 that the incoming light intensity is increased by a factor $2n^2$ on the inside if the planar slab is replaced by an ideally textured optical medium [58]. Inside such an ideally textured slab of material the directions of the light rays will be fully randomized and the system is called ergodic. However, a rigorous proof that certain solar cell geometries are ergodic has not been given in the PV literature. Recently, initial experimental and computational results have been reported which claim that intermittent chaotic rays lead to optically ergodic systems. The systems were cylindric and half-cylindric photonic plates [59, 60].

1.1.2 Chaotic dynamics

The discovery of the modern chaos theory is usually credited to Edward Lorenz. In his quest to predict the weather, Lorenz found that the behavior of his mathematical models is strongly dependent on the initial conditions of his calculations. This is the essential ingredient of chaos in dynamical systems. In 1972, Lorenz gave a talk titled “Predictability: does the flap of a butterfly’s wings in Brazil set off a tornado in Texas?”. Lorenz’s discovery has famously become known as *the butterfly effect* and is cited frequently in many contexts from popular science to

popular culture, including the movie Jurassic Park from 1993. The development of what we today refer to as chaos, or chaotic dynamics was lead by three important problems: The three-body problem, studied by Henri Poincaré for his winning entry in the 1890s prize competition in honor of Swedish King Oscar II [61, 62], the ergodic hypothesis from Ludwig Boltzmann’s work on statistical mechanics which was later proved by Von Neumann [63], and Lord Rayleigh’s nonlinear oscillators for modeling musical instruments [64].

The ergodic hypothesis lead the scientists at the time to look for ergodic mechanical systems. In 1898 Jacques Hadamard showed that the dynamics of balls on a Hadamard billiard, a surface of constant negative curvature, is everywhere unstable [65]. Later, in 1963, Yakov Sinai introduced *dynamical billiards*. The Sinai billiard is a square box with hard walls with a circular hard wall in the middle. The dynamics of the system is described by the movement of a frictionless particle which bounces around while obeying the reflection law. Sinai proved that the Sinai billiard is ergodic for most initial conditions, becoming the first to ever show the ergodicity of a dynamical billiard [66]. Leonid Bunimovich, who completed his PhD under Sinai’s supervision, studied a special dynamical billiard which bears his name, the *Bunimovich stadium*. He proved that its dynamics is chaotic [67–69]. We shall later see the relevance that the Bunimovich stadium has to light trapping and absorption enhancement in solar cells.

The trajectories of classical dynamics, often called orbits, are deeply linked to quantum mechanics. The old “planetary” quantum mechanics of Bohr, which was so successful for the spectrum of the hydrogen atom, failed when applied to the helium atom. However, when Wintgen *et al.* incorporated the semiclassical ideas developed by Gutzwiller in the 1960s, the helium atom was correctly quantized without the use of the new quantum mechanics of Heisenberg, Schrödinger, Born, and others [70, 71]. Gutzwiller was able to show that quantum systems whose classical counterparts are chaotic, can be quantized by a sum over classical periodic orbits [72–76]. This is known as the Gutzwiller trace formula. It has had a big impact on the development of periodic orbit theory.

Quantum chaos is the study of chaos in dynamical systems which are governed by wave equations. For that reason it is also referred to as wave chaos. Random matrix theory is a central tool in the field developed by Dyson, Metha, and others including Wigner who applied it to his studies on the chaotic energy spectra of heavy atomic nuclei [77–80]. It has been shown that the statistics of nearest neighbor eigenvalues of a certain class of random matrices known as the Gaussian orthogonal ensemble (GOE) follows the same distribution [81, 82]. This distribution is often called the Wigner surmise. Bohigas, Giannoni, and Schmit conjectured that all chaotic systems follow the Wigner surmise [83]. This conjecture has become a very important diagnostic tool in quantum chaos, and plenty of evidence in support of the conjecture exist [79, 80, 84]. The conjecture is therefore widely accepted by the community. Using these tools provided by random matrix theory, the phenomena of quantum chaos have been studied in a variety of physical sys-

tems including water waves [85], vibrating plates [84] and blocks [86], microwave resonators [87], and micro disk lasers [88].

Classical chaotic scattering is defined by the existence of a chaotic repeller, also called the invariant set, the set of all trajectories with infinitely long lifetime [89,90]. In scattering systems described by rays, such as scattering in geometrical optics, these trajectories represent rays that never exit the system. Due to time-reversal symmetry, such rays can not enter the system either. However, rays which come close to the chaotic repeller tend to stick to it, and may spend a long time to escape [91,92]. Moreover, it has been found that the geometry of the chaotic repeller is fractal [93–95]. Chaotic scattering systems have been studied in the context of both classical and wave chaos [84,96–99]. Semiclassical methods have also been applied to scattering systems [100,101].

Scattering systems which involve layered materials, have boundaries between media with different refractive indices. Rays incident on such boundaries, or interfaces, can split into two or more rays [102,103]. Ray splitting systems have been discussed extensively for stepped billiards and been important to the discussion in quantum chaos [104–106]. It has been found that the effects of ray splitting need to be taken into account in Gutzwiller’s trace formula [102]. Experimental studies have shown how classical ray splitting trajectories manifest themselves in wave systems [103]. Ray splitting affects the nearest neighbor level statistics in wave systems [107]. It was shown for a certain system that the inclusion of ray splitting shifts the spectral statistics towards GOE statistics, conjectured to be present in chaotic systems. In the absence of ray splitting, the statistics was found to be between GOE and the Poisson distribution.

1.1.3 Open questions

It is integral to have knowledge about the relevant physical principles and mechanisms to produce and optimize highly advanced devices such as solar cells. One route of optimization is creating light trapping structures. Gaining new understanding on how to exploit known physical principles to improve light trapping is highly beneficial to guide the design process that is necessary to do optimizations. The fields of light trapping in solar cells and chaotic dynamics have clear overlapping areas, with perhaps the most obvious overlapping concept being the dynamics of scattering rays.

Solar cells are essentially a type of scattering systems where the goal is to maximize the conversion of incident energy to electrical current. Light trapping is paramount to achieve this, especially for optically thin solar cells. Existing literature shows that the presence of long-lived rays which disperse exponentially fast away from each other is a property of chaotic scattering systems. The nature of such rays are therefore very interesting for improving the light management of solar cells. Rays are fast to compute and intuitive to analyze, whereas wave calculations are often

slow and sometimes completely unfeasible, e.g. for structures with simultaneously small and large features. It would be of great interest to see what the trajectories of the most important rays with respect to energy conversion in solar cells look like. Moreover, can ray splitting rays be used to calculate optical properties for size scales below the geometrical optics limit? Can ray models be exact regardless of the scale of the problem at hand? Ergodicity is a central concept in the theory of chaos in dynamical systems, making a link between the importance of ergodic scattering for light trapping and chaos theory. This link begs the question which is also the central theme of this PhD project: does the presence of chaotic scattering enhance the light trapping properties in solar cells? To answer this question, the dynamics of both rays and waves needs to be investigated.

1.2 Objective

The objective of this thesis is to demonstrate that chaotic scattering is important for the absorption efficiency in solar cells, using both ray and wave dynamics. This effort is broken up into three smaller tasks. The results of these tasks are reported in the format of research papers, two of which are already published in the scientific literature. Each task corresponds to a paper (two published, one submitted for publication) which is referred to by a roman numeral according to Sec. *List of Papers*.

- I** Develop an exact ray theory for solar cell models consisting of a stack of planar absorbing films to gain insight about the importance of the different rays in such systems. An exact ray theory for absorption in solar cells, i.e. absorbing dielectric films, does not exist. Such a theory can be developed using ideas from semiclassics and can be validated by comparison with Maxwell's equations for electrodynamics.
- II** Demonstrate classical chaos in a model solar cell with surface structure and prove that the absorption efficiency is enhanced and correlated with the onset of chaotic scattering. A model system is needed where the dynamics can be changed with a system parameter from regular to chaotic.
- III** Demonstrate presence of wave chaos, enhancement of absorption efficiency, and the correlation between the two. Classical chaos in a dynamical system does not necessarily imply wave chaos in an equivalent system for waves. This requires investigation of the same solar cell model system with the same surface structure as in the previous task.

Chapter 2

Theory and Methods

This chapter introduces the theoretical concepts and methodology central to the papers of this thesis. It serves as an introduction without going into the results and details which are presented in the papers. It is also meant to help the reader see the connection between the topics and give the reader some basic knowledge of how current is generated in a solar cell. For a complete introduction to solar cells, see Nelson's book [108].

2.1 The photovoltaic effect and solar cells

The photovoltaic effect was first discovered by Edmond Becquerel in 1839. When light shines on solar cells, electrical current is generated through the photovoltaic effect. There are three essential mechanisms taking place in the generation of current in a solar cell. These are the generation, separation, and collection of electron-hole pairs. The electronic band structure of solids can include a range of energy called the energy gap, E_g , where the valence and conduction bands are separated. Under ideal conditions no electron states exist in the energy gap, although impurities and certain material configurations, such as in intermediate-band solar cells [109], introduce intentional electron states in the energy gap region. The energy gap is central to the current generation in solar cells.

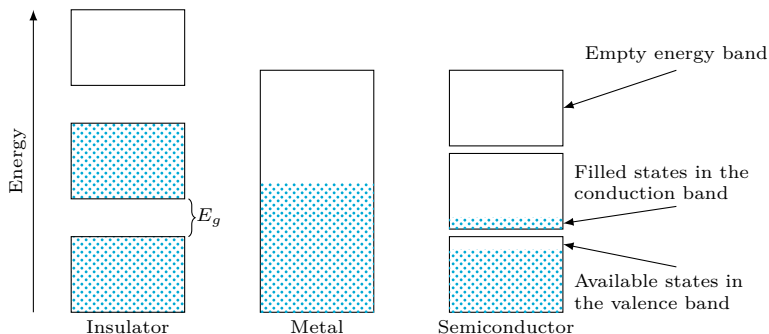


Figure 2.1: Schematic of the filling of the electron band structure in insulators, metals and semiconductors. Figure adapted from Kittel [110].

Figure 2.1 shows a schematic presentation of the electron structure of insulators, metals and semiconducting materials. The band structure of available electron states explains some of the properties of solids. The filled bands and large E_g of insulators make them poor conductors, and vice versa the partially filled bands make metals excellent conductors. Semiconductors suitable for solar cell applications, such as silicon, have an energy gap small enough for light in the visible spectrum to excite electrons from the valence band to the conduction band. Assume a monocrystalline slice of silicon where the individual Si atoms form covalent bonds with each of their four neighbors, see Fig. 2.2a. These covalent bonds can be broken by photons with energy larger than E_g . An electron-hole pair, which is free to move about in the crystal lattice, is generated when a bond is broken.

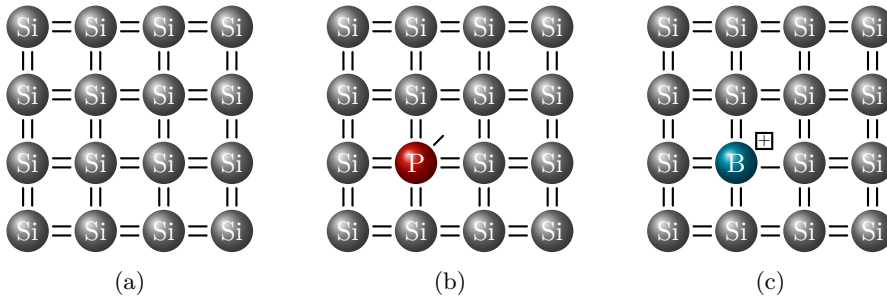


Figure 2.2: a) A two-dimensional projection of monocrystalline silicon. The black lines represent the sharing of electrons in covalent bonds between the atoms. b) Phosphorus atoms bring an extra electron to the silicon crystal. c) Boron atoms have one electron less than the surrounding silicon crystal, thus they bring an electron vacancy.

To generate current, the electron-hole pair must be separated and collected. The separation mechanism is made possible by introducing dopant elements in the Si crystal. Phosphorous and boron are popular choices for silicon solar cells. Phosphorous has an extra valence electron compared to silicon, see Fig. 2.2b, while boron lacks an electron, see Fig. 2.2c. The “lack” of an electron is an electron vacancy called a “hole”. For all practical purposes holes are pictured to move around in the silicon lattice as a positively charged particle would do. When a phosphorous doped (N-type) slice of silicon is joined together with a boron doped (P-type) slice of silicon to form a P-N junction, the extra electrons and holes recombine as shown in Fig. 2.3. The recombination depletes a region in the middle of the P-N junction of charge carriers, hence the name depletion region. Since the dopant cores are fixed to the lattice, the depletion region is unevenly charged and an electric field is formed across it. The electron-hole pair is separated by the electric field which sends electrons to the N side and holes to the P side of the junction. If contacts are not attached, i.e. the cell is an open circuit, a charge gradient is built up over the P-N junction. The electrons and holes seek to recombine, but recombination is prevented by the electric field over the depletion region. When contacts are then attached, charges have a new route to each other and electrical

current flows through the circuit system.

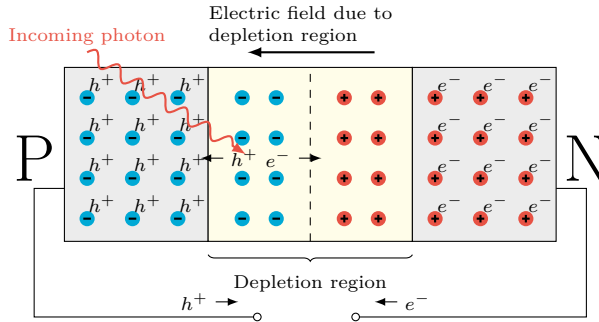


Figure 2.3: Schematic of how a simple photovoltaic device works under illumination. An incoming photon is absorbed and creates an electron, e^- , and a hole, h^+ , in the depletion region between a p-doped and n-doped semiconductor. The two particles are separated and electrical current can be extracted from the device.

A solar cell is a complex device with numerous material interfaces, contacts for extracting electricity, and antireflection coatings to protect the cell from the environment. To model solar cells in full is therefore a very challenging undertaking. There are also a great number of relevant solar cell designs and architectures. Choosing a particular one for this study could be interesting, albeit somewhat arbitrary. For the task at hand, namely to investigate the absorption and light trapping properties of solar cells with surface structure, it is instructive to create a general and simplified model. By collapsing the layers in Fig. 2.3 and adding an ideal backside mirror to completely remove transmission losses, we get a more manageable model with one layer that is characterized by its complex index of refraction. Section 2.2 presents such flat models without surface structure in one dimension, and section 2.4 presents two-dimensional models with a light trapping surface structure.

2.2 Absorbing films in one dimension

Maxwell's equations of electrodynamics can be used to calculate the optical scattering of a wave traveling through a given system or give expressions for optical properties such as reflectance. In one-dimensional systems the same expressions can be achieved using one-dimensional scalar waves, i.e. waves without polarization. Quantum mechanics is one of the most important areas of application of scalar waves. In other words, there is an equivalence between Maxwell and quantum mechanics in one-dimensional wave systems. Assuming a film made of a light absorbing material, its *absorption efficiency* can be expressed in the following way: the total incident intensity, normalized to unity, minus the fraction of reflected and

transmitted intensity

$$\sigma = 1 - R - T. \quad (2.1)$$

The transmission loss T can be eliminated by equipping the film with a perfect backside mirror

$$\sigma = 1 - R. \quad (2.2)$$

The reflectance R can be calculated for a single film with a perfectly reflecting back-mirror by considering a wave e^{ikx} with wave number k , coming in from the left and the quantum mechanical continuity conditions

$$\psi_1(0) = \psi_2(0), \quad (2.3a)$$

$$\frac{\partial}{\partial x} \psi_1(0) = \frac{\partial}{\partial x} \psi_2(0), \quad (2.3b)$$

where $x = 0$ is at the air-film interface, i.e., between region I and region II as seen in Fig. 2.4. In addition,

$$\psi_2(m) = 0, \quad (2.4)$$

is imposed at the location of the back-mirror, $x = m$, making it a perfectly reflecting mirror.

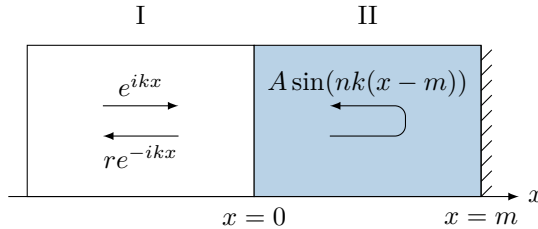


Figure 2.4: A model of an absorbing film with an air-film interface at $x = 0$ and a perfectly reflecting mirror at $x = m$.

Consequently, the wave functions in region I and II are

$$\psi_{\text{I}} = e^{ikx} + re^{-ikx}, \quad x \leq 0 \quad (2.5a)$$

$$\psi_{\text{II}} = A \sin(nk(x-m)), \quad 0 \leq x \leq m \quad (2.5b)$$

where n is the complex index of refraction in region II. Region I is air, with index of refraction equal to 1. The reflection amplitude r and factor A are found by applying the continuity and back-mirror conditions:

$$r = \frac{n \cos(nkm) + i \sin(nkm)}{n \cos(nkm) - i \sin(nkm)}, \quad (2.6)$$

$$A = \frac{2n}{\sin(nkm)[i \tan(nkm) - n]}. \quad (2.7)$$

The fraction of reflected intensity is obtained from the reflection amplitude,

$$R = |r|^2 = \left| \frac{n \cos(nkm) + i \sin(nkm)}{n \cos(nkm) - i \sin(nkm)} \right|^2. \quad (2.8)$$

In this model, Eq. (2.8) takes absorption into account via the imaginary part of the complex index of refraction, n . In the case of a system with a real index of refraction, R would naturally be equal to 1 due to no absorption in the material model. The imaginary part of the index of refraction models the total absorption. There is no discrimination between where the energy goes after it has been absorbed. This is an important note to make in the context of solar cells as not all absorbed energy contributes to the electrical output. However, the absorption efficiency is still an important figure of merit that should be optimized.

2.3 Ray splitting in one dimension

The absorption efficiency σ can also be derived analytically by considering rays carrying phase information. Contrary to the rays used in geometric optics, which are an approximation where the wavelength is short compared to its surroundings, the rays presented here are fundamentally different. By attaching phases to the rays, interference effects are included in the model and the analytic expression in Eq. (2.6) is recovered. Consider a single absorbing film with a perfect back-mirror. Incident rays partially transmit and partially reflect at the air-film interface at $x = 0$, and totally reflect at the mirror. At the interface, the ray can get reflection amplitudes r_l and r_r , and transmission amplitudes t_l and t_r depending on the direction of travel (subscript r to the right and subscript l to the left). At the mirror, the ray acquires a 180° phase shift. The reflection and transmission amplitudes are derived by using the continuity of the wave function which describes the wave dynamics inside and outside of the film. The procedure of deriving these amplitudes is described in detail in Appendix A of Paper I. The phenomenon of partial transmission and reflection of light is also called ray splitting. The ray dynamics literature refers to rays which split as *non-Newtonian* and their non-splitting counterparts as *Newtonian* [111].

The three simplest rays in a system consisting of a single film with thickness a , index of refraction n , and a reflecting backside mirror are shown in Fig. 2.5.

Their contributions yield a crude approximation to the total reflection amplitude

$$r \approx r_l + t_l e^{2inka} e^{i\pi} t_r + t_l e^{4inka} e^{2i\pi} r_r t_r, \quad (2.9)$$

where the first, second and third term correspond to the ray in Fig. 2.5a, 2.5b and 2.5c respectively. Adding more rays improves the quality of the approximation. It

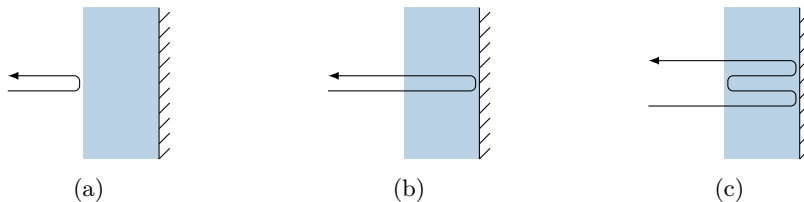


Figure 2.5: The three shortest rays in the system consisting of a single film with a backside mirror.

is straightforward to sum all possible rays in single film systems to get the exact reflection amplitude

$$r = r_l + t_l t_r e^{i\pi} e^{2inka} \sum_{\nu=0}^{\infty} (e^{i\pi} r_r e^{2inka})^{\nu}. \quad (2.10)$$

After evaluating the geometric series, the expression equates to the analytic expression in Eq. (2.6). It means that if all rays are accounted for, and present in the sum, the result is no longer only an approximation, but is exact.

For multilayer structures, it is not so easy to count all rays in this manner. One might be tempted to think that a possible solution would be to organize “families” of rays to help counting them. Each family could contain all combinations of rays with N hits on the back-mirror, and then the procedure would be to sum all families, thus all possible rays. This approach would be successful if the sums required to sum all rays within a family were not conditionally convergent. Approximating conditionally convergent sums by truncating them is a strategy that is prone to large errors. Thus, to approximate r , with arbitrary precision, in a multilayer where conditionally convergent sums appear, rays must be added to the sum with gradually increasing length. This method is the hierarchical summation scheme and it is described in detail in Paper I.

2.4 Absorbing films with surface structures in two dimensions

Ray splitting with phase-carrying rays is also a valid approach for calculating the absorption efficiency in infinitely long two-dimensional planar film structures. It is valid with both orthogonal incident light, which is effectively the one-dimensional problem, and oblique incident light assuming the polarization remains perpendicular to the plane of incidence [4]. For non-planar films, a theory with phase-carrying rays has not yet been developed. However, in sufficiently large structures compared to the wavelength of interest, one can opt to use geometric optics which excludes semiclassical phases.

2.4.1 The film+dome model system

To study the effect of chaotic dynamics of rays and waves on the absorption efficiency, a suitable model system is needed that exhibits a transition from regular to chaotic dynamics as a function of some system parameter. The Bunimovich stadium is one of the most well studied chaotic billiards in the literature. It is constructed by placing semicircles with radius r at both short sides of a $2r \times l$ rectangle, see Fig. 2.6a. This basic idea of this shape is, with a few modifications, used to construct a surface structured solar cell model. The Bunimovich stadium is cut across its straight middle section and the dome mirror is removed and a new mirror is placed along the cut. Hence, this system consists of a smaller rectangle attached to a dome. This system is called *film+dome*, and is shown in Fig. 2.6b. The side mirrors confine the system to a single unit cell. Because of the presence of the side mirrors, the system has a mirror symmetry along the middle of the “bucket shaped” mirror configuration. The “bucket” unit cell can be repeated periodically to result in a laterally extended solar cell. In an experimental realization of this system, the structure could be a periodic structure with thin reflecting walls defining the unit “bucket” cell, and periodically repeating domes on top of a conventional solar cell without surface structure. Since realization of the side mirrors in the extended system is experimentally difficult to do, and perhaps even unnecessary, one might instead simulate a system where the side mirrors are eliminated in favor of periodic boundary conditions. This, perhaps more realistic system, has not been investigated within the framework of this thesis and is subject to further investigation. However, it is expected that the bucket model with side mirrors and a model with periodic boundary conditions will yield qualitatively similar results.

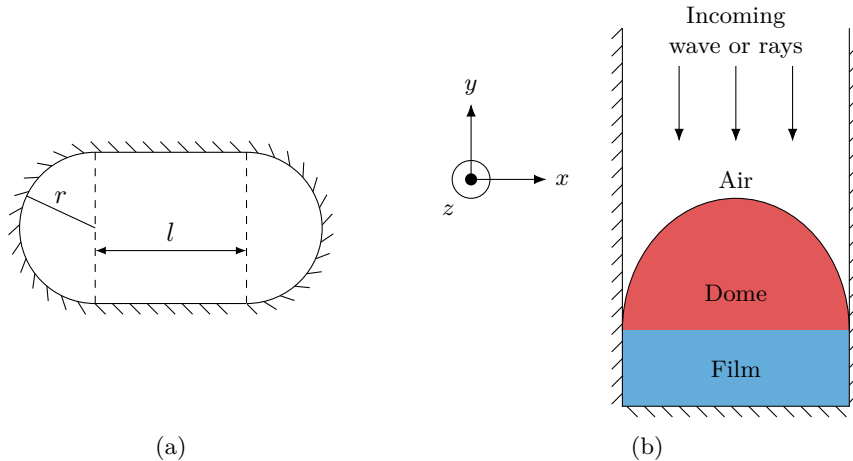


Figure 2.6: a) The closed Bunimovich billiard system. b) The open film+dome system.

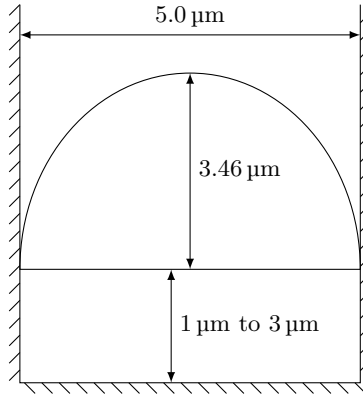


Figure 2.7: The measurements of the film+dome system. Several film thicknesses from $1\ \mu\text{m}$ to $3\ \mu\text{m}$ were used.

The exact shape of the dome in the film+dome system differs from the semicircular domes in the Bunimovich stadium. Instead an ellipse was tuned to find the maximum absorption efficiency given a film thickness of $2\ \mu\text{m}$. The exact measurements of the film+dome systems that have been investigated are given in Fig. 2.7.

2.5 Classical ray dynamics in two dimensions

The dynamics of classical rays are governed by the laws of geometrical optics, namely the laws of refraction and reflection. The reflection law is simple - the angle of the reflected ray is equal to the angle of the incident ray with respect to the normal of the reflecting surface. This law is applied to all mirror surfaces in the film+dome system, i.e. specular reflection is assumed at the mirrors. The refraction law describes the refraction of light across the interface of two isotropic media described by their index of refraction n_1 and n_2 . The angle of incidence, θ_1 , is related to the angle of refraction, θ_2 , with Snell's simple expression

$$n_1 \sin(\theta_1) = n_2 \sin(\theta_2). \quad (2.11)$$

The interface between media with different index of refraction is a ray splitting surface. Most of the time, light is not fully refracted into the adjacent medium, but splits into a refracted ray, often called transmitted as it represents the ray that transmits from one medium to another, and a ray specularly reflected off the interface between the two media. Fig. 2.8a illustrates this phenomenon. This type of ray splitting is in principle the same as the ray splitting presented for the one-dimensional films in Sec. 2.3. Fig. 2.9 shows an example of how a single incoming ray splits into several ray branches.

The fraction of energy carried by the transmitted and the reflected ray is described by the Fresnel equations [112]. This is different from the one-dimensional films where the transmission and reflection amplitudes were derived from the continuity properties of the quantum mechanical wave function. The Fresnel equations depend on the direction of the polarization with respect to the plane of incidence. For *s*-polarized light, i.e. polarization perpendicular to the plane of incidence, the Fresnel equations are

$$r_s = \frac{\cos \theta_1 - \sqrt{n'^2 - \sin^2 \theta_1}}{\cos \theta_1 + \sqrt{n'^2 - \sin^2 \theta_1}}, \quad (2.12)$$

$$t_s = \frac{2 \cos \theta_1}{\cos \theta_1 + \sqrt{n'^2 - \sin^2 \theta_1}}, \quad (2.13)$$

For *p*-polarized light, when the polarization is parallel to the plane of incidence, the Fresnel equations are

$$r_p = \frac{-n'^2 \cos \theta + \sqrt{n'^2 - \sin^2 \theta}}{n'^2 \cos \theta + \sqrt{n'^2 - \sin^2 \theta}} \quad (2.14)$$

$$t_p = \frac{2n' \cos \theta}{n'^2 \cos \theta + \sqrt{n'^2 - \sin^2 \theta}}. \quad (2.15)$$

For both sets of equations $n' = n_2/n_1$ is introduced. If the film+dome system is imagined to be a two-dimensional structure with a third cylinder symmetric dimension sticking out of the paper plane (Fig. 2.6b), it is then necessary to assume *s*-polarized Fresnel equations, i.e. polarization along the cylindric dimension, to obtain the same result in each “slice” of the cylinder. The exception to partial transmission and reflection is if the incident ray is coming towards an interface from an optically denser material with θ greater than some critical angle

$$\theta_c = \sin^{-1} \left(\frac{n_1}{n_2} \right). \quad (2.16)$$

This phenomenon is called total internal reflection, see Fig. 2.8b. The ray is not split into a transmitted and reflected ray, only a specular reflected ray, hence the name.

2.5.1 Absorption efficiency

The absorption efficiency is defined the same way as for the one-dimensional films, $1 - R$, and given the symbol σ . The hierarchical summations scheme introduced in Sec. 2.3 gives the correct summation order of rays for a finite set of rays to yield an approximation of the exact reflectance R . Since there is no hierarchical

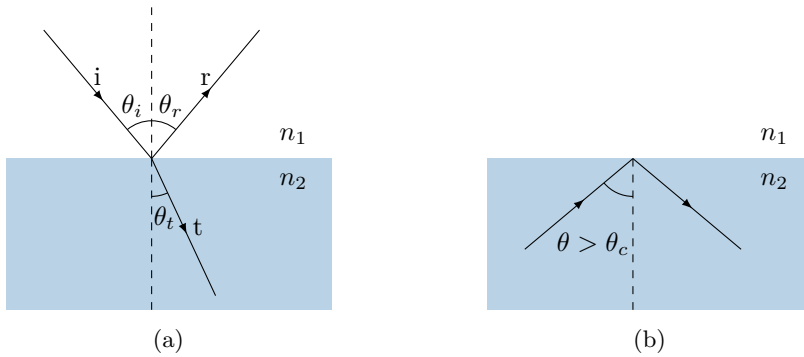


Figure 2.8: a) Schematic showing the refraction and reflection of an incoming ray. b) Total internal reflection when the incoming angle θ is larger than θ_c . $n_2 > n_1$ in both a) and b).

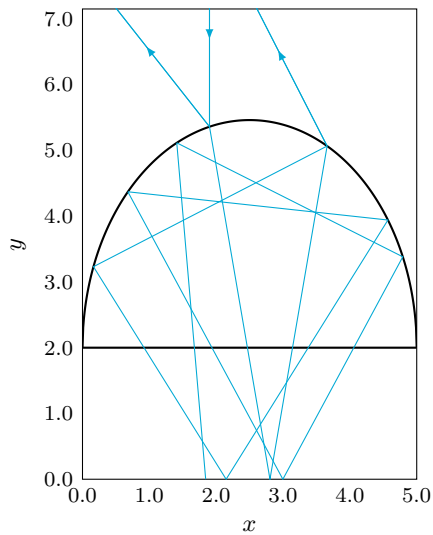


Figure 2.9: A simulation of an incoming ray which splits, reflects and transmits as it moves inside the film+dome with $n_{\text{dome}} = n_{\text{film}} = 2$. Each branch is artificially terminated prematurely to make it easier to see the ray splitting into reflected and transmitted branches. The direction of the incoming and outgoing rays are indicated with arrows.

summation scheme for counting rays known for two-dimensional film structures with non-flat surfaces, the reflectance R is instead calculated using Beer-Lambert's law of absorption [112]. It can be used to calculate the average absorption of an ensemble of rays sent toward the film+dome system. The number of rays in the ensemble must be large enough to give a good approximation for the absorption efficiency. In Fig. 2.10a the absorption efficiency is plotted against the number of rays incident on a film+dome system with $n_{\text{dome}} = n_{\text{film}} = 2$. The intensity of a ray is attenuated exponentially as it travels through an absorbing medium by an attenuation factor

$$e^{-4\pi n_i x / \lambda}, \quad (2.17)$$

where n_i is the imaginary part of the index of refraction which provides absorption to the medium and the distance x is the length of the ray through the absorbing medium. Each incident ray is given an initial intensity of 1 which decays proportionally to x . Classical rays do not have a wavelength, but the wavelength, denoted by λ , appears through Beer-Lambert's law.

Truncating the lifetime of rays

Non-Newtonian ray simulations could in theory last forever. There is always a part of any incident ray which will never return from the scattering system. Note that in the event of ray splitting, the incident "mother" ray carries intensity $a \leq 1$. The intensities of the reflected and transmitted ray "branches" b and c , respectively, add to the intensity of their mother ray, $a = b + c$. Ray splitting generates an increasing number of non-escaping rays as the simulation goes on. The simulation time of a given ray must therefore be truncated.

An incident ray starts with intensity 1 which dissipates through Beer-Lambert's law and splits into branches through the Fresnel equations at ray splitting surfaces. The simulation of that particular incoming ray is terminated when the intensity of each branch drops below a threshold value, or the ray escapes. Such a truncation introduces an intensity loss called the *truncation loss*. If this threshold is set too high, a lot of intensity is lost due to short simulation time. On the other hand, if it is set too low, the simulation would continue for a long time. The truncation loss is plotted versus the threshold in Fig. 2.10b for a film+dome system with $n_{\text{dome}} = n_{\text{film}} = 2$ and 10000 incoming rays.

2.5.2 Fractal dimension of scattering fractals

The existence of a chaotic repeller is a signature of classical chaotic scattering [113]. A chaotic repeller has a non-integer fractal dimension d [93–95]. The concept of fractal dimensions was introduced by Benoît Mandelbrot [114] and can be defined

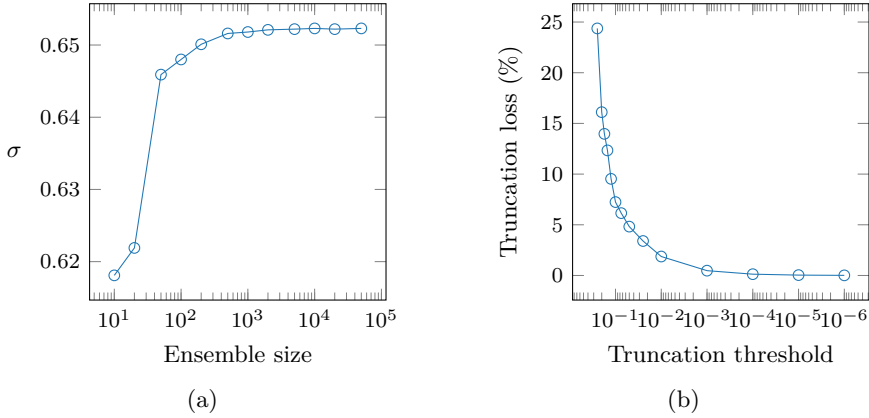


Figure 2.10: a) The absorption efficiency σ as a function of the ensemble size of incident rays. b) The truncation loss is the loss of intensity due to truncation of the simulation time, here shown as a function of the truncation threshold. Both a) and b) for a film+dome system with $n_{\text{dome}} = n_{\text{film}} = 2$.

in simple terms with a method known as the box counting method, explained below. The repeller consists of Newtonian rays which neither enter nor leave the film+dome system, thus having infinitely long lifetime. This set of rays can be found by tracing rays starting from inside the film+dome system. The lifetime of a given ray is measured by recording how many times it collides with a select section of the total phase space, called the Poincaré surface of section (PSOS). For solar cell applications it is important that the rays spend most of their time in the absorbing film. The PSOS is therefore chosen to be the backside or bottom mirror of the film+dome system. However, the absorption mechanisms are disabled in these simulations to prevent rays from being terminated prematurely. The only termination condition is escape from the system or exceeding a set limit of collisions with the PSOS. The collision limit is put in place to respect that the precision of the ray simulations degrades quickly when chaos is present in the system due to the sensitivity to initial conditions.

A number of rays with initial conditions (x_i, θ_i) , see Fig. 2.11b are started from the PSOS and their lifetimes are registered. The resulting image is called a scattering fractal. The chaotic repeller is contained in the scattering fractal. An example of a scattering fractal with a chaotic repeller is shown in Fig. 2.11a for a film+dome system with $n_{\text{dome}} = n_{\text{film}} = 2$ where the lifetime of each initial point is color-coded.

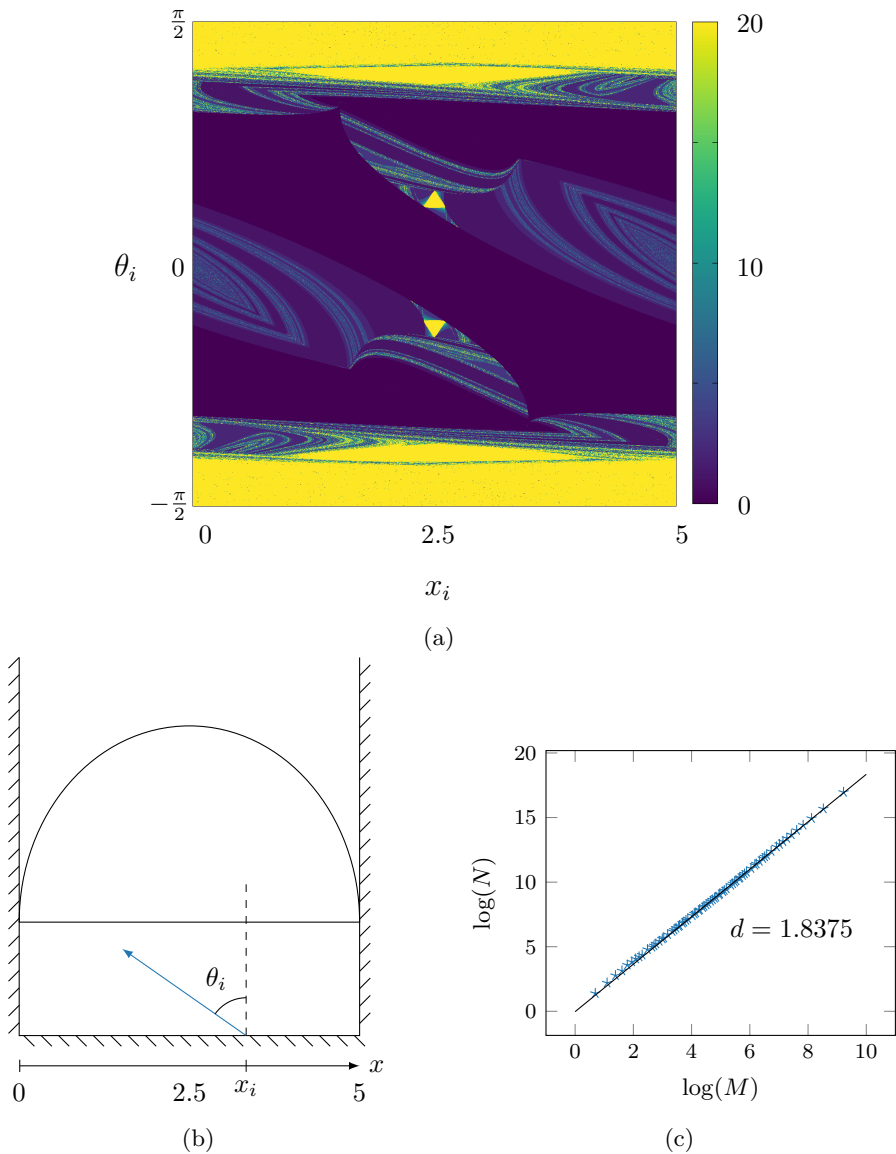


Figure 2.11: a) A scattering fractal with non-integer geometry. b) Schematic showing a ray with initial conditions (x_i, θ_i) . c) A log-log plot of the number of boxes N as a function of the box scale M . The slope of the linear fit gives the fractal dimension d .

Box counting method

The box counting method [115–118] is a procedure of calculating the fractal dimension of an object, for instance a scattering fractal, by covering it with gradually smaller boxes while counting how many boxes are needed to cover the entire object. The fractal dimension d of a scattering fractal is thus defined

$$d = \lim_{M \rightarrow \infty} \frac{\log N}{\log M}, \quad (2.18)$$

where N is the number of boxes needed to cover the scattering fractal, and M is the scale of the boxes. Since M can not be taken to ∞ in practice, it is therefore common practice to perform linear regression on $\log(N)$ versus $\log(M)$. The slope of the linear fit is the fractal dimension d , shown in Fig. 2.11c for a film+dome system with $n_{\text{dome}} = n_{\text{film}} = 2$.

There are many ways to implement the box counting method. In the case of scattering fractals, they are stored as images with $P \times P$ pixels where each pixel corresponds to a ray with initial conditions (x_i, θ_i) . Because of this choice, the number of integers P is divisible by determines the number of differently sized boxes the scattering fractal is covered by. If the boxes are made smaller than the pixels, the relationship between $\log(N)$ and $\log(M)$ behaves like a regular two-dimension figure without fractal properties.

2.6 Wave dynamics in the film+dome system

Classical chaos has powerful tools of characterizing dynamics in scattering systems which are intuitive and computationally cheap to perform. Since a solar cell is inherently a wave system, it is therefore necessary to investigate the dynamics of the wave-analog film+dome system. Assume a three-dimensional film+dome system with cylindric symmetry along the z -axis sticking out of the paper plane, as in Fig. 2.6b. Under the assumption that the polarization is perpendicular to the plane of incidence, which lies in the xy plane, the wave problem is essentially two-dimensional. The steady state electromagnetic (E&M) wave equation is then equivalent to the 2D Helmholtz equation

$$[\nabla^2 + n(x, y)^2 K^2] \psi(x, y) = 0, \quad (2.19)$$

where $n(x, y)$ is the index of refraction

$$n(x, y) = \begin{cases} n_{\text{film}} & (x, y) \text{ in film,} \\ n_{\text{dome}} & (x, y) \text{ in dome,} \end{cases} \quad (2.20)$$

and ψ is the wave function, equivalent to the electric field. Equation (2.19) can be solved with the Green's function method (GFM) using the Lippman-Schwinger

formula

$$\psi_p(x, y) = \phi_p(x, y) - \int G(K, x, x', y, y') K^2 [1 - n(x', y')^2] \psi_p(x', y') dx' dy', \quad (2.21)$$

where $G(K, x, x', y, y')$ is the Green's function and $\phi_p(x, y)$ is a free solution with $n(x, y) = 1$, also called a channel wave function. The full derivation of the Green's function is described in detail in the appendix of Paper III. Equation (2.21) is discretized on a lattice shown in Fig. 2.12. The absorption cross section, equivalent to the absorption efficiency $1 - R$, is calculated directly from the scattered wave function ψ .

$$\sigma = \frac{4\pi}{\lambda w} \int n_r(x, y) n_i(x, y) \psi(x, y) dx dy, \quad (2.22)$$

where λ is the wavelength of the incident light, and n_r and n_i are the real and imaginary parts of the index of refraction, respectively.

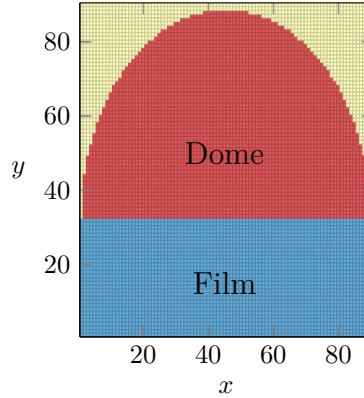


Figure 2.12: The discretized film+dome system.

2.6.1 Exact wave solution for a planar film

An analytic expression for the wave function inside a film placed in a “mirror bucket”, i.e. a film+dome system minus the dome (see Fig. 2.13), can be found by the same procedure as the one used for the one-dimensional film in Sec. 2.2. The film system is shown in Fig. 2.14. The wave function on the outside of the film is the sum of the incoming and outgoing wave

$$\psi_1 = (e^{-ik_{y,1}y} - r e^{ik_{y,1}y}) \sin\left(\frac{p\pi x}{w}\right), \quad (2.23)$$

where r is the reflection amplitude. On the inside of the film the wave function takes the form

$$\psi_2 = A \sin(k_{y,2}y) \sin\left(\frac{p\pi x}{w}\right). \quad (2.24)$$

The wave functions ψ_1 and ψ_2 are weighted by a sine function along the x -direction, which is a consequence of the side mirrors. p determines the shape of the incoming wave.

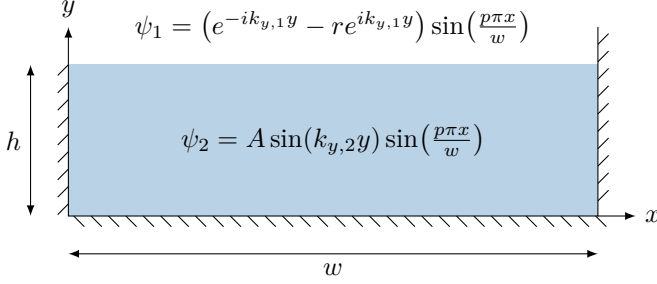


Figure 2.13: The single film system in a bucket shaped mirror configuration.

The total wavenumber in region i , K_i , changes because of the discontinuity of the refractive index $n(x, y)$. The parallel wavenumbers are unchanged across the interface,

$$k_{x,1} = k_{x,2} = k_x = p\pi/w, \quad (2.25)$$

and the perpendicular wavenumbers $k_{y,i}$ are discontinuous, thus the total wavenumber, $K_i^2 = k_{y,i}^2 + k_{x,i}^2$, is also discontinuous

$$K_2 = nK_1. \quad (2.26)$$

Using this, the coefficients r and A are found by applying the continuity properties of the wave function across the air-film interface. The absolute square of the wave function inside the film is

$$|\psi_2|^2 = \frac{4 \sin(k_{y,2}y)^2 \sin(k_x x)}{\sin(k_{y,2}h)^2 + \left(\frac{k_{y,2}}{k_{y,1}}\right)^2 \cos(k_{y,2}h)^2}. \quad (2.27)$$

The precision of the GFM can be assessed by comparing $|\psi_{\text{GFM}}|^2$ with (2.27). The integral of $|\psi_2|^2$ inside a $w \times h$ film is

$$\begin{aligned} I(k_{y,1}, k_{y,2}, k_x) &= \int_0^h \int_0^w |\psi_2|^2 dx dy \\ &= \frac{\left(\frac{h}{2} - \frac{\sin(2k_{y,2}h)}{4k_{y,2}}\right) \left(\frac{w}{2} - \frac{\sin(2k_x w)}{4k_x}\right)}{\sin(k_{y,2}h)^2 + \left(\frac{k_{y,2}}{k_{y,1}}\right)^2 \cos(k_{y,2}h)^2}. \end{aligned} \quad (2.28)$$

Fig. 2.14 shows rolling resonances that are expected from a planar film from both GFM and the exact expression. The GFM curve is shifted a few nanometers to

the right of the exact curve. This shift reduces as the resolution of the GFM mesh is increased.

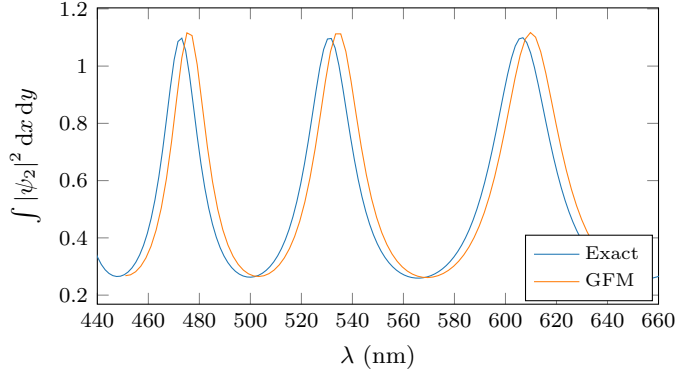


Figure 2.14: Comparison of $\int |\psi_2|^2 dx dy$ as a function of the wavelength λ calculated from the exact expression and numerically from the GFM.

2.6.2 Nearest neighbor eigenangle statistics

Bohigas, Giannoni, and Schmit conjectured that generic time-reversal invariant chaotic wave systems have level distributions fitting the Wigner surmise

$$P(s) = \frac{\pi s}{2} e^{-\pi s^2/4}. \quad (2.29)$$

In the context of quantum chaotic scattering, $P(s)$ is the probability density function of a sequence of nearest neighbor spacings between the eigenangles of the scattering matrix S . The S matrix gives the probability amplitude of scattering from an incoming channel wave function in channel p

$$\psi_p = e^{-ik_y y} \sin\left(\frac{p\pi x}{w}\right), \quad (2.30)$$

to an outgoing wave channel m . The total scattered wave from the incoming wave in channel p is a mix of outgoing waves

$$\psi_p = \sum_{m=1}^M S_{p \rightarrow m} e^{iB_m y} \sin\left(\frac{p\pi x}{w}\right), \quad (2.31)$$

where M is the number of available channel wave functions and B_m is the wave number along the y -direction. M is determined by the energy of the incoming wave and the width of the film+dome system. $S_{p \rightarrow m}$ is the scattering amplitude

from channel p to m ,

$$S_{p \rightarrow m} = -\delta_{pm} - \frac{2K^2}{wB_m} \int \sin\left(\frac{m\pi x'}{w}\right) \sin(B_m y') \times [1 - n(x', y')^2] \psi_p(x', y') dx' dy'. \quad (2.32)$$

A more detailed derivation of (2.32) can be found in Paper III. The S matrix is unitary for Hamiltonian systems with eigenvalues on the unit circle, $e^{i\xi}$. The distribution of spacings between the nearest neighbors of the scaled eigenangles, $\xi_s = \xi M/2\pi$, follow the Wigner surmise if the system is chaotic. The nearest neighbor eigenangle distribution of a film+dome system is tested by taking a collection of nearest neighbor spacings from a number of S matrices, sampled by varying the energy of the incoming wave, and comparing it to the Wigner surmise.

Chapter 3

Results and discussions

3.1 Paper I

Exact ray theory for the calculation of the optical generation rate in optically thin solar cells

In Paper I, an exact ray theory was developed for solar cell models consisting of thin layers. We looked at structures below the geometrical optics limit, i.e. beyond the validity of geometrical ray optics. Summing rays with phases attached to them perfectly reproduces the predictions of the quantum mechanical wave equation. The paper presents a new ray formalism with ray splitting and phases to calculate the absorption cross section (σ) of absorbing planar film stacks, showing the duality between rays and waves. We found that all rays can be summed analytically for a system consisting of a single film with or without a backside mirror. Figure 3.1a shows that only a small number of rays are needed to obtain results in agreement with those obtained from a full wave theory of such systems. The importance of phases is seen clearly from Fig. 3.1b. The resonance structure in σ is only present when phases are included. Summing all rays and leaving out the phases, yields only an approximation of the lower modulation of σ .

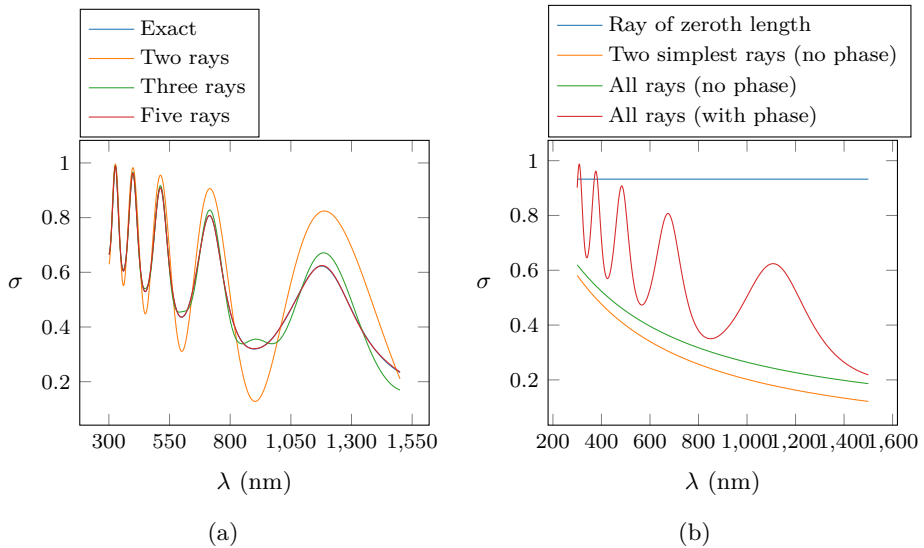


Figure 3.1: a) The absorption cross section σ as a function of the wavelength λ for an absorbing film with a backside mirror. The refractive index of the 500 nm thick film is $1.8+0.05i$. b) Comparison showing the importance of including phases. Both figures are adapted from Paper I.

For film stacks with more than one layer, it was found that an analytic summation of all rays is not possible. A hierarchical summation scheme (HSS) was developed

to approximate σ . The HSS truncates the infinite sums by terminating the rays after a predefined number of ray splitting events which determines the quality of the approximation. The consequence is that only rays up to a certain length are included in the approximation of σ . The lengths of the longest rays are always comparable, and the approximation is more accurate when a large number of splitting events is allowed.

A Fourier transform of the reflection amplitude $(1 - \sigma)$ revealed the path lengths of the most important rays in a film stack with three layers, shown in Fig. 3.2. The path of the most important rays is information that gives new insight about the scattering dynamics in multilayered structures. It is possible to design systems to force the most important rays to spend most of their time in the absorbing layer for maximizing the absorption cross section. Systems can be tuned by changing the number of layers, index of refraction and layer thicknesses. This could prove to be an efficient tool for engineers to understand the ray dynamics in multilayer structures for enhancing the absorption cross section.

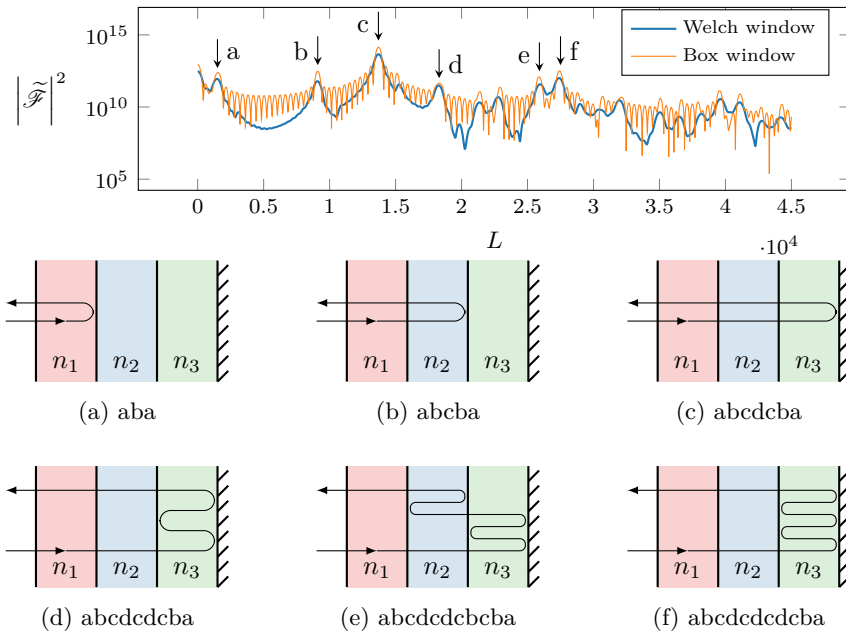


Figure 3.2: Top frame: Finite-range Fourier transform (approximate length spectrum) $\tilde{\mathcal{F}}(L)$ of the exact $r(k)$ of a three-layer film system with a backside mirror. $\tilde{\mathcal{F}}(L)$ shows distinct peaks, labeled (a)–(f). The rays corresponding to these peaks, including their symbolic-dynamics labels, are illustrated in the six frames (a)–(f), below the top frame, respectively. These six rays make the most important contributions in the ray-representation of $r(k)$ of this system. The figure is adapted from Paper I.

3.2 Paper II

Chaos: A new mechanism for enhancing the optical generation rate in optically thin solar cells

In Paper II, a correlation between the onset of chaotic dynamics and enhancement of absorption efficiency was demonstrated in a classical ray system. It was shown that the absorption efficiency is greater if chaotic ray dynamics is present, compared to a similar system with regular ray dynamics. The film+dome model system used in the study consists of an absorbing film with a non-absorbing elliptical dome on top. The film+dome system has the ability to change from regular to chaotic dynamics as a function of the index of refraction in the dome, n_{dome} . The classical ray dynamics were investigated with a ray tracing code, written specifically for this system, using ray splitting and absorption modeling with Beer-Lambert's law. The accuracy of the Beer-Lambert absorption efficiency using classical ray tracing proved to be comparable to the average absorption cross section calculated with a commercial full E&M FDTD solver, see Fig. 3.3a.

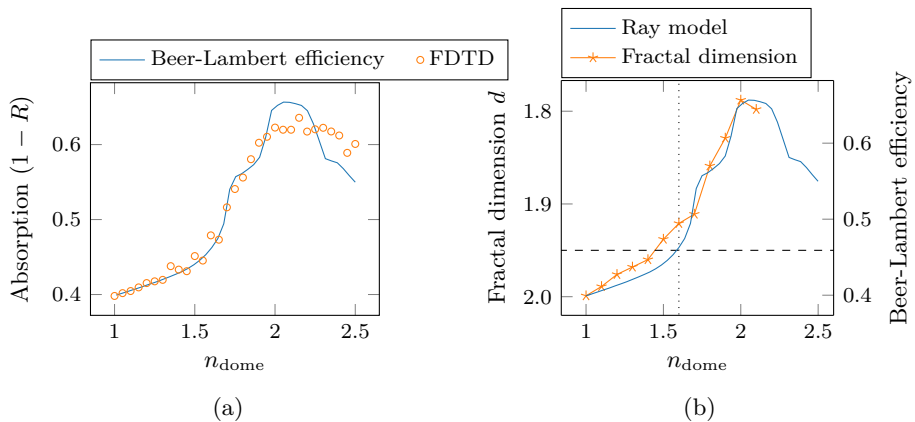


Figure 3.3: (a) Absorption efficiency calculated with a commercial FDTD solver compared to the Beer-Lambert absorption efficiency calculated by rays. b) Visualization of the fractal dimension (orange) and the Beer-Lambert efficiency (blue). The onset of chaos is determined by the first data point below a fractal dimension of 1.95, indicated by a horizontal dashed line. The rapid increase of the Beer-Lambert efficiency is indicated by a vertical dotted line. Both figures are adapted from Paper II.

Chaotic dynamics is associated with a non-integer fractal dimension of the invariant set which is visualized as a scattering fractal. The onset of chaos was therefore determined by measuring the fractal dimension of scattering fractal with a box counting method, which was integrated into the ray tracing code. The fractal dimension was calculated for film+dome systems with n_{dome} from 1.0 to 2.5. A

systematic correlation between the rapid increase in Beer-Lambert efficiency and fractal dimension below a threshold value was observed. An example of this is seen in Fig. 3.3b for a film+dome system with $2.0\ \mu\text{m}$ film thickness.

The results were found to be structurally stable with respect to the film thickness, i.e. the chaos \leftrightarrow efficiency correlation holds even if the film thickness is changed. This was done by studying critical behavior in the fractal dimension, Beer-Lambert efficiency, and incoming Newtonian rays (see Fig. 3.4), while varying the film thickness from $0.5\ \mu\text{m}$ to $4.0\ \mu\text{m}$. The critical value, n_{critical} , was found in each of the three cases. These critical values show the same trend as a function of film thickness, and are visualized in Fig. 3.5. Because it is hard to recreate microstructures down to the smallest details, structural stability is important for experimentalists to perform studies on film+dome systems.

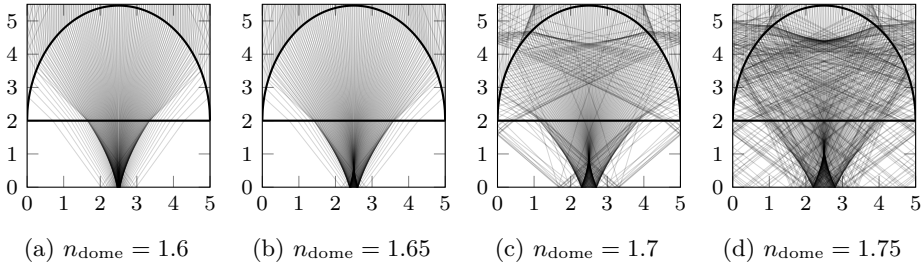


Figure 3.4: Newtonian rays sent from the outside for different values of n_{dome} . At the critical value $n_{\text{dome}} = 1.7$ the rays become sensitive to their initial condition.

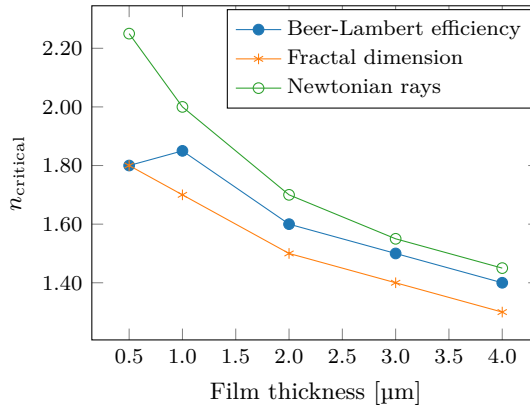


Figure 3.5: The n_{critical} is the value for when the Beer-Lambert efficiency (blue) starts to increase more rapidly, the fractal dimension (orange) is below 1.95, and the Newtonian rays sent from the outside directly downwards (green) visually start to behave sensitively on the initial conditions. The figure is adapted from Paper II.

3.3 Paper III

Wave chaos enhanced light trapping in optically thin solar cells

In Paper III, the wave-analog to the classical film+dome system studied in Paper II was investigated with techniques from quantum chaos. As in Paper II, the same correlation was found between the rapid enhancement of absorption cross section and the onset of chaotic dynamics. The onset of chaos was also linked to enhanced light trapping. An increase in the average dwell time of rays in the system was observed, making it a three-way correlation between dwell time, enhancement of absorption and chaotic wave dynamics.

The Helmholtz equation was solved numerically in a discretized film+dome system using the Green's function method to carry out wave calculations. Figure 3.6 shows typical behavior of the wave function with scarlets appearing as n_{dome} is increased and the system becomes chaotic. Some wave functions were also scarred by the unstable periodic orbits present in the system.

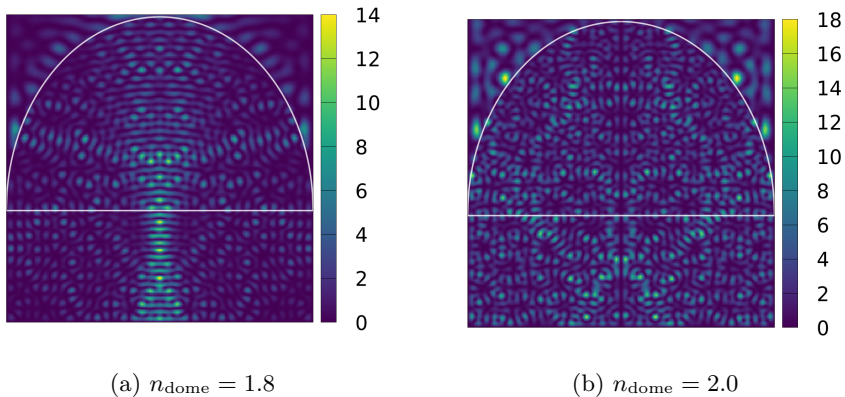


Figure 3.6: Irregularities in the scattered wave function become more and more prevalent with increasing n_{dome} . This is a signature of chaos. The figures are adapted from Paper III.

To quantify the onset of chaos, the S matrix was derived. The eigenangle statistics of nearest-neighbor spacings were numerically calculated for film+dome systems with n_{dome} ranging from 1.0 to 2.0. These statistics were compared with interpolating distributions between regular (Poisson distribution) and chaotic (Wigner distribution) scattering dynamics. The Berry-Robnik and Brody distributions were fitted to histograms of the statistics (see Fig. 3.7) using a χ^2 test. Histograms belonging to chaotic film+dome systems with n_{dome} above a certain value were found to pass the χ^2 test. For film+dome systems with 1 μm , 2 μm and 3 μm thick

films, the tests were passed at n_{dome} equal to 1.9, 1.6 and 1.5, respectively. These values are comparable with the n_{critical} values found in Paper II for the classical film+dome systems.

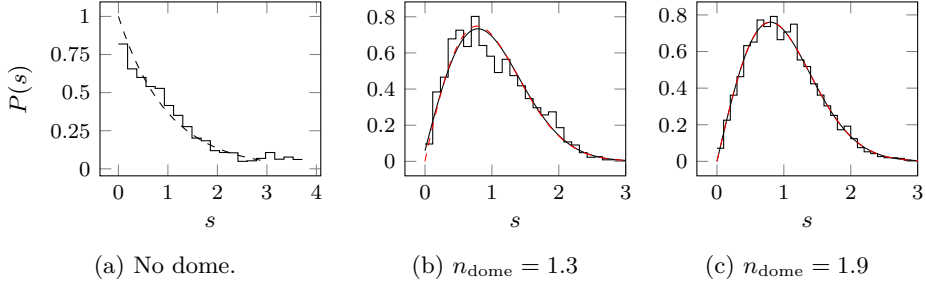


Figure 3.7: The histograms shows the level statistics of the different film+dome systems. The dashed line is the Poisson distribution, $P(s) = e^{-s}$ and the solid line is the Wigner surmise. For low values of n_{dome} the film+dome system is pseudo-integrable. At n_{dome} equal to 1.1 and 1.2 the distributions are between the pseudo-integrable and Wigner case. The smooth black line is the best-fitting Berry-Robnik distribution and the red, dashed line is the best-fitting Brody distribution.

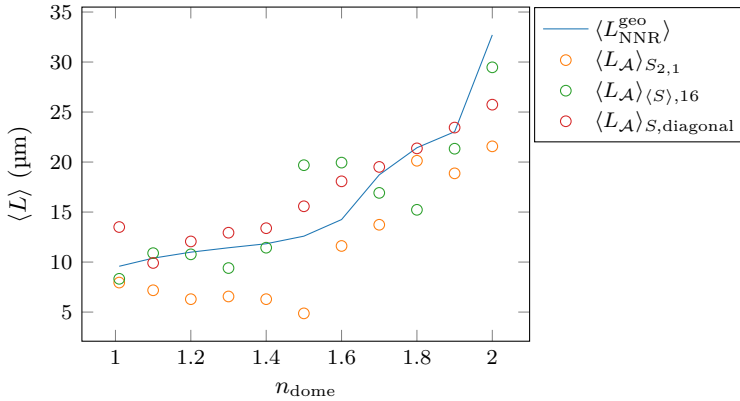


Figure 3.8: Average geometric path length calculated by ray-tracing 10000 non-Newtonian rays (blue full line), derived from the width of the autocorrelation function, using $S_{2,1}$ (orange open circles), using an average over 16 off-diagonal S-matrix elements (green open circles), and averaging over all diagonal S-matrix elements (red open circles). The figure is adapted from Paper III.

An approximation of the average dwell time of rays, $\langle L_{\mathcal{A}} \rangle$, were extracted from the autocorrelation function of the S matrix. It was revealed that the average dwell time of rays increased for higher values of n_{dome} and coincided with the onset of chaos, meaning that chaos is a mechanism that improves light trapping. Moreover, $\langle L_{\mathcal{A}} \rangle$ showed remarkably good agreement with the geometric lengths of classical

non-Newtonian rays, see Fig. 3.8. We highlighted that our results can be verified experimentally by measuring the autocorrelation function. Hence, the three-way correlation between chaos, absorption efficiency and light trapping can be shown experimentally for a realization the film+dome system.

Chapter 4

Conclusion

The overarching goal of this thesis is to test the chaos hypothesis, i.e., the statement “chaotic scattering enhances the light trapping properties in optically thin solar cells”. To this end, the effects of chaotic scattering dynamics were studied with rays in the classical regime, and with scalar waves in the wave regime.

A new ray model for calculating the exact absorption cross section was developed for one-dimensional stacks of absorbing planar films in Paper I. The ray formalism presented yields the same results for reflection, transmission and absorption as the solutions of Maxwell’s equations in one dimension. It was demonstrated how the dynamics of rays can be used to evaluate the exact reflectance and absorption properties of a given system when the correct phase, transmission and reflection amplitudes are included for rays splitting at material interfaces. With this ray model it is possible to identify the trajectories of the rays that affect the reflectance the most, and to account for film interference effects neglected by simpler ray models.

The ray model was the foundation of a more general ray model in two dimensions using conventional ray optics in addition to ray splitting. This ray tracer was presented in Paper II, and was used to study the ray dynamics of surface structured solar cell models where the scattering dynamics was changed from regular to chaotic by tuning the refractive index of the dome in the film+dome system. Chaotic dynamics were identified above a certain value of the index of refraction by calculating the fractal dimension of scattering fractals. The behavior of incoming Newtonian rays at this critical value supported the findings. In addition, it was found that the Beer-Lambert efficiency rapidly improved at the critical value. A systematic correlation between absorption efficiency and onset of chaos was demonstrated over a range of different film+dome systems with varying film thicknesses, proving that the correlation is structurally stable.

In Paper III, a scalar wave solver for the Helmholtz equation based on the Green’s function method was developed to analyze the wave functions and scattering matrices of the film+dome system. The presence of classical chaos presented in Paper II was verified on the wave level. The average dwell time of rays was extracted from the scattering matrix and compared to the geometric length of non-Newtonian rays. It was found that the chaos \leftrightarrow efficiency correlation is a three-way chaos \leftrightarrow efficiency \leftrightarrow dwell time correlation. The central topics in this thesis, i.e., chaotic dynamics, improved absorption efficiency and light trapping, are linked together by this result.

Chapter 5

Further Research

With the framework for studying the dynamics of rays and waves in place, it is of great interest to pursue the connection between chaos and light trapping further. There are numerous papers available showing that surface structuring dramatically enhances the efficiency of a solar cell. The parameter space is enormous and impossible to explore experimentally. In addition, not all structures are feasible to fabricate even on the lab scale. Therefore, numerical experiments are frequently used as guides to find relevant systems to characterize experimentally. This job is easier if one can make a good initial guess or look for something specific. As this thesis and associated papers document, chaos can be the thing to be on the look-out for, and ray tracing is one of the tools which fits the job.

If I were to make specific suggestions for topics for further research, I would propose to characterize the film+dome system experimentally to verify the results. One of the challenges would be to recreate the microscale morphology with materials covering the range of refractive indices. On the simulation side, it would be very interesting to investigate how the dynamics of existing high-performance light trapping schemes compare to each other. Are such systems chaotic or regular?

In the course of my graduate studies some time was spent on investigating random surface structures. Due to time constraints, this topic was not explored enough to result in a publication. The scattering dynamics of ensembles of realizations of random surface structures is therefore proposed as a topic for further research. The general idea which was pursued by our group was the study and comparison of random surface structures and the film+dome system. It is well known that random surface structures can facilitate efficient light trapping. Chances are that chaos plays a role in the dynamics of systems with random surface structures. How do ordered structures compare with chaotic dynamics? A study of ordered and disordered structures with and without chaotic dynamics would be an interesting topic to pursue.

References

- [1] M.A. Brandsrud, E. Seim, R. Lukacs, A. Kohler, E.S. Marstein, E. Olsen, and R. Blümel. Exact ray theory for the calculation of the optical generation rate in optically thin solar cells. *Physica E: Low-dimensional Systems and Nanostructures*, 105:125 – 138, 2019.
- [2] E. Seim, A. Kohler, R. Lukacs, M. A. Brandsrud, E. S. Marstein, E. Olsen, and R. Blümel. Chaos: A new mechanism for enhancing the optical generation rate in optically thin solar cells. *Chaos: An Interdisciplinary Journal of Nonlinear Science*, 29(9):093132, 2019.
- [3] E. Seim, A. Kohler, R. Lukacs, M.A. Brandsrud, E.S. Marstein, E. Olsen, and R. Blümel. Wave chaos enhanced light-trapping in optically thin solar cells. *Chaos: An Interdisciplinary Journal of Nonlinear Science*, submitted Oct 2019.
- [4] M.A. Brandsrud, R. Lukacs, R. Blümel, E. Seim, E.S. Marstein, E. Olsen, and A. Kohler. An exact ray model for oblique incident light on planar films. work in progress.
- [5] M.A Brandsrud, R. Lukacs, R. Blümel, E. Seim, E.S. Marstein, E. Olsen, and A. Kohler. Resonance structures in layers of planar films. work in progress.
- [6] E. Seim, A. Kohler, R. Lukacs, M.A. Brandsrud, E.S. Marstein, E. Olsen, and R. Blümel. Chaos: a new mechanism for enhancing the optical generation rate in optically thin solar cells. In Alexandre Freundlich, Laurent Lombez, and Masakazu Sugiyama, editors, *Physics, Simulation, and Photonic Engineering of Photovoltaic Devices VIII*, volume 10913, pages 213 – 221. International Society for Optics and Photonics, SPIE, 2019.
- [7] M.A Brandsrud, R. Lukacs, R. Blümel, E. Seim, E.S. Marstein, E. Olsen, and A. Kohler. Optimized solar cells based on changes in resonance structure as a function of the refractive index and the thickness. In Alexandre Freundlich, Laurent Lombez, and Masakazu Sugiyama, editors, *Physics, Simulation, and*

- [8] E. Seim, A. Kohler, R. Lukacs, M.A. Brandsrud, E.S. Marstein, E. Olsen, and R. Blümel. Wave chaos: A new mechanism for enhancing the absorption cross section of optically thin solar cells. Presented at: *Norwegian Solar Cell Conference 2019-05-20–2019-05-21*.
- [9] M.A. Brandsrud, R. Lukacs, R. Blümel, E. Seim, E.S. Marstein, E. Olsen, and A. Kohler. Optimized solar cells based on changes in resonance structure as a function of the refractive index and the thickness. Presented at: *SPIE Photonics West 2019-02-01–2019-02-06*.
- [10] M.A. Brandsrud, E. Seim, J.H. Solheim, R. Blümel, and A. Kohler. Does chaotic scattering affect the extinction efficiency in quasi-spherical scatterers? Presented at: *BioSpecMLC 2019-04-18–2019-08-21*.
- [11] M.A. Brandsrud, R. Lukacs, R. Blümel, E. Seim, E.S. Marstein, E. Olsen, and A. Kohler. Two-dimensional ray theory for optically thin solar cells. Presented at: *Norwegian Solar Cell Conference 2019-05-20–2019-05-21*.
- [12] E. Seim, A. Kohler, R. Lukacs, M.A. Brandsrud, E.S. Marstein, E. Olsen, and R. Blümel. Chaos: A new mechanism for enhancing the optical generation rate in thin-film solar cells. Presented at: *SPIE Photonics West 2019-02-01–2019-02-06*.
- [13] E. Seim, A. Kohler, R. Blümel, M.A. Brandsrud, and R. Lukacs. Light trapping by structured surfaces in the regular and chaotic scattering regime. Presented at: *Norwegian Solar Cell Conference 2017-05-09–2017-05-10*.
- [14] M.A. Brandsrud, A. Kohler, R. Blümel, E. Seim, and R. Lukacs. The importance of coupling between spheres for the efficiency enhancement of periodically structured solar cells. Presented at: *Norwegian Solar Cell Conference 2017-05-09–2017-05-10*.
- [15] European Commission. EU 2030 climate & energy framework. https://ec.europa.eu/clima/policies/strategies/2030_en. Accessed: 2019-08-05.
- [16] International Renewable Energy Agency. Renewable power generation costs in 2018, 2018.
- [17] International Energy Agency. IEA a snapshot of global PV. <http://www.iaea-pvps.org/index.php?id=266>, 2019. Accessed: 2019-08-05.
- [18] Martin A Green. Third generation photovoltaics: solar cells for 2020 and beyond. *Physica E: Low-dimensional Systems and Nanostructures*, 14(1-2):65–70, 2002.

-
- [19] Martin A Green. Thin-film solar cells: review of materials, technologies and commercial status. *Journal of Materials Science: Materials in Electronics*, 18(1):15–19, 2007.
- [20] Frank Dimroth and Sarah Kurtz. High-efficiency multijunction solar cells. *MRS bulletin*, 32(3):230–235, 2007.
- [21] Wolfgang Guter, Jan Schöne, Simon P Philipps, Marc Steiner, Gerald Siefer, Alexander Wekkeli, Elke Welser, Eduard Oliva, Andreas W Bett, and Frank Dimroth. Current-matched triple-junction solar cell reaching 41.1% conversion efficiency under concentrated sunlight. *Applied Physics Letters*, 94(22):223504, 2009.
- [22] RR King, DC Law, KM Edmondson, CM Fetzer, GS Kinsey, H Yoon, RA Sherif, and NH Karam. 40% efficient metamorphic GaInP/ GaInAs/ Ge multijunction solar cells. *Applied physics letters*, 90(18):183516, 2007.
- [23] Masafumi Yamaguchi, Tatsuya Takamoto, and Kenji Araki. Super high-efficiency multi-junction and concentrator solar cells. *Solar energy materials and solar cells*, 90(18-19):3068–3077, 2006.
- [24] Dirk König, K Casalenuovo, Y Takeda, G Conibeer, JF Guillemoles, R Patterson, LM Huang, and MA Green. Hot carrier solar cells: Principles, materials and design. *Physica E: Low-dimensional Systems and Nanostructures*, 42(10):2862–2866, 2010.
- [25] AJ Nozik. Quantum dot solar cells. *Physica E: Low-dimensional Systems and Nanostructures*, 14(1-2):115–120, 2002.
- [26] Antonio Luque, Antonio Martí, and Colin Stanley. Understanding intermediate-band solar cells. *Nature Photonics*, 6(3):146, 2012.
- [27] Guangda Niu, Xudong Guo, and Liduo Wang. Review of recent progress in chemical stability of perovskite solar cells. *Journal of Materials Chemistry A*, 3(17):8970–8980, 2015.
- [28] Martin A. Green, Yoshihiro Hishikawa, Ewan D. Dunlop, Dean H. Levi, Jochen Hohl-Ebinger, and Anita W.Y. Ho-Baillie. Solar cell efficiency tables (version 51). *Progress in Photovoltaics: Research and Applications*, 26(1):3–12, 2018.
- [29] Kunta Yoshikawa, Hayato Kawasaki, Wataru Yoshida, Toru Irie, Katsunori Konishi, Kunihiko Nakano, Toshihiko Uto, Daisuke Adachi, Masanori Kanematsu, Hisashi Uzu, and Kenji Yamamoto. Silicon heterojunction solar cell with interdigitated back contacts for a photoconversion efficiency over 26%. *Nature Energy*, 2:17032 EP –, Mar 2017. Article.
- [30] T. Tiedje, E. Yablonovitch, G. D. Cody, and B. G. Brooks. Limiting efficiency of silicon solar cells. *IEEE Transactions on Electron Devices*, 31(5):711–716, May 1984.
-

-
- [31] Lucio Claudio Andreani, Angelo Bozzola, Piotr Kowalczewski, Marco Liscidini, and Lisa Redorici. Silicon solar cells: toward the efficiency limits. *Advances in Physics: X*, 4(1):1548305, 2019.
- [32] Romain Cariou, Jan Benick, Frank Feldmann, Oliver Höhn, Hubert Hauser, Paul Beutel, Nasser Razek, Markus Wimplinger, Benedikt Bläsi, David Lackner, et al. Iii-v-on-silicon solar cells reaching 33% photoconversion efficiency in two-terminal configuration. *Nature Energy*, 3(4):326, 2018.
- [33] Jérémie Werner, Florent Sahli, Fan Fu, Juan J Diaz Leon, Arnaud Walter, Brett A Kamino, Bjoern Niesen, Sylvain Nicolay, Quentin Jeangros, and Christophe Ballif. Perovskite/perovskite/silicon monolithic triple-junction solar cells with a fully textured design. *ACS Energy Letters*, 3(9):2052–2058, 2018.
- [34] Stephanie Essig, Christophe Allebé, Timothy Remo, John F Geisz, Myles A Steiner, Kelsey Horowitz, Loris Barraud, J Scott Ward, Manuel Schnabel, Antoine Descoedres, et al. Raising the one-sun conversion efficiency of iii-v/si solar cells to 32.8% for two junctions and 35.9% for three junctions. *Nature Energy*, 2(9):17144, 2017.
- [35] Arvind Shah, Pedro Torres, Reto Tscharnner, Nicolas Wyrsh, and Herbert Keppner. Photovoltaic technology: the case for thin-film solar cells. *science*, 285(5428):692–698, 1999.
- [36] KL Chopra, PD Paulson, and V Dutta. Thin-film solar cells: an overview. *Progress in Photovoltaics: Research and applications*, 12(2-3):69–92, 2004.
- [37] David Redfield. Multiple-pass thin-film silicon solar cell. *Applied Physics Letters*, 25(11):647–648, 1974.
- [38] Simeon C Baker-Finch and Keith R McIntosh. Reflection of normally incident light from silicon solar cells with pyramidal texture. *Progress in Photovoltaics: Research and Applications*, 19(4):406–416, 2011.
- [39] Keith R. McIntosh, Malcolm D. Abbott, and Ben A. Sudbury. Ray tracing isotextured solar cells. *Energy Procedia*, 92:122 – 129, 2016. Proceedings of the 6th International Conference on Crystalline Silicon Photovoltaics (SiliconPV 2016).
- [40] A.W. Smith and A. Rohatgi. Ray tracing analysis of the inverted pyramid texturing geometry for high efficiency silicon solar cells. *Solar Energy Materials and Solar Cells*, 29(1):37 – 49, 1993.
- [41] Benjamin Lipovšek, Janez Krč, and Marko Topič. Optical model for thin-film photovoltaic devices with large surface textures at the front side. *Informacije Midem*, 41(4):264–271, 2011.

-
- [42] Emily D Kosten, Jackson H Atwater, James Parsons, Albert Polman, and Harry A Atwater. Highly efficient gaas solar cells by limiting light emission angle. *Light: Science & Applications*, 2(1):e45, 2013.
- [43] Jo Gjessing and Erik S Marstein. Optical performance of solar modules. *Energy Procedia*, 38:348–354, 2013.
- [44] Rolf Brendel. Coupling of light into mechanically textured silicon solar cells: A ray tracing study. *Progress in Photovoltaics: Research and Applications*, 3(1):25–38, 1995.
- [45] Mark L Brongersma, Yi Cui, and Shanhui Fan. Light management for photovoltaics using high-index nanostructures. *Nature materials*, 13(5):451, 2014.
- [46] Dennis M Callahan, Jeremy N Munday, and Harry A Atwater. Solar cell light trapping beyond the ray optic limit. *Nano letters*, 12(1):214–218, 2012.
- [47] Zongfu Yu, Aaswath Raman, and Shanhui Fan. Fundamental limit of nanophotonic light trapping in solar cells. *Proceedings of the National Academy of Sciences*, 107(41):17491–17496, 2010.
- [48] Peter N. Saeta, Vivian E. Ferry, Domenico Pacifici, Jeremy N. Munday, and Harry A. Atwater. How much can guided modes enhance absorption in thin solar cells? *Opt. Express*, 17(23):20975–20990, Nov 2009.
- [49] Albert Polman and Harry A Atwater. Photonic design principles for ultrahigh-efficiency photovoltaics. *Nature materials*, 11(3):174, 2012.
- [50] Jonathan Grandidier, Dennis M. Callahan, Jeremy N. Munday, and Harry A. Atwater. Light absorption enhancement in thin-film solar cells using whispering gallery modes in dielectric nanospheres. *Advanced Materials*, 23(10):1272–1276, 2011.
- [51] Jonathan Grandidier, Raymond A Weitekamp, Michael G Deceglie, Dennis M Callahan, Corsin Battaglia, Colton R Bukowsky, Christophe Ballif, Robert H Grubbs, and Harry A Atwater. Solar cell efficiency enhancement via light trapping in printable resonant dielectric nanosphere arrays. *physica status solidi (a)*, 210(2):255–260, 2013.
- [52] Erik Garnett and Peidong Yang. Light trapping in silicon nanowire solar cells. *Nano letters*, 10(3):1082–1087, 2010.
- [53] Patrick Campbell and Martin A Green. Light trapping properties of pyramidally textured surfaces. *Journal of Applied Physics*, 62(1):243–249, 1987.
- [54] Yi-Fan Huang, Surojit Chattopadhyay, Yi-Jun Jen, Cheng-Yu Peng, Tze-An Liu, Yu-Kuei Hsu, Ci-Ling Pan, Hung-Chun Lo, Chih-Hsun Hsu, Yuan-Huei Chang, et al. Improved broadband and quasi-omnidirectional anti-reflection properties with biomimetic silicon nanostructures. *Nature nanotechnology*, 2(12):770, 2007.

-
- [55] Xiaogang Liu, Paul R Coxon, Marius Peters, Bram Hoex, Jacqueline M Cole, and Derek J Fray. Black silicon: fabrication methods, properties and solar energy applications. *Energy & Environmental Science*, 7(10):3223–3263, 2014.
- [56] Barbara Fazio, Pietro Artoni, Maria Antonia Iatì, Cristiano D’andrea, Maria Josè Lo Faro, Salvatore Del Sorbo, Stefano Pirotta, Pietro Giuseppe Gucciardi, Paolo Musumeci, Cirino Salvatore Vasi, et al. Strongly enhanced light trapping in a two-dimensional silicon nanowire random fractal array. *Light: Science & Applications*, 5(4):e16062, 2016.
- [57] Corsin Battaglia, Ching-Mei Hsu, Karin Söderström, Jordi Escarré, Franz-Josef Haug, Mathieu Charrière, Mathieu Boccard, Matthieu Despeisse, Duncan T. L. Alexander, Marco Cantoni, Yi Cui, and Christophe Ballif. Light trapping in solar cells: Can periodic beat random? *ACS Nano*, 6(3):2790–2797, 2012.
- [58] Eli Yablonovitch. Statistical ray optics. *J. Opt. Soc. Am.*, 72(7):899–907, Jul 1982.
- [59] Marina Mariano, Gregory Kozyreff, Luis G. Gerling, Pablo Romero-Gomez, Joaquim Puigdollers, Jorge Bravo-Abad, and Jordi Martorell. Intermittent chaos for ergodic light trapping in a photonic fiber plate. *Light Sci Appl.*, 5:e16216, Dec 2016.
- [60] Guillermo Martínez-Denegri, Silvia Colodrero, Quan Liu, Johann Toudert, Gregory Kozyreff, and Jordi Martorell. Ergodic light propagation in a half-cylinder photonic plate for optimal absorption in perovskite solar cells. *Advanced Optical Materials*, 7(10):1900018, 2019.
- [61] H. Poincaré. Introduction. *Acta Math.*, 13(1-2):5–7, 1890.
- [62] Institut Mittag-Leffler. From order to chaos: The prize competition in honour of king oscar ii. <http://www.mittag-leffler.se/library/henri-poincare>. Accessed: 2019-09-11.
- [63] J. v. Neumann. Proof of the quasi-ergodic hypothesis. *Proceedings of the National Academy of Sciences*, 18(1):70–82, 1932.
- [64] John William Strutt Rayleigh. *The Theory of Sound*. Macmillan, 1877.
- [65] Hadamard. Les surfaces à courbures opposées et leurs lignes géodésiques. *Journal de Mathématiques Pures et Appliquées*, 4:27–74, 1898.
- [66] Ya. G. Sinai. On the foundations of the ergodic hypothesis for a dynamical system of statistical mechanics. *Dokl. Akad. Nauk SSSR*, 153(6):1261–1264, 1963.
- [67] L. A. Bunimovich. On ergodic properties of certain billiards. *Functional Analysis and Its Applications*, 8(3):254–255, Jul 1974.

-
- [68] L. A. Bunimovich. On the ergodic properties of nowhere dispersing billiards. *Communications in Mathematical Physics*, 65(3):295–312, Oct 1979.
- [69] LA Bunimovich. Decay of correlations in dynamical systems with chaotic behavior. *Zh. Eksp. Teor. Fiz*, 89:1452–1471, 1985.
- [70] GS Ezra, Klaus Richter, G Tanner, and D Wintgen. Semiclassical cycle expansion for the helium atom. *Journal of Physics B: Atomic, Molecular and Optical Physics*, 24(17):L413, 1991.
- [71] D. Wintgen, K. Richter, and G. Tanner. The semiclassical helium atom. *Chaos*, 2(1):19–33, 1992.
- [72] M. C. Gutzwiller. *Chaos in Classical and Quantum Mechanics*. Springer, New York, 1990.
- [73] Martin C Gutzwiller. Phase-integral approximation in momentum space and the bound states of an atom. *Journal of mathematical Physics*, 8(10):1979–2000, 1967.
- [74] Martin C Gutzwiller. Phase-integral approximation in momentum space and the bound states of an atom. ii. *Journal of Mathematical Physics*, 10(6):1004–1020, 1969.
- [75] Martin C Gutzwiller. Energy spectrum according to classical mechanics. *Journal of Mathematical Physics*, 11(6):1791–1806, 1970.
- [76] Martin C. Gutzwiller. Periodic orbits and classical quantization conditions. *Journal of Mathematical Physics*, 12(3):343–358, 1971.
- [77] Eugene P. Wigner. Characteristic vectors of bordered matrices with infinite dimensions. *Annals of Mathematics*, 62(3):548–564, 1955.
- [78] A. M. Lane, R. G. Thomas, and E. P. Wigner. Giant resonance interpretation of the nucleon-nucleus interaction. *Phys. Rev.*, 98:693–701, May 1955.
- [79] F. Haake. *Quantum Signatures of Chaos*. Springer, Berlin, third edition, 2010.
- [80] M. L. Mehta. *Random Matrices and the Statistical Theory of Energy Levels*. Academic press, second edition, 1991.
- [81] M L. Mehta and J Des Cloizeaux. The probabilities for several consecutive eigenvalues of a random matrix. *Indian Journal of Pure & Applied Mathematics*, 3, 01 1972.
- [82] Michael Victor Berry. *Classical Chaos and Quantum Eigenvalues*, chapter 11, pages 341–348. Springer US, Boston, MA, 1988.
- [83] O. Bohigas, M. J. Giannoni, and C. Schmit. Characterization of chaotic quantum spectra and universality of level fluctuation laws. *Phys. Rev. Lett.*, 52:1–4, Jan 1984.
-

-
- [84] H.-J. Stöckmann. *Quantum Chaos: An Introduction*. Cambridge University Press, Cambridge, 2000.
- [85] R Blümel, IH Davidson, WP Reinhardt, H Lin, and M Sharnoff. Quasilinear ridge structures in water surface waves. *Physical Review A*, 45(4):2641, 1992.
- [86] C. Ellegaard, T. Guhr, K. Lindemann, J. Nygård, and M. Oxborrow. Symmetry breaking and spectral statistics of acoustic resonances in quartz blocks. *Phys. Rev. Lett.*, 77:4918–4921, Dec 1996.
- [87] Hui Cao and Jan Wiersig. Dielectric microcavities: Model systems for wave chaos and non-hermitian physics. *Rev. Mod. Phys.*, 87:61–111, Jan 2015.
- [88] Jung-Wan Ryu and Martina Hentschel. Designing coupled microcavity lasers for high-q modes with unidirectional light emission. *Opt. Lett.*, 36(7):1116–1118, Apr 2011.
- [89] P. Gaspard. Quantum chaotic scattering. *Scholarpedia*, 9(6):9806, 2014. revision #143296.
- [90] Holger Kantz and Peter Grassberger. Repellers, semi-attractors, and long-lived chaotic transients. *Physica D: Nonlinear Phenomena*, 17(1):75–86, 1985.
- [91] Leo P. Kadanoff and Chao Tang. Escape from strange repellers. *Proceedings of the National Academy of Sciences of the United States of America*, 81(4):1276–1279, 1984.
- [92] Eduardo G Altmann. Emission from dielectric cavities in terms of invariant sets of the chaotic ray dynamics. *Physical Review A*, 79(1):013830, 2009.
- [93] Celso Grebogi, Edward Ott, and James A Yorke. Fractal basin boundaries, long-lived chaotic transients, and unstable-unstable pair bifurcation. *Physical Review Letters*, 50(13):935, 1983.
- [94] Alexander Eberspächer, Jörg Main, and Günter Wunner. Fractal weyl law for three-dimensional chaotic hard-sphere scattering systems. *Physical Review E*, 82(4):046201, 2010.
- [95] WT Lu, Srinivas Sridhar, and Maciej Zworski. Fractal weyl laws for chaotic open systems. *Physical review letters*, 91(15):154101, 2003.
- [96] Edward Ott and Tamás Tél. Chaotic scattering: An introduction. *Chaos: An Interdisciplinary Journal of Nonlinear Science*, 3(4):417–426, 1993.
- [97] Jesús M Seoane and Miguel A F Sanjuán. New developments in classical chaotic scattering. *Reports on Progress in Physics*, 76(1):016001, dec 2012.
- [98] Pierre Gaspard and Stuart A. Rice. Scattering from a classically chaotic repeller. *The Journal of Chemical Physics*, 90(4):2225–2241, 1989.

-
- [99] Pierre Gaspard and Stuart A Rice. Exact quantization of the scattering from a classically chaotic repeller. *The Journal of chemical physics*, 90(4):2255–2262, 1989.
- [100] Pierre Gaspard and Stuart A Rice. Semiclassical quantization of the scattering from a classically chaotic repeller. *The Journal of chemical physics*, 90(4):2242–2254, 1989.
- [101] B Eckhardt. Fractal properties of scattering singularities. *Journal of Physics A: Mathematical and General*, 20(17):5971, 1987.
- [102] Luise Couchman, Edward Ott, and Thomas M Antonsen Jr. Quantum chaos in systems with ray splitting. *Physical Review A*, 46(10):6193, 1992.
- [103] Reinhold Blümel, TM Antonsen Jr, Bertrand Georgeot, Edward Ott, and RE Prange. Ray splitting and quantum chaos. *Physical Review E*, 53(4):3284, 1996.
- [104] R. Blümel, P. M. Koch, and L. Sirko. Ray-splitting billiards. *Foundations of Physics*, 31(2):269–281, Feb 2001.
- [105] A. Kohler, G. H. M. Killesreiter, and R. Blümel. Ray splitting in a class of chaotic triangular step billiards. *Phys. Rev. E*, 56:2691–2701, Sep 1997.
- [106] A Kohler and R Blümel. Weyl formulas for quantum ray-splitting billiards. *Annals of Physics*, 267(2):249–280, 1998.
- [107] RN Oerter, E Ott, TM Antonsen Jr, and P So. Spectral statistics for quantum chaos with ray splitting. *Physics Letters A*, 216(1-5):59–66, 1996.
- [108] Jenny Nelson. *The Physics of Solar Cells*. Imperial College Press, 2004.
- [109] A Luque, A Martí, N López, E Antolin, E Cánovas, C Stanley, C Farmer, LJ Caballero, L Cuadra, and JL Balenzategui. Experimental analysis of the quasi-fermi level split in quantum dot intermediate-band solar cells. *Applied Physics Letters*, 87(8):083505, 2005.
- [110] Charles Kittel. *Introduction of Solid State Physics 8th ed.* John Wiley & Sons, Inc., 2005.
- [111] L. Sirko, P. M. Koch, and R. Blümel. Experimental identification of non-newtonian orbits produced by ray splitting in a dielectric-loaded microwave cavity. *Phys. Rev. Lett.*, 78:2940–2943, Apr 1997.
- [112] Frank L Pedrotti, Leno M Pedrotti, and Leno S Pedrotti. *Introduction to Optics*. Pearson Education, inc., third edition, 2007.
- [113] Edward Ott. *Chaos in Dynamical Systems*. Cambridge University Press, Cambridge, 1993.
- [114] Benoit Mandelbrot. How long is the coast of britain? statistical self-similarity and fractional dimension. *Science*, 156(3775):636–638, 1967.
-

-
- [115] Heinz-Otto Peitgen, Hartmut Jürgens, and Dietmar Saupe. *Chaos and fractals: new frontiers of science*. Springer Science & Business Media, 2006.
- [116] Brian Klinkenberg. A review of methods used to determine the fractal dimension of linear features. *Mathematical Geology*, 26(1):23–46, Jan 1994.
- [117] Larry S Liebovitch and Tibor Toth. A fast algorithm to determine fractal dimensions by box counting. *physics Letters A*, 141(8-9):386–390, 1989.
- [118] T.G. Smith, G.D. Lange, and W.B. Marks. Fractal methods and results in cellular morphology — dimensions, lacunarity and multifractals. *Journal of Neuroscience Methods*, 69(2):123 – 136, 1996.



Exact ray theory for the calculation of the optical generation rate in optically thin solar cells



M.A. Brandsrud^{a,1}, E. Seim^{a,*,1}, R. Lukacs^a, A. Kohler^a, E.S. Marstein^{c,d}, E. Olsen^a, R. Blümel^b

^a Norwegian University of Life Sciences, Faculty of Science and Technology, Drøbakveien 31, 1432 Ås, Norway

^b Wesleyan University, Department of Physics, 265 Church Street, Middletown, 06459, CT, USA

^c Institute for Energy, Department of Solar Energy, Instituttveien 18, 2007, Kjeller, Norway

^d University of Oslo, Department of Physics, Gunnar Randers vei 19, 2007, Kjeller, Norway

ABSTRACT

There is a profound duality between rays and waves. In fact, 70 years ago, in the context of quantum mechanics, Feynman showed that rays, properly equipped with phases and correctly summed, provide exact solutions of the quantum mechanical wave equation. In this paper, constructing explicit, exact ray solutions of the one-dimensional Helmholtz equation as a model for optically thin solar cells, we show that the ray-wave duality is also exact in the context of the electromagnetic wave equations. We introduce a complex index of refraction in order to include absorption. This has so far not been treated in the quantum ray-splitting literature. We show that inclusion of exact phases is mandatory and that a ray theory without phases may result in amplitude errors of up to 60%. We also show that in the case of multi-layered solar cells the correct summation order of rays is important. Providing support for the notion that rays provide the “skeleton” of electromagnetic waves, we perform a Fourier transform of the (experimentally measurable) solar cell reflection amplitude, which reveals the rays as peaks in the optical path length spectrum. An application of our exact ray theory to a silicon solar cell is also provided. Treating the one-dimensional case exactly, our paper lays the foundation for constructing exact ray theories for application to solar cell absorption cross section in two and three dimensions.

1. Introduction

In the quest for cheaper and cheaper solar cells, the solar cell community is continuously on the lookout for ways to decrease material costs. It is well known that in order to produce thinner solar cells with the same absorption properties as their thicker counterparts, absorption of optically thin solar cells may be enhanced by the use of nano-layering or by nano-structuring [1,2]. In order to investigate the nature of the absorption enhancement of optically thin solar cells by nano-layering or structuring, full wave calculations have been employed [3,4]. Shape resonances such as whispering gallery modes in spherical nanostructures have been considered as one possible cause for the absorption enhancement [5]. As another possible cause for the absorption enhancement, the coupling of modes in periodic nano-structures has been considered [6]. While absorption enhancement by nano-layering and nano-structuring has been demonstrated both experimentally [7] and numerically [8], the origins of the absorption enhancement mechanisms are not completely understood. Handy tools for investigating wave propagation and absorption properties of electromagnetic radiation in complex nano-structures are required for achieving a deeper understanding.

In the short wavelength limit, i.e., when the wavelength is small

compared to the size of the structures used for absorption enhancement (e.g. in micro-structured materials), ray tracing has been employed as an approach for investigating wave propagation and absorption enhancement in solar cells since the 1980s [9–11], when the optical performance of various solar cell designs was evaluated using ray-tracing techniques for the computation of the reflectance, transmittance and absorption. Since then, several numerical codes [12–19] and methods were developed, such as the Monte Carlo ray tracing method [20], the polarization ray tracing technique [21,22], the ray tracing combined with transfer matrix theory [23] and ray tracing combined with image processing [17]. Starting with one-dimensional modelling [24], these methods were later extended to two and three dimensions [25–28].

Ray tracing methods have been shown to explain the trapping of rays in solar cells. However, ray tracing fails to explain resonance effects in nano-structured materials such as whispering gallery modes. The reason for this deficiency is obvious: In order to describe resonance effects in layered thin films or films with nano-structures, the wave nature of the electromagnetic radiation needs to be taken into account, while the classical ray picture in electrodynamics is used to study the propagation of electromagnetic waves in terms of rays for cases where the wavelength of the electromagnetic radiation is short compared to changes of the media in which the electromagnetic radiation is

* Corresponding author.

E-mail address: e.seim.es@gmail.com (E. Seim).

¹ Contributions to the publication are considered equal.

propagating. This is not the case for optically thin solar cells with nano-layers and nano-structures, where the optical properties of the material change on a scale which is comparable to the wavelength of light.

In the field of quantum theory, a ray theory that takes into account the wave nature is readily available. In quantum mechanics, the ray-wave duality leads to the important field of semiclassical methods [29,30], which attempts to solve the quantum Schrödinger equation on the basis of classical particle trajectories. Using rays to solve the wave equations is tempting since it is usually much more straightforward to solve the ordinary differential equations determining the dynamics and geometry of rays, than solving the wave equations, which requires the solution of partial differential equations of continuous media. In order to obtain an exact result on the basis of rays, the rays need to be associated with phases; if for each ray the correct phases can be determined, the wave-ray duality is exact and the wave equations may be solved on the basis of rays. Since in this case, the ray theory solves the Helmholtz equation exactly, the ray theory can also correctly handle resonances caused by the wave nature of light. In addition, we introduced a complex refractive index in the ray theory allowing to treat absorption, which so far has not been introduced in quantum ray-splitting literature.

Only recently, in the field of solar cells, attempts that include phases have been reported [31].

In order to increase the understanding of the behavior of light in nano-layered and nano-structured solar cells, we present a ray theory that yields an exact description of the behavior of light in one-dimensional systems and allows to explain absorption enhancement due to nano-layering and nano-structuring.

In order to demonstrate the new theory, we study the optical generation rate of optically thin solar cells, modeled as vertical stacks of thin (absorbing) dielectric films, under normal incidence of light. In sections 2 and 3 we show that in this case, with or without a mirror behind the stack, Maxwell's vector equations are equivalent with a one-dimensional scalar Helmholtz equation, which we solve with our exact ray theory. We will use the scalar theory throughout this paper. In order to model absorption, we use a complex index of refraction. In section 4 we introduce a hierarchical scheme of summing rays as a convenient method of keeping track of rays bouncing off of and transmitting through different dielectric layers of the solar cell. We also show that including only the simplest rays already yields an excellent approximation of the exact solution of the wave equation. In Section 5 and 6 we show that both summation order and phases are important in our ray theory. We show in section 7 that the signature of the most important rays appears as peaks in the Fourier transform of the reflection amplitude of a flat solar cell. In section 8 we demonstrate how our ray theory can be used for materials with practical importance within the solar cell field. In Section 9 we discuss our results; we summarize and conclude our paper in Section 10.

Our method can be extended for use in two and three dimensions. The theory describes the optical properties of a device and is based on the imperative that phases need to be included to arrive at a useful ray theory.

2. The scalar wave model for a one-dimensional film

In order to develop a ray theory for studying absorption enhancement in optically thin solar cells, we consider one-dimensional systems in which electromagnetic radiation is propagating towards a region consisting of one or more parallel layers of different materials. In this section we will introduce one-dimensional model system that we will use for illustration throughout the paper. In all cases, we consider the propagation direction as normal to the surfaces of the materials. Since we want to develop model systems for optically thin solar cells, we study cases where one or more of the layers consist of energy-converting materials. We describe the incoming electromagnetic wave by a plane wave. Since we consider only normal incidence, the system can

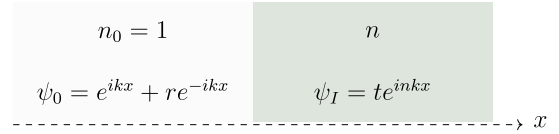


Fig. 1. Schematic description of a half-space problem, where the left half space is vacuum ($n_0 = 1$) and the right half space is material. A plane wave is propagating towards a boundary between vacuum ($n_0 = 1$) and an arbitrary dielectric material with refractive index $n = n_r + i n_i$. The imaginary part n_i of the refractive index is set to zero if the dielectric material is non-absorptive. The waves are propagating in x -direction, normal to the surface. ψ_0 and ψ_I are the scalar wave functions in the two regions, $k = 2\pi/\lambda$ is the angular wave number in vacuum, and λ is the vacuum wavelength. r and t are here the reflection and transmission amplitudes for the plane wave in this system; the amplitude of the incoming plane wave is set to one.

be fully described by a scalar wave function, ψ [32].

The first and simplest system we will investigate is a system consisting of a single film. By evaluating the scalar wave function for one single film, where the material of the film is an energy-converting material with complex refractive index $n = n_r + i n_i$, we can understand the occurrence of interference maxima and investigate how these are related to the enhancement of the absorption cross section. The interference maxima are resonances akin to the whispering gallery resonances that occur in spherical particles used for nano-structuring solar cells, which lead to an enhancement of the electric field and the absorption properties of the solar cells.

The reflection probability R at the boundary between two materials is calculated as $R_b = |r|^2$, where r is the amplitude of the reflected wave (see Fig. 1). By requiring a continuous scalar wave function and a continuous first derivative of the scalar wave function at the boundary, we can derive an expression for R_b for the case illustrated in Fig. 2 [33], i.e.,

$$R_b = \frac{(1 - n_r)^2 + n_i^2}{(1 + n_r)^2 + n_i^2}. \tag{2.1}$$

The probability for transmission at the boundary for the system in Fig. 1, T_b , is given by $T_b = |t|^2 = 1 - R_b$.

We start by evaluating two simple systems, namely a single film and a single film with a mirror, as shown in Fig. 2a and b, respectively.

We require that the wave function and its first derivative are continuous at the boundaries and that the wave function is zero at the surface of the mirror. We derive the transmission probability $T = |t|^2$ and the reflection probability $R = |r|^2$ for the systems, where t and r are the amplitudes of the transmitted and reflected plane waves, respectively. For the single-film case, shown in Fig. 2a, the reflection and transmission amplitudes are given by

$$r = \frac{i \sin(nka)[(nk)^2 - k^2]}{2nk^2 \cos(nka) - i \sin(nka)[(nk)^2 + k^2]}, \tag{2.2a}$$

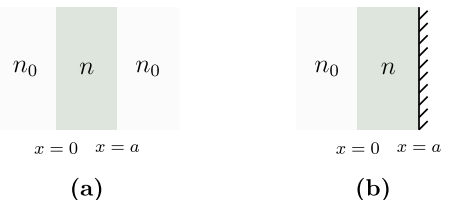


Fig. 2. Two simple film systems. (a) A single film in vacuum and (b) a single film in vacuum with a mirror. The refractive index of the film is given by $n = n_r + i n_i$. $n_0 = 1$ is the refractive index of vacuum, a is the thickness of the film.

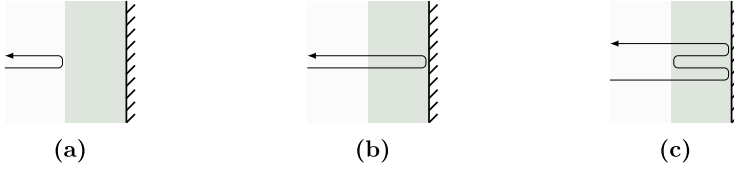


Fig. 3. Three types of rays encountered in a film-mirror system. (a) The ray directly reflects from the surface. This ray does not contribute to the absorption cross section. (b) The simplest ray that contributes to the absorption cross section. The ray enters into the film is reflected from the mirror and exits. (c) A more complex ray contributing to the absorption cross section. This ray has two reflections from the mirror and one internal reflection from the

film-vacuum boundary.

$$t = \frac{2nk^2 e^{-2ika}}{2nk^2 \cos(nka) - i \sin(nka)[(nk)^2 + k^2]} \quad (2.2b)$$

where $k = 2\pi/\lambda$ is the angular wave number in vacuum, λ is the vacuum wavelength, nk is the angular wave number in the film, n is the complex refractive index of the film, and a is the thickness of the film. If the film is non-absorptive, i.e., n is real, it is straightforward to show that Eqs. 2.2a and 2.2b lead to $R + T = |r|^2 + |t|^2 = 1$, i.e., all electromagnetic radiation entering the film is eventually leaving the film again.

In the case a mirror is present (see Fig. 2b), there is no transmission. Therefore the system can be characterized by the reflection amplitude alone, which in this case is given by

$$r = \frac{n \cos(nka) + i \sin(nka)}{n \cos(nka) - i \sin(nka)} \quad (2.3)$$

If the film is non-absorptive, i.e., n is real, it follows immediately from Eq. (2.3) that $R = |r|^2 = 1$, i.e. again all electromagnetic radiation entering the film is eventually leaving the film.

We define the *absorption cross section* as the fraction of light that is absorbed and denote it by σ . In the two cases shown in Fig. 2, the film with and without the mirror, the expressions for σ are respectively given by

$$\sigma(\lambda) = 1 - R(\lambda), \quad (2.4a)$$

$$\sigma(\lambda) = 1 - (R(\lambda) + T(\lambda)). \quad (2.4b)$$

According to the definition of σ as the fraction of absorbed light, i.e., light that does not exit the solar cell, in addition to absorbed light that leads to beneficial photo current, σ contains all parasitic absorption processes, for instance the two-photon process [34,35].

The same procedure can be applied for film-systems without mirror. For a non-absorptive film, σ is zero. For the rest of this paper, we will focus exclusively on cases where a mirror is placed behind the film/films in order to model a solar cell system.

In an equivalent solar cell system the absorption cross section is the total amount of absorbed energy absorbed at a given wavelength λ . This is the maximal amount of energy that can potentially create electron-hole pairs at a given wavelength λ . Under normal operating conditions, if the total amount of absorbed energy is increasing, the number of the photo-electrons will also increase and this will lead to enhanced efficiency. When the absorption cross section is weighted by the AM1.5 solar spectrum, we obtain the *optical generation rate*, G_{opt} . The optical generation rate G_{opt} has been introduced to the solar cell field by Ferry et al. [36]. Since then it is used as the measure of the optical performance of various solar cell designs. In our case G_{opt} is given by

$$G_{opt}(\lambda) = \Gamma_{solar}(\lambda)\sigma(\lambda)A, \quad (2.5)$$

where $\Gamma_{solar}(\lambda)$ is the spectral weighting term and A is the surface area of the solar cell. In this paper we will evaluate $\sigma(\lambda)$ for our systems in order to get a fundamental understanding of how the optical resonances in the energy converting film increase the total amount of absorbed energy.

For a single film, or a stack of films, with different refractive indices, it is possible to analytically derive a formula for the absorption cross section from the probability current. This depends only on the absolute

square of the scalar wave function inside of the film(s). To be specific, we consider the case of an array of films, described by a space-dependent complex refractive index $n(x) = n_r(x) + i n_i(x)$. The complex refractive index $n(x)$ when the optical or the absorption properties of a material change. When a stack of films is illuminated from the front and backed by a mirror, the absorption cross section is given by

$$\sigma = 2k \int_0^w n_i(x) n_r(x) |\psi(x)|^2 dx, \quad (2.6)$$

where the stack of films is assumed to be located in the interval $0 \leq x \leq w$ and the mirror is located at $x = w$. The details of the derivation are presented in Appendix B. Since for a single film with mirror both r and $\psi(x)$ are known explicitly (see Eq. (2.3) and Appendix B), it is straightforward in this case to show by explicit calculations that Eq. (2.6) holds (see Appendix C).

3. Exact ray theory for single films

In this section, we will show that it is possible to estimate the absorption cross section by considering and summing rays. Three examples of simple rays are shown in Fig. 3.

In order to calculate the total reflection amplitude r we need to sum up all possible rays in the film [37,38]. Every ray contributes to the total reflection amplitude and thereby to the absorption cross section with an amplitude and a phase. The reflection and transmission amplitudes of the ray depending on the side of the boundary the ray is hitting. Denoting by r_l and t_l the reflection and transmission amplitudes, respectively, for a ray originating from outside in the vacuum and transmitting into the film, and by r_r and t_r the reflection and transmission amplitudes, respectively, for a ray originating from inside of the film and traveling towards the vacuum, we obtain (see Appendix A):

$$r_l = \frac{1 - n}{1 + n}, \quad (3.1)$$

$$t_l = \frac{2}{1 + n}, \quad (3.2)$$

$$r_r = -\left(\frac{1 - n}{1 + n}\right), \quad (3.3)$$

$$t_r = \frac{2n}{1 + n}. \quad (3.4)$$

It is important to note that the amplitudes, eq. (3.1)–(3.4), remains exact if the refractive index, n , is complex. We hereby established a ray model that is able to describe absorption of electromagnetic radiation. In addition to the amplitudes, we need to include the phase that the ray collects when it transverses the film, i.e., each time it travels from the vacuum-film interface to the mirror or from the mirror to the interface. This phase collected when traveling through the distance a is given by e^{inka} . Further we have to include the phase $e^{i\pi}$ [39] caused by the mirror each time a ray is reflected by the mirror.

To introduce our procedure, we state the contribution to r from the three selected rays illustrated in Fig. 3. The result is

$$r = r_l + t_l e^{inka} e^{i\pi} e^{inka} t_r + t_l e^{inka} e^{i\pi} e^{inka} r_r e^{inka} e^{i\pi} e^{inka} t_r, \quad (3.5)$$

where the first term is the contribution of the ray illustrated in Fig. 3a,

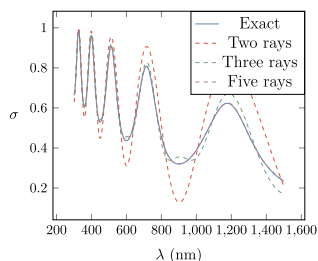


Fig. 4. Absorption cross section σ as a function of the wavelength λ for the system given in Fig. 2a. The blue line is calculated analytically with Eq. (2.3) and the ray model with Eq. (3.6) is used when the two (red dashed), three (green dashed line) and five (purple dashed line) simplest rays are included. The refractive index of the film in this system is $1.8 + 0.05i$ and the thickness is 500 nm. The wavelength ranges from 300 nm to 1500 nm. (For interpretation of the references to color in this figure legend, the reader is referred to the Web version of this article.)

the second term is the contribution from the ray illustrated in Fig. 3b, and the third term is the contribution from the ray illustrated in Fig. 3c. If we include all contributing rays, their total, exact contribution to r is given by

$$r = \eta + t_l t_r e^{i\pi} \sum_{\nu=0}^{\infty} (e^{i\pi} r_r e^{2i\pi k a})^{\nu}. \tag{3.6}$$

By inserting the expressions for r_l , t_b , r_r , and t_r , and with the help of the elementary summation formula for the geometric series, it turns out that r in Eq. (3.6) is equal to r in Eq. (2.3).

Whenever an energy-converting film is present, i.e., whenever $n_r > 1$, we have $|r_r| < 1$ and the expression for r in Eq. (3.6) converges absolutely. Fig. 4 shows σ for the single film system with a mirror behind. The solid line is the exact expression for σ , the dashed line is σ found by the ray model where only a few simple rays are included.

As shown in Fig. 4 very fast convergence is observed even if only a few of the shortest rays are included. The figure also shows that considering only the five simplest rays in the system, the analytically calculated absorption cross section can already be predicted near perfectly. Fig. 4 illustrates another important aspect, namely that our ray theory can describe absorption of electromagnetic radiation by including a complex refractive index.

4. Exact ray theory for multilayered films: hierarchical summation scheme

When a system has more than one layer, each ray, upon encountering a vacuum-film boundary or a boundary between two layers, will split into two rays, a reflected ray and a transmitted ray (except the mirror in our model system). This is called ray splitting [40–42]. With increasing geometric length, tracking splitting rays becomes an ever more complex task since each split ray, subsequently, will undergo splittings itself. Thus, the number of rays in the system increases exponentially with the number of splittings, i.e., with the geometric lengths of the rays.

In order to keep track of all the rays, we present a convenient book-keeping system, called symbolic dynamics [43]. This system is widely used in the fields of non-linear dynamics and chaos. This symbolic language consists of an alphabet and simple grammatical rules which determine the path of a ray unambiguously. The symbolic dynamics of two film layers with a backside mirror (Fig. 5) has an alphabet that consists of the three letters (symbols) a , b , c . Each of the letters corresponds to a boundary where the ray will either split or simply reflect. The grammatical rules are:

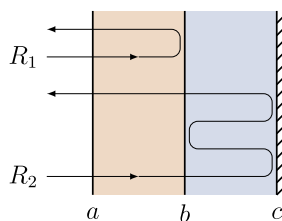


Fig. 5. Two rays, R_1 and R_2 , in a system with a mirror and two film layers. R_1 and R_2 are labeled by the symbolic dynamics aba and $abc bca$, respectively.

1. A word must start with the letter a . If the ray exits the system, the word must also end in the letter a .
2. Skipping letters is not allowed, i.e., unless the trajectory terminates, the letter a is always followed by the letter b , the letter b is always followed by letters a or c and the letter c is always followed by the letter b , indicating reflection off of the mirror.

Illustrating these rules, we construct the two sample rays R_1 and R_2 shown in Fig. 5. R_1 transmits at a and reflects at b before transmitting out of the system through a . Thus, the word labeling R_1 is aba . We may be tempted to label R_2 as aca , but this violates rule 2. The correct word, $abc bca$, contains information about every boundary crossed.

To define the symbolic dynamics of systems with more films, we simply use a larger alphabet. If there is no mirror, i.e., transmission through the system is possible, rule 1 would allow words to end with the last letter of the alphabet.

The graph in Fig. 6 generates the part of the vocabulary that contains words with seven or less symbols for the two-film system in Fig. 5. The incoming ray will first hit node a . All a nodes are colored blue to emphasize that they mark the end of a word. The edges that are connecting the nodes are either black or red. A black edge signifies a ray traveling to the right and a red edge signifies a ray traveling to the left. A word can easily be read off Fig. 6 by writing down the successive letters starting from the first node to another blue node.

The computer implementation of this hierarchical summation scheme uses the number of ray splittings at the boundaries as a measure of the run time, not the number of rays explicitly. More splitting events generate exponentially more rays to approximate the reflectance R . About seven such splittings are needed to approximate the analytic expression reasonably well as seen in Fig. 7. These seven splittings generate a set of 64 contributing rays. Allowing more splittings, thus adding more rays, improves the approximation further.

If photons were classical, Newtonian particles, ray-splitting would not occur. The only ray allowed according to Newtonian mechanics would be the ray labeled $abcba$. Accordingly, this ray is also known as the “Newtonian ray” [44]. All other rays show ray splitting [40–42]. Since ray splitting is not allowed according to Newtonian mechanics, these split rays are called “non-Newtonian” [44]. Non-Newtonian rays have been proven theoretically [40,41,45,46] and experimentally [42,47–49].

To assess the importance of the (Newtonian forbidden) non-Newtonian rays compared with the (Newtonian allowed) non-split, Newtonian ray, we also show the contribution of the Newtonian ray to $R(\lambda)$ in Fig. 7. We see that the Newtonian ray alone, although in the vicinity of the exact result for $R(\lambda)$, produces a result with very poor accuracy. Conversely, Fig. 7 shows that the contribution of the split, non-Newtonian rays is substantial, and that only the added contribution of the split, non-Newtonian rays produces accurate results.

5. Importance of the correct summation order

As discussed in the previous section, in the case of a single film, the sum in Eq. (3.6) for the reflection amplitude r is absolutely convergent,

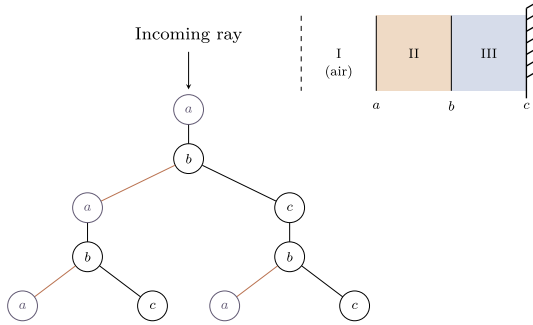


Fig. 6. Schematic of the ray tree algorithm. The interfaces between the materials II and III are labeled *a* and *b*, respectively, and the mirror is labeled *c*. An incoming ray always hits *a* first. At *a* the ray will split in two. One ray is reflected (ray labeled ‘*a*’) and the other will travel to the right (black edge) towards *b*. At *b* it can either go to the left (red edge) and exit, or continue to travel to the right to the mirror, *c*. The inset shows the two-layered system that is considered in this example. (For interpretation of the references to color in this figure legend, the reader is referred to the Web version of this article.)

and the summation order of the rays is irrelevant. Any summation scheme, as long as all rays are included, will yield the exact value for *r*. However, if there is more than one film, the order of summation does matter. Let

$$r = \sum_{j=0}^{\infty} A_j \tag{5.1}$$

be the ray representation of the reflection amplitude. If Eq. (5.1) were a finite sum, the order in which we sum the rays would clearly not matter. However, this is not the case with infinite sums, such as Eq. (5.1). Only if

$$\sum_{j=0}^{\infty} |A_j| < \infty \tag{5.2}$$

is the summation order of the terms in Eq. (5.1) irrelevant and always yields the correct reflection amplitude. In this case, as discussed in the previous section, we call the sum in Eq. (5.1) absolutely convergent. If, however,

$$\sum_{j=0}^{\infty} |A_j| = \infty, \tag{5.3}$$

it was shown by Riemann [50] that, depending on the summation order of the terms in Eq. (5.1), the infinite sum in Eq. (5.1) can be made to have any prescribed value. This is known as Riemann’s Rearrangement Theorem [51]. In this case the sum in Eq. (5.1) is called conditionally convergent, and it is necessary to sum it in some prescribed way in

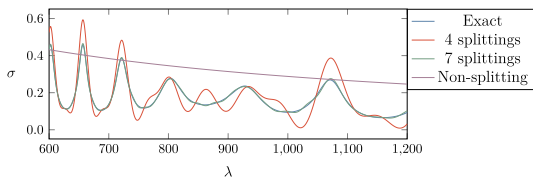


Fig. 7. Absorption cross section σ as a function of the wavelength λ , including various numbers of split rays, and the shortest non-splitting ray. The hierarchical summation scheme approximates the analytical result for the film with two layers (Fig. 5) almost perfectly with only 64 rays or, equivalently, seven splittings. Including more rays yields an even more accurate result. The non-splitting ray approximately defines the lower envelope of the exact result.

order to obtain correct results.

In Appendix D we show that for our two-film system, for a large range of dielectric constants, Eq. (5.3) holds, i.e., in these cases our ray sum in Eq. (5.1) is only conditionally convergent. The correct summation scheme in these cases is to sum the rays in the order of increasing path length, where the path length of the ray may either be its geometric length or its optical path length. This summation scheme is not dictated by mathematics, which does not help us beyond the fact of stating that in the case of conditional convergence different summation prescriptions produce different results [51], but interestingly is dictated by the physical situation. For actual realizations of solar cells there is always some absorption present, which naturally suppresses the importance of longer rays. Therefore, ordering the rays according to their importance for *r* means ordering them according to their path lengths.

We can numerically corroborate the importance of the summation order by testing for absolute convergence with the hierarchical summation scheme. We take the absolute value of each term, which is equivalent to removing the phase completely. Fig. 8 compares the absolute value of the difference between the analytical reflection probability R_A and the reflection probability R_{HSS} , computed according to the hierarchical summation scheme. Without the absolute value of each term, i.e., when phases are included, convergence is reached after a small number of splittings. Without phases, we see that the difference $|R_A - R_{HSS}|$ is diverging, numerically corroborating that the sum over rays is not absolutely convergent.

6. Importance of phases in the ray theory

In this section we emphasize the importance of phases, even in the case of absorption (which was not included in Sec. 5), by computing absorption cross sections, with and without phases included, using as an example the single film with mirror introduced in Secs. 2 and 3. Comparing the two cases, we show that the ray theory without phases produces results that contain unacceptably large errors.

In order to demonstrate the importance of the phases, we introduce the following ray model where phases are not included. Without phases, instead of being associated with an amplitude, every ray is associated with an intensity. We set the incoming intensity of the ray to I_0 . The simplest ray model we consider retains only the directly reflected ray as illustrated in Fig. 3a. We call this ray the *ray of zero length*, since it does not enter the energy-converting film, and its optical path length inside of the film, therefore, is zero. We further assume that the probability given in Eq. (2.1) describes the amount of light reflected at the surface of the film. The rest of the light is absorbed in the film. In this case the absorption depends on the wavelength of the incoming light only through the wave number, *k*, as long as the refractive index of the film is constant for all wavelengths. When we evaluate rays that travel inside of the film, the intensity assigned to a particular ray decreases via Beer-Lambert’s Law, and is expressed as

$$I = I_0 e^{-n_i kx}, \tag{6.1}$$

where I_0 is the incoming intensity of the light, which we set to 1, *x* is the distance travelled in the film [39,52], *k* is the wave number and n_i is the imaginary part of the refractive index of the film.

To find the amount of absorbed light, i.e., the absorption cross section, σ , we need to sum the contributions to the absorption from each ray. When the ray hit a boundary, a part of it will reflect and a part of it will transmit. The probability for reflection at a boundary, R_b is given in eq. (2.1) and the probability of transmission is $T_b = 1 - R_b$. Evaluating σ due to the rays in Fig. 3a and b, the result is

$$\sigma = 1 - (R_b + T_b^2 e^{-2n_i ka}), \tag{6.2}$$

where *a* is the width of the film. The expression inside the brackets is the sum of the intensities of these two reflected rays. When all possible rays are included (infinitely many), σ is given by

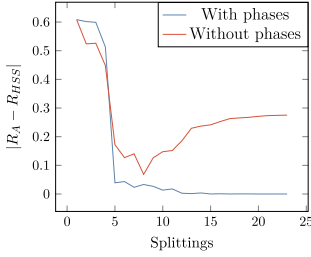


Fig. 8. Absolute value of the difference between the reflection calculated by the analytical expression, R_A , and the hierarchical summation scheme, R_{HSS} , is converging when the phase of the rays is included. The same calculation will diverge if it is done without phases.

$$\sigma = 1 - \left(R_b + \frac{T_b^2 e^{-2n_i k a}}{1 - R_b e^{-2n_i k a}} \right). \quad (6.3)$$

We arrive at this formula by summing up all possible rays and by using the elementary summation formula for the geometric series.

Fig. 9 shows a comparison of the absorption cross section evaluated with ray models that include and neglect phases, respectively. For the case in which phases are neglected, we present three different scenarios. (1) The horizontal blue line in Fig. 9 is σ computed by including only the ray of zero length (see Fig. 3a). (2) The red line in Fig. 9 is σ computed on the basis of the two rays in Fig. 3a and b (Eq. (6.2)). (3) The green line in Fig. 9 is σ obtained by including infinitely many rays (Eq. (6.3)). Contrasting these three cases, computed without including phases, we also show the exact result for σ in Fig. 9, where we have included infinitely many rays *with phases* (purple line). The exact result, with phases included, shows oscillations (purple line), which are not captured by either of the three cases that do not include phases. As seen in Fig. 9, σ without phases is monotonically decreasing when the wavelength increases (green and red lines), without any oscillations according to Eq. (6.1). The result without phases included underestimates the exact result with phases included, and, according to Fig. 9, the relative error can exceed 60% in the wavelength region shown in Fig. 9. In the context of absorption cross sections of typical solar cells, an error of this magnitude is not acceptable. We conclude that for accurate modelling of solar-cell efficiencies in terms of rays, inclusion of phases is absolutely essential. Any ray theory, whether applied in the electromagnetic, acoustic, or quantum domains, is exact only if phases are

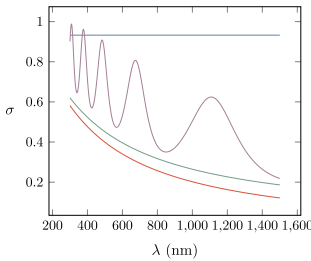


Fig. 9. Absorption cross section, σ , as a function of wavelength, λ , in the range $300 \text{ nm} \leq \lambda \leq 1500 \text{ nm}$, for a single film with refractive index $n = 1.8 + 0.05i$, a thickness of 500 nm, and a mirror on the backside of the film. The blue line is σ , including only the reflected ray of zero length (see Fig. 3a). The red line is σ , including only the two simplest rays (see Fig. 3a and b, calculated with Eq. (6.2)). The green line is σ , including infinitely many rays without phases, calculated with Eq. (6.3), and the purple line is σ , including infinitely many rays with phases. The purple line is calculated with the ray theory presented in Sec. 3. (For interpretation of the references to color in this figure legend, the reader is referred to the Web version of this article.)

included. Neglecting phases may have serious consequences, ranging from incorrect results to divergent results as demonstrated in Fig. 8 of Sec. 5.

7. Signatures of rays in the Fourier transform of the reflection amplitude

A Fourier transform of the reflection amplitude $r(k)$ allows us to reveal the signatures of the rays whose combined contributions result in the exact functional form of $r(k)$. If the entire spectral range is accessible to us, we obtain this information in the form of the *length spectrum*

$$\mathcal{F}(L) = \frac{1}{2\pi} \int_{-\infty}^{\infty} r(k) e^{-iLk} dk. \quad (7.1)$$

To illustrate, let us use the exact, explicit formula 3.6 for the reflection amplitude r of a single film with mirror. We obtain

$$\mathcal{F}(L) = n\delta(L) + \frac{t_l t_r}{r} \sum_{\nu=1}^{\infty} e^{i\nu\pi} r_{\nu}^{\nu} \delta(L - 2\nu a), \quad (7.2)$$

where $\delta(x)$ is Dirac's delta function. We see that $\mathcal{F}(L)$ is a series of sharp peaks at integer multiples of the optical path length $2na$, where each peak corresponds to the optical path length of a certain ray inside of the film. Thus, every single ray that contributes to Eq. (3.6) is represented as a sharp peak in $\mathcal{F}(L)$. This even includes the “ray of zero length”, which is the ray that reflects with amplitude r_l off of the front surface of the film. Since this ray does not enter the film, its optical path length in $\mathcal{F}(L)$, naturally, is zero. The weights of the δ terms in Eq. (7.2) correspond to the amplitudes that the rays pick up when crossing a boundary or being reflected from a boundary. Thus, the length spectrum of r contains the complete optical information of the system under consideration. This is not surprising, since the Fourier transform in Eq. (7.1), a function in L space, is complementary to the ray representation, Eq. (3.6), of r in k space. Unfortunately, ray information can be extracted so cleanly from $r(k)$ with Eq. (7.1) only if the integration range is infinite. In actual applications in solar cells, we are restricted to a finite spectral range, which turns the exact length spectrum $\mathcal{F}(L)$ into an approximate length spectrum

$$\widetilde{\mathcal{F}}(L) = \frac{1}{2\pi} \int_{k_1}^{k_2} r(k) e^{-iLk} dk. \quad (7.3)$$

Applied to our single-film example, this evaluates to

$$\begin{aligned} \widetilde{\mathcal{F}}(L) = & \frac{r_l}{2\pi} \exp\left[-i\left(\frac{k_1+k_2}{2}\right)L\right] (k_2 - k_1) \operatorname{sinc}\left[\frac{L}{2}(k_2 - k_1)\right] \\ & + \frac{t_l t_r}{2\pi r} (k_2 - k_1) \sum_{\nu=1}^{\infty} e^{i\nu\pi} r_{\nu}^{\nu} \exp\left[i\left(\frac{2\nu a - L}{2}\right)(k_1 + k_2)\right] \\ & \times \operatorname{sinc}\left[\left(\frac{2\nu a - L}{2}\right)(k_2 - k_1)\right], \end{aligned} \quad (7.4)$$

where $\operatorname{sinc}(x) = \sin(x)/x$ is the “sinc-function”. We see that in the case of a finite spectral range the sharp δ -function peaks are replaced by smooth, oscillatory sinc-functions, which produces “Gibbs ringing” [53] in $\widetilde{\mathcal{F}}(L)$ that produces copious “extra peaks” in $\widetilde{\mathcal{F}}(L)$ and may thus obscure the peaks that correspond to rays. The ringing may be reduced by the use of a window function [54], i.e., a function $w(k)$ that softly “switches on” and “switches off” the integration at k_1 and k_2 according to $w(k_1) = w(k_2) = 0$, $w'(k_1) = w'(k_2) = 0$, $w''(k_1)/k_1^2 \ll 1$, $w''(k_2)/k_2^2 \ll 1$.

As an illustrative example we present the Fourier transform of the reflection amplitude of a three-layered film with constant, non-dispersive indices of refraction, $n_1 = 1.5$, $n_2 = 1.9$, $n_3 = 2.3$, and film widths $a_1 = 500 \text{ nm}$, $a_2 = 2000 \text{ nm}$, and $a_3 = 1000 \text{ nm}$, respectively. In this example we chose $k_1 = 2\pi/1200 \text{ nm}$ and $k_2 = 2\pi/5 \text{ nm}$. We used the window function

$$w(m) = 1 - \left(\frac{m - \frac{N-1}{2}}{\frac{N-1}{2}} \right)^2, \quad (7.5)$$

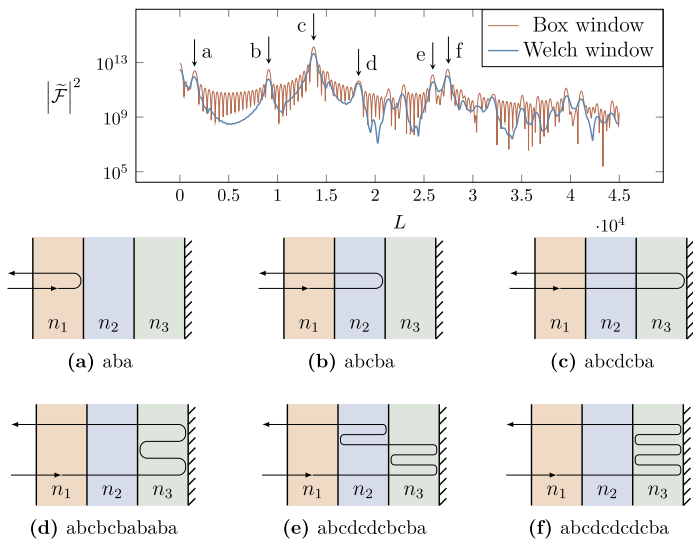


Fig. 10. Top frame: Finite-range Fourier transform (approximate length spectrum) $\tilde{\mathcal{F}}(L)$ of the exact $r(k)$ of a three-layer film system with mirror with parameters as specified in the text. $\tilde{\mathcal{F}}(L)$ shows distinct peaks, labeled (a)–(f). The rays corresponding to these peaks, including their symbolic-dynamics labels, are illustrated in the six frames (a)–(f), below the top frame, respectively. These six rays make the most important contributions in the ray-representation of $r(k)$ of this system.

called the Welch window function. Here m is an integer variable that corresponds to the grid used in the calculations. If we are using M different values of k , m takes the values $0 \leq m \leq M - 1$. Using no window (box window) shows Gibbs phenomenon very clearly. The resulting length spectrum of this three-layer system is displayed in Fig. 10. In general, a larger Fourier peak indicates a more important component in a Fourier series. Hence, the heights of the peaks in Fig. 10 directly relate to the importance of the contributions of the corresponding rays to r . The peaks labeled a-f in Fig. 10 correspond to the rays illustrated in (a) - (f) of Fig. 10, respectively. The six tallest peaks correspond to rays labeled by the words *aba*, *abcb*, *abcdcb*, *abcba*, *abcdcbcb*, and *abcdcdcbcb*, respectively. The peaks in Fig. 10 are located at the optical path lengths of the rays, i.e., they are located at the linear combinations $2\nu_1 n_1 a_1 + 2\nu_2 n_2 a_2 + 2\nu_3 n_3 a_3$, where ν_j , n_j , and a_j are the repetition number, index of refraction, and width of layer number j , respectively.

As shown in this section, whenever we have $r(k)$, either analytically or numerically calculated, or experimentally determined, a Fourier transform of $r(k)$ reveals the peaks of the corresponding multi-layer system, a technique we call *ray spectroscopy*. The peak heights will tell us which of the rays are the most important in determining the reflection amplitude r , which, in turn, determines the absorption cross

section of the corresponding solar cell. As shown in Fig. 10, the peak height is an exponentially decreasing function of optical path length, which means that only a few of the shortest rays are necessary to determine $r(k)$ with sufficient accuracy to be useful for system optimization. This, in turn, enables us to design and optimize solar cells in a completely new way on the basis of a few important rays, which implies a very small parameter space to be searched for system optimization.

8. Example with silicon

To provide an example of the ray-wave equivalence and the hierarchical summation scheme, we analyzed a three-layer simplification of a five-layer optically thin, epitaxial crystalline silicon solar cell using experimentally determined indices of refraction [55–58]. Fig. 11 shows the layer structure for these two models. The intent with the simple three-layer design is to demonstrate the concepts described in this paper applied to a system with material constants of practical importance. However, it should be noted that solar cells with co-planar structure are mainly used to provide an example. Commercial solar cells usually have some kind of surface structure to lower the reflectivity.

Since both the two amorphous silicon (a-Si) layers and the two crystalline silicon (c-Si) layers in the experimentally realized solar cell

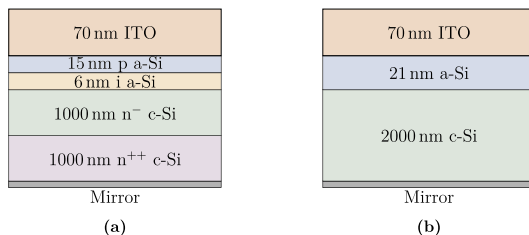


Fig. 11. Multilayer solar cells with mirror. (a) Experimentally realized thin epitaxial crystalline silicon solar cell consisting of five layers [55]. (b) Three-layer simplified model of the experimental system shown in (a), obtained by replacing layers with different doping but approximately the same index of refraction by a single layer. The three layers are, from top to bottom, 70 nm ITO, 21 nm amorphous silicon, and 2000 nm intrinsic silicon, respectively.

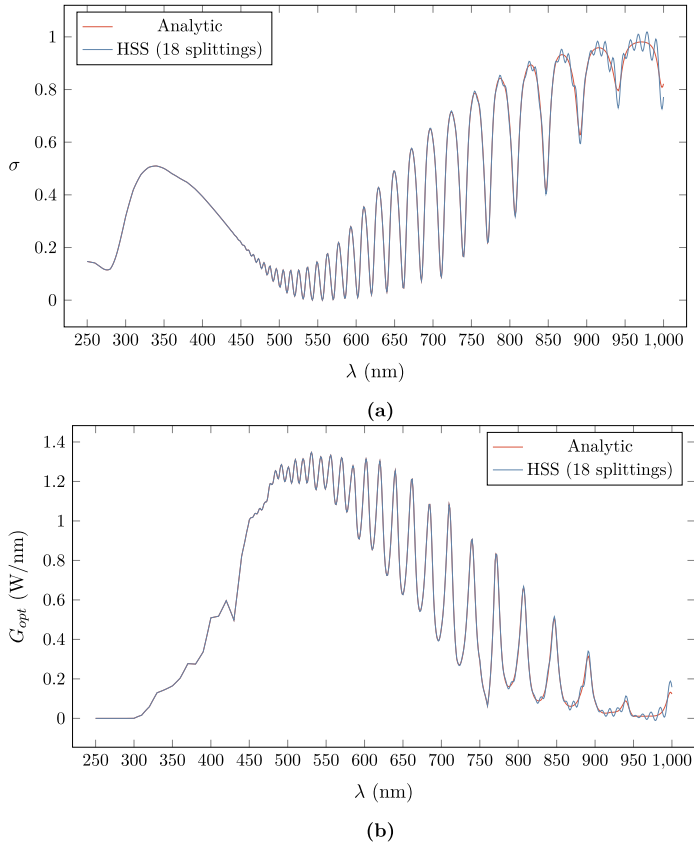


Fig. 12. a) A comparison of the absorption cross section σ calculated from an analytic expression and with a finite number of rays, using the hierarchical summation scheme (HSS). 18 splittings produce 65,537 rays and gives a good approximation to the analytic expression. b) When the AM1.5 solar spectrum [59] is taken into account, we get the optical generation rate, G_{opt} .

differ only in their doping, and since we for now neglect the doping-dependent free carrier absorption, we modeled this solar cell in terms of a three-layer system by collapsing the two a-Si layers and the two c-Si layers into a single layer, respectively.

Fig. 12a shows a comparison between the analytical result (red line) for the absorption cross section σ and the result produced by the hierarchical summation scheme (blue line). In the lower wavelength regime, σ is perfectly approximated by the hierarchical summation scheme including 18 splittings or 65,537 rays. Only from 750 nm do we start to see some deviations. This demonstrates the complexity of a three-layer film in terms of its ray dynamics, and highlights the power of the hierarchical summation scheme even in the case of dispersive indices of refraction.

In order to obtain the optical generation rate [59], Eq. (2.5), we multiply σ with the AM1.5 solar spectrum, I . The result is displayed in Fig. 12b for both the analytical expression (red line) and the hierarchical summation scheme (blue line), corresponding to the two corresponding cases shown in Fig. 12a, respectively.

Once more, we see excellent agreement between optical generation rate obtained on the basis of the analytical and hierarchical summation scheme results.

9. Discussion

As shown in section 3, there is a profound duality between waves and rays. Rays are governed by ordinary differential equations, describing particle motion, while wave fronts are the solutions of continuous wave equations expressed in the language of partial differential equations. This duality is exploited in many fields of physics that deal with waves. In optics, e.g., it leads to the important field of geometric optics [60] in which one attempts to obtain an accurate description of the passage of light through various optical components by using a ray picture, side-stepping the more involved solution of Maxwell's wave equations [39,61]. There are many examples where the wave-ray duality is exact (see, e.g., [30]) and may be exploited to advantage. The most important example is Feynman's path integrals [62], which solve the full wave-mechanical problem of quantum mechanics exactly by summing over all possible classical rays. Another example of exact ray solutions to the corresponding wave problem is quantum mechanics with energy-scaling step potentials in one dimension [63–65]. Since the quantum step-potential problem and the electromagnetic (E&M) optically thin solar-cell problem are formally identical problems, one of the intentions of this paper is to transfer and adapt methodology from the quantum chaos community in the field of one-dimensional energy-scaling step potentials and dressed quantum graphs [64,65] to the solar-

cell community, who is concerned with the solution of Maxwell's equations for stacks of layers of anti-reflection coatings on top of energy-converting materials. We note that, so far, only the bound-state problem has been studied extensively in the context of dressed, scaling quantum graphs, which, in the optical case, would correspond to the presence of two mirrors, one at the front and one at the back of the stack of films. The scattering problem, as studied in this paper, has to our knowledge not yet been studied in the context of dressed, scaling quantum graphs.

For the one-dimensional case we derived the exact expression for the *absorption cross section*, σ , of the energy-converting material. When σ is weighed by the solar spectrum as the spectral weighting term, the *optical generation rate* is obtained. This brings out the connection between the structure of the wave function ψ and the absorption. By evaluating σ we can engineer our system to increase the absorption, and thus the absorption cross section, of the system.

We showed the importance of including phases in our ray theory with the help of the following two-step method. First, we include the exact phases of the rays in our one-dimensional model, which we take as consisting of a single film. In section 3 we demonstrate that this yields the exact solution of the Helmholtz equation. Then, we evaluated the ray sum for this one-dimensional systems setting all phases to 1. We showed in Section 5 that the resulting, incorrect ray theory cannot handle the resonances and in addition predicts a spectral optical generation rate that is up to 60% off. We are convinced that this observation carries over to any ray tracing in two and three dimensions, which means that in order to be confident in the accuracy of a ray-tracing result, phases *must* be included. Otherwise, as shown in our paper in the one-dimensional case, one should be prepared for large errors in the predictions of a ray theory that omits phases.

For several of our model systems, including our example of the lab silicon cell discussed in section 8, we showed that including only a few rays in the ray sum already gives a good approximation of the absorption cross section (see, e.g., Fig. 4. This observation is important since, in principle, an infinity of rays needs to be summed over in order to obtain exact results, and if the convergence were slow, this would result in an enormous number of terms to be summed, partially, or totally, cancelling out the advantage in computational speed of rays over waves. That only a few dominant rays already determine the final result with good accuracy is particularly important in two and three dimensions, since, according to the increased dimension, the set of rays that needs to be summed over is much larger.

Since our ray theory is exact, it works for all refractive indices, n . This includes all n typically encountered in solar cells, where complex n indicates an absorptive material. A strength of the ray theory is that the refractive index can have any value and is not limited to only small values of real and imaginary parts. Our ray theory is therefore applicable to any solar cell material. Including the temperature dependence of its index of refraction. In linear approximation, as a function of temperature T , we can write

$$n(T) = n_0(T_0) + \beta(T - T_0), \quad (9.1)$$

where n_0 is the complex index of refraction at a reference temperature T_0 and β is the complex temperature coefficient, combining the two temperature coefficients for the real and imaginary parts of the index of refraction. Since our theory is exact for all indices of refraction, our theory can accommodate exactly the temperature dependence of the index of refraction, described by the temperature coefficients. In addition, since our complex index of refraction models the effects of the band gap and any gain and loss mechanisms, their temperature dependence, via the complex index of refraction, is included as well. We would also like to point out here that complex indices of refraction have so far not been treated in the quantum ray-splitting literature. Therefore our paper is the first to show that a complex index of refraction does not invalidate the exactness of the ray theory.

In our theory the boundary conditions between the vacuum and

dielectric films, and between different dielectric films, are treated exactly, without any approximations. Only the boundary condition between the energy-converting dielectric film and the mirror is idealized, assuming 100% reflection. This assumption is not necessary since the mirror can be treated as another dielectric layer [39] for which our theory is exact.

Two-dimensional materials are of great current interest (see, e.g., [66,67]). Since the dielectric properties of these materials have already been measured [68], reflection and transmission amplitudes of these two-dimensional materials can be computed. Once these amplitudes are known, our theory is applicable to these materials and stays exact.

We do not hesitate to point out that for one-dimensional systems wave calculations are cheaper than ray calculations. For one-dimensional multi-layer systems, the transfer matrix method [69] can be used, which is fast and includes absorption. Even in two dimensions, solving the wave equation might still be cheaper and faster than applying the ray theory. In three dimensions, however, supported by the fact that an extensive literature on ray-tracing in three dimensions exists [15,16,27,28], we believed that ray methods will have an edge, in particular when constructed with phases included, which renders them exact.

In addition to paving the way toward an exact and efficient ray theory in three dimensions, the emphasis of this work is to present a ray theory that can be used to understand the different mechanisms that may be used to improve the absorption cross section. The fact that only a few rays describe the absorption cross section, σ , of the system is encouraging since only a few parameters (rays) need to be optimized for optimizing the entire system. Consequently, there are two ways in which classical ray calculations can be used in the context of solar cells: (1) As a predictive tool used to predict the outcomes of wave calculations (predictive direction; forward model) and (2) as a means to understand the results of wave calculations, in particular to illuminate and illustrate the mechanisms by which enhancement of the absorption cross section is achieved (analysis direction).

In the case of a single film, we showed in section 5 that the ray sum is absolutely convergent. Therefore, the terms in the sum may be summed in any order. In the case of stacks of two or more films, however, we showed in section 5 that the resulting ray sum is only conditionally convergent. In this case the order of summation is important, since, according to Riemann [50,70], any result can be obtained from a conditionally convergent sum by cleverly re-ordering the terms. In section 4 we present a hierarchical scheme according to which the rays in a multi-layer system can be summed in correct order.

The dominant rays describing the system can be found by performing the Fourier transform of σ . Thus, the Fourier transform provides us with the possibility of extracting ray information from σ . It is important to use a windowed Fourier transform (requiring a switching function) to eliminate the Gibbs ringing, which produces spurious peaks in the Fourier transform that do not correspond to rays. We found that rays are connected to the absorption cross section. The longer the rays, the larger the absorption cross section. The Fourier transform gives us the ability to study the dominant rays. By increasing the dominance of the long rays, which have the largest contribution to the absorption, it is possible to design solar cells to have an increased absorption cross section.

In section 8 we study a realistic system with a refractive index that exhibits dispersion. We showed that even dispersion is no obstacle to our theory; it still provides us with the correct absorption cross section.

Sunlight is incoherent and the question arises whether our results, derived for coherent light, are relevant for illumination of solar cells with incoherent light. We answer this question in the affirmative, since what we evaluate is the absorption cross section, which is defined for a sharp frequency, associated with an infinite coherence length. Another way to see this is the following. On the microscopic level, it is individual photons that strike the solar cell and interact with it. While different photons certainly have different frequencies, each individual

photon has a sharp frequency and a corresponding wave function that is the solution of the optical Helmholtz equation. Thus, at each individual frequency, it is indeed the Helmholtz equation that governs the absorption of photons and thus determines the absorption cross section. The total optical generation rate is then obtained by a simple integral over the absorption cross sections weighted with the solar spectrum. Thus, our theory, despite the fact that sun light is incoherent, works for all film thicknesses.

10. Conclusions

In this paper we have shown that the ray theory is exact in one dimension. Our results are important since they pave the way to the use of exact ray tracing in three dimensions, which allows for both including textures and other scattering surfaces, as well as oblique incidences of sunlight.

We also showed several other facts that are important for the extension of the ray theory to three dimensions. We showed that the summation order of the rays is important and that it is dangerous, although tempting, to sum sub classes of rays to infinity, and then add the sub classes results. We showed explicitly that this will yield incorrect results.

An important result we obtained is that phases must be properly computed and included with each ray that is used to compute reflection probabilities and the absorption cross section. Without including the phases, as is sometimes done in current three-dimensional Monte-Carlo simulations of ray tracing in solar cells, we showed that an error of up to 60% and larger can be incurred.

Appendix A. Reflection and transmission amplitudes

In order derive the exact ray model, we need to include the phases. The phases are described as below:

To obtain the proper phases for reflection and transmission of a ray at the left edge of a material, we consider the potential shown in Fig. A.1.

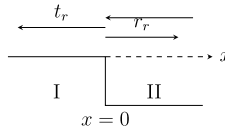


Fig. A.1. When a ray is coming from the left and goes from region I (vacuum) to region II (material with refractive index n), the ray will split into a transmitted and a reflected ray at the boundary. The amplitudes of this rays are given by the reflection and transmission amplitudes, r_l and t_l .

Coming from the left, out of region I ($x < 0$), a ray encounters the left edge of region II at $x = 0$. It gets reflected back into region I with reflection amplitude r_l , and gets transmitted into region II with amplitude t_l . The subscript l stands for “left”. In region I it is vacuum. In order to find the correct phase of the amplitude, we need to use the wavenumber of the corresponding wave and k is given by $\frac{2\pi}{\lambda}$, where λ is the wavelength. In region II, the wavenumber of the corresponding wave is given by $k_{II} = nk$ where n is the refractive index in region II. The wavefunction in region I and II are:

$$\Psi_I = e^{ikx} + r_l e^{-ikx}, \tag{A.1}$$

$$\Psi_{II} = t_l e^{ik_{II}x}. \tag{A.2}$$

Using the continuity of the wavefunction and its first derivative at $x = 0$, we obtain:

$$r_l = \frac{1 - n}{1 + n}, \tag{A.3}$$

$$t_l = \frac{2}{1 + n}. \tag{A.4}$$

When the wave is coming from the right, the ray will encounter the boundary as shown in Fig. A.2.

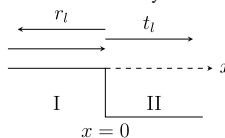


Fig. A.2. Reflection and transmission amplitudes, r_r and t_r , respectively, for a ray incident from the right (out of region II, i.e., $x > 0$).

The wavefunctions are

$$\Psi_I = t_r e^{-ikx}, \tag{A.5}$$

$$\Psi_{II} = e^{-ikn_1x} + r_r e^{ikn_1x}. \tag{A.6}$$

Again using continuity and the continuity of the first derivative gives us

$$r_r = -\left(\frac{1-n}{1+n}\right), \tag{A.7}$$

$$t_r = \frac{2n}{1+n}. \tag{A.8}$$

Appendix B. Integral formula for the spectral optical generation rate

In the scalar one-dimensional theory, the radiative flux, up to a constant, is defined by

$$j = \frac{1}{2i} \left(\psi^* \frac{d}{dx} \psi - \psi \frac{d}{dx} \psi^* \right). \tag{B.1}$$

Since, according to Fig. 1, the incident radiation is described by the plane wave $\psi_{in} = e^{ikx}$, the flux of the incident radiation is

$$j_{in} = \frac{1}{2i} \left(e^{-ikx} \frac{d}{dx} e^{ikx} - e^{ikx} \frac{d}{dx} e^{-ikx} \right) = k > 0. \tag{B.2}$$

Since, according to Fig. 1 the reflected radiation is described by $\psi_{refl} = r e^{-ikx}$, a calculation analogous to Eq. (B.2) yields

$$j_{refl} = -|r|^2 k = -Rk < 0. \tag{B.3}$$

The total flux on the left-hand side of the boundary is thus

$$j = j_{in} + j_{refl} = k - Rk. \tag{B.4}$$

In terms of flux, the reflection probability R is defined as

$$R = \left| \frac{j_{refl}}{j_{in}} \right| = |r|^2, \tag{B.5}$$

which is consistent with our earlier definition Eq. (2.1) of the reflection probability above. We now turn to the wave equation, i.e.,

$$\frac{d^2 \psi}{dx^2} = -n^2 k^2 \psi. \tag{B.6}$$

Taking the complex conjugate, we arrive at

$$\frac{d^2 \psi^*}{dx^2} = -(n^*)^2 k^2 \psi^*. \tag{B.7}$$

From Eqs. (B.6) and (B.7) we obtain

$$\psi^* \frac{d^2 \psi}{dx^2} - \psi \frac{d^2 \psi^*}{dx^2} = [(n^*)^2 - n^2] k^2 |\psi|^2. \tag{B.8}$$

We can also write the left-hand side of Eq. (B.8) as

$$\psi^* \frac{d^2 \psi}{dx^2} - \psi \frac{d^2 \psi^*}{dx^2} = \frac{d}{dx} \left[\psi^* \frac{d\psi}{dx} - \psi \frac{d\psi^*}{dx} \right] = 2i \frac{d}{dx} j(x), \tag{B.9}$$

where we used equation Eq. (B.1).

We now specialize to the situation shown in Fig. 2b, i.e., the film with mirror. For this situation, we now integrate Eq. (B.9) with Eq. (B.8) over the width of the film to obtain

$$\begin{aligned} 2i \int_0^a \frac{dj}{dx} dx &= 2i [j(a) - j(0)] \\ &= 2i [0 - k(1 - R)] \\ &= \int_0^a [(n^*)^2 - n^2] k^2 |\psi|^2 dx \\ &= \int_0^a (-4in_r n_i) k^2 |\psi|^2 dx. \end{aligned} \tag{B.10}$$

Therefore, we now obtain

$$R = 1 - 2k \int_0^a n_i n_r |\psi|^2 dx \tag{B.11}$$

and

$$\sigma = 1 - R = 2k \int_0^a n_i n_r |\psi|^2 dx. \tag{B.12}$$

Appendix C. Equivalence of the 1-R with the spectral optical generation rate

In this appendix we demonstrate that the two different approaches presented in section 2 lead to the same formula for the absorption cross section σ . For a single film on a mirror (Fig. 2a) the wavefunction ψ inside the film is

$$\psi = \frac{-2 \sin[nk(x - a)]}{\sin(nka) + i n \cos(nka)}, \tag{C.1}$$

where a is the film thickness, n is the complex refractive index and k is the wavenumber. The absorption cross section is

$$\sigma = 2k \int_0^a |\psi|^2 n_i n_r dx. \tag{C.2}$$

This can also be written as

$$\sigma = 2kn_r n_i \left(\frac{2}{\eta^2 + \theta^2} \right) \int_0^a \cosh[2n_i k(x - a)] - \cos[2n_r k(x - a)] dx, \tag{C.3}$$

where the prefactor contains

$$\begin{aligned} \eta &= \gamma - n_i \varepsilon + n_r \zeta \\ \theta &= \delta + n_i \zeta + n_r \varepsilon \\ \gamma &= \sin(n_r ka) \cosh(n_i ka) \\ \delta &= i \cos(n_r ka) \sinh(n_i ka) \\ \varepsilon &= \cos(n_r ka) \cosh(n_i ka) \\ \zeta &= i \sin(n_r ka) \sinh(n_i ka). \end{aligned} \tag{C.4}$$

Evaluation of the integral is straightforward and results in

$$\frac{2}{\eta^2 + \theta^2} [n_r \sinh(2n_i ka) - n_i \sin(2n_r ka)]. \tag{C.5}$$

To complete our task, we have to show that $1 - |r|^2$ from the scalar wave model produces the same result. The reflectivity $|r|^2$ is

$$|r|^2 = \left| \frac{-n \cos(nka) + i \sin(nka)}{n \cos(nka) - i \sin(nka)} \right|^2, \tag{C.6}$$

which can be rewritten as

$$|r|^2 = \frac{(n_r \varepsilon + n_i \zeta - \delta)^2 + (n_i \varepsilon - n_r \zeta + \gamma)^2}{\theta^2 + \eta^2}. \tag{C.7}$$

Inserting this together with γ , δ , ε , and ζ into $1 - |r|^2$ yields exactly the same result as in Eq. (C.5).

Appendix D. Proof of importance of the summation order

In this Appendix we show that for our two-film system and for a large range of dielectric constants, Eq. (5.3) holds, i.e., in these cases our ray sum in Eq. (5.1) is only conditionally convergent. We show this by observing that if the sum in Eq. (5.3) is already infinite for a subclass of rays, it is certainly infinite when summing over all rays, since all the terms not taken into account are positive. The subclass we focus on consists of rays that make p right reflections on the vacuum/film interface and make q right reflections on the film/film interface (see Fig. D.1). We also exclude any left reflections on the film/film interface, which uniquely defines our subclass of rays. Three examples of rays in our subclass are shown in Fig. D.1. All three rays have $p = 1$ and $q = 2$, and they contribute the same amplitude to r in Eq. (5.1). They differ only in their sequence of bounces. This induces degeneracy in our ray sum. In fact, any class of rays, characterized by a given p and q , is $\binom{p+q}{p}$ fold degenerate, where $\binom{p+q}{p}$ is the binomial coefficient [71]. The total contribution ρ of all of the rays of our subclass to the total reflection amplitude r is

$$\rho = \sum_{p=0}^{\infty} \sum_{q=0}^{\infty} \binom{p+q}{p} |t_1|^{2p+2} |r_1|^{2q} e^{ik[2(p+1)n_1 a_1 + 2(p+q+1)n_2 a_2]}, \tag{D.1}$$

where t_1 and r_1 are transmission amplitude and right-reflection amplitude at the vacuum/film interface, t_2 and r_2 are transmission amplitude and right-reflection amplitude at the film/film interface, a_1 is the width of film 1, a_2 is the width of film 2, and n_1 and n_2 are the refractive indices of films 1 and 2, respectively. To check whether the double sum in Eq. (D.1) is absolutely convergent, we need to check whether

$$\rho' = \sum_{p=0}^{\infty} \sum_{q=0}^{\infty} \binom{p+q}{p} |t_1|^{2p+2} |r_1|^{2q} |t_2|^{2p+2} |r_2|^{2q} \tag{D.2}$$

is finite or infinite. Defining $x = |t_2|^2 |r_1|$ and $y = |r_2|$, we may write Eq. (D.1) in the form

$$\rho' = |t_1|^2 |t_2|^2 \sum_{p=0}^{\infty} \sum_{q=0}^{\infty} \binom{p+q}{p} x^p y^q, \tag{D.3}$$

and since t_1 and t_2 are constants, it is sufficient to check the double sum

$$\rho'' = \sum_{p=0}^{\infty} \sum_{q=0}^{\infty} \binom{p+q}{p} x^p y^q > \sum_{p=0}^{\infty} \binom{2p}{p} (xy)^p > \sum_{p=1}^{\infty} \frac{(4xy)^p}{p}. \tag{D.4}$$

For the first inequality we used the fact that all terms in the sum are positive, and that, therefore, including only the diagonal terms in the sum provides a strict lower bound for the value of the sum, and for the second inequality we used the fact that $\binom{2p}{p} > 2^{2m}/m$, which is straightforward to show using the doubling formula for Euler's Γ function [71]. Analyzing the result in Eq. (D.4), we see that the sum over p converges for $xy < 1/4$. In this case, therefore, we cannot decide whether ρ^* is finite or infinite. For $xy = 1/4$, however, the last sum in Eq. (D.4) is the harmonic series, which diverges [71]. Therefore, for $xy = 1/4$, we definitely have $\rho^* = \infty$, which implies that in this case Eq. (5.1) is only conditionally convergent. Since for all $xy > 1/4$ the harmonic series provides a lower bound of the last sum in Eq. (D.4), we also have $\rho^* = \infty$ for all $xy > 1/4$. It follows that the ray sum in Eq. (5.1) is only conditionally convergent in all cases for which $z = |t_2|^2|r_1r_2| \geq 1/4$. Finally, we have to answer the question whether $z \geq 1/4$ is possible at all. We note that $|r_1|$ may freely range between 0 and 1, while $|t_2|^2|r_2|$ can range only between 0 and $2/(3\sqrt{3})$, which is obtained by observing that $|t_2|^2 = 1 - |r_2|^2$ and subsequently determining the maximum of the function $w = (1 - |r_2|^2)|r_2|$. This implies that z may range between 0 and $2/(3\sqrt{3}) > 0.38$, which overlaps with $z > 1/4$. Thus, we have proved that an entire range of cases exists in which Eq. (5.1) is only conditionally convergent. In these cases of conditional convergence we are not allowed to sum rays in arbitrary order. As discussed in Sect. 5, in order to obtain correct results, we have to sum the rays in the order of increasing path length.

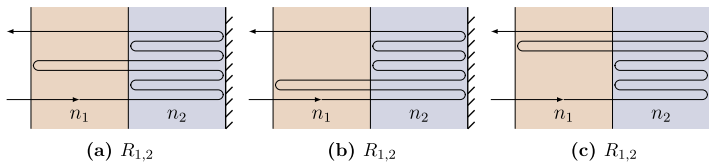


Fig. D.1. Three ray trajectories that belong to the same class, $R_{1,2}$, and contribute with the same amplitude to the reflection amplitude of the film system. They differ only in the order of right-reflections on the vacuum/film and film/film interfaces. (a) The ray reflects inside the second film, then reflects inside the first film and reflects for the second time at the film/film interface and leaves the system. (b) The ray reflects once at the vacuum/film interface then enters the second film and reflects twice on the film/film interface. (c) The ray enters the second film, reflects twice on the film/film interface, enters the first film and reflects once on the vacuum/film interface.

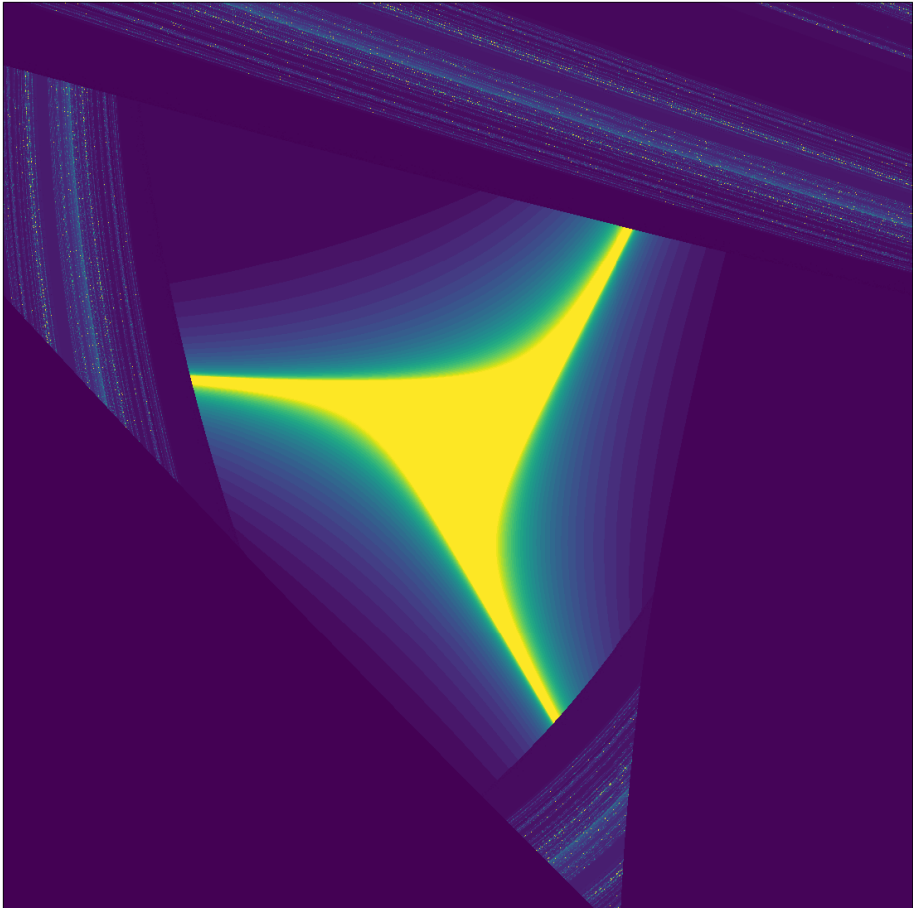
References

- [1] J. Krc, M. Zeman, S.L. Luxemburg, M. Topic, Modulated photonic-crystal structures as broadband back reflectors in thin-film solar cells, *Appl. Phys. Lett.* 94 (2009) 153501.
- [2] P. Spinelli, A. Polman, Light trapping in thin crystalline silicon solar cells using surface Mie scatterers, *IEEE J. Photovolt.* 4 (2) (2014) 554–559.
- [3] Robin Vismara, Olindo Isabella, Miro Zeman, Back-contacted BaSi₂ solar cells: an optical study, *Optic Express* 25 (8) (2017) A402.
- [4] Daniel Lockau, Tobias Sontheimer, Christiane Becker, Eveline Rudigier-Voigt, Frank Schmidt, Bernd Rech, Nanophotonic light trapping in 3-dimensional thin-film silicon architectures, *Optic Express* 21 (S1) (Jan 2013) A42–A52.
- [5] Jonathan Grandidier, Dennis M. Callahan, Jeremy N. Munday, Harry A. Atwater, Light absorption enhancement in thin-film solar cells using whispering gallery modes in dielectric nanospheres, *Adv. Mater.* 23 (10) (2011) 1272–1276.
- [6] M. Schmid, Review on light management by nanostructures in chalcopyrite solar cells, *Semicond. Sci. Technol.* 32 (4) (2017) 043003.
- [7] C. Becker, P. Wyss, D. Eisenhauer, J. Probst, V. Preidel, M. Hammerschmidt, S. Burger, 5 by 5 cm² silicon photonic crystal slabs on glass and plastic foil exhibiting broadband absorption and high-intensity near-fields, *Sci. Rep.* 4 (2014) 5886.
- [8] W.I. Nam, Y.J. Yoo, Y.M. Song, Geometrical shape design of nanophotonic surfaces for thin film solar cells, *Optic Express* 24 (14) (Jul 2016) A1033–A1044.
- [9] Eli Yablonovitch, Statistical ray optics, *J. Opt. Soc. Am.* 72 (7) (1982) 899–907.
- [10] Patrick Campbell, A. Martin, Green. Light trapping properties of pyramidally textured surfaces, *J. Appl. Phys.* 62 (1987) 243–249.
- [11] T. Uematsu, M. Iida, K. Hane, Y. Hayashi, T. Saitoh, A new light trapping structure for very-thin, high-efficiency silicon solar cells, *Photovoltaic Specialists Conference, 1988., Conference Record of the Twentieth IEEE, 1988., pp. 792–795.*
- [12] David Thorp, Stuart R. Wenham, Ray-tracing of arbitrary surface textures for light-trapping in thin silicon solar cells, *Sol. Energy Mater. Sol. Cell.* 48 (1997) 295–301.
- [13] A.W. Smith, A. Rohatgi, S.C. Neel, Texture: a ray tracing program for the photovoltaic community, *Photovoltaic Specialists Conference, 1990., Conference Record of the Twenty First IEEE, 1990., pp. 426–431.*
- [14] Rolf Brendel, Coupling of light into mechanically textured silicon solar cells: a ray tracing study, *Prog. Photovoltaics Res. Appl.* 3 (1995) 25–38.
- [15] J.E. Cotter, Raysim 6.0 - a free geometrical ray tracing program for silicon solar cells, *Photovoltaic Specialists Conference, 2005. Conference Record of the Thirty-first IEEE, 2005., pp. 1165–1168.*
- [16] Rudi Santbergen, Tomomi Meguro, Takashi Suezaki, Gensuke Koizumi, Kenji Yamamoto, Miro Zeman, Genpro4 optical model for solar cell simulation and its application to multijunction solar cells, *IEEE J. Photovolt.* 7 (2017) 919–926.
- [17] Helmut Mäkel, Hendrik Holst, Mirko Löhmann, Eckard Wefringhaus, P. Pietro, Altermatt, Detailed analysis of random pyramidal surfaces with ray tracing and image processing, *IEEE J. Photovolt.* 6 (2016) 1456–1465.
- [18] Hendrik Holst, Matthias Winter, Malte R. Vogt, Karsten Bothe, Marc Köntges, Rolf Brendel, P. Pietro, Altermatt, Applications of a new ray tracing framework to the analysis of extended regions in Si solar cell modules, *Energy Procedia* 28 (2013) 86–93.
- [19] Keith R. McIntosh, Richard M. Swanson, Jeffrey E. Cotter, A simple ray tracer to compute the optical concentration of photovoltaic modules, *Prog. Photovoltaics Res. Appl.* 14 (2006) 167–177.
- [20] Rolf Brendel, Simple prism pyramids: a new light trapping texture for silicon solar cells, *Photovoltaic Specialists Conference, 1993., Conference Record of the Twenty Third IEEE, 1993., pp. 253–255.*
- [21] Garam Yun, Karlton Crabtree, Russell A. Chipman, Properties of the polarisation ray tracing matrix, *Proc. SPIE 6682, Polarization Science and Remote Sensing III, 2007., p. 66820Z.*
- [22] Simeon C. Baker-Finch, Keith R. McIntosh, Reflection of normally incident light from silicon solar cells with pyramidal texture, *Prog. Photovoltaics Res. Appl.* 19 (2010) 406–416.
- [23] Benjamin Lipovsek, Janez Krc, Marko Topic, Optical model for thin-film photovoltaic devices with large surface textures at the front side, *Inf. MIDEM: J. Microelectron., Electron. Compon. Mater.* 41 (4) (2011) 264–271.
- [24] Janez Krc, Franc Smole, Marko Topic, Analysis of light scattering in amorphous silicon solar cells by a one-dimensional semi-coherent optical model, *Prog. Photovoltaics Res. Appl.* 11 (2003) 15–26.
- [25] C. Zechner, P. Fath, G. Willeke, E. Bucher, Two- and three-dimensional optical Carrier generation determination in crystalline silicon solar cells, *Sol. Energy Mater. Sol. Cell.* 51 (1998) 255–267.
- [26] Rolf Brendel, D. Scholten, Modeling light trapping and electronic transport of waffle-shaped crystalline thin-film silicon solar cells, *Appl. Phys. A* 69 (1999) 201–213.
- [27] Simeon C. Baker-Finch, Keith R. McIntosh, One-dimensional photogeneration profiles in silicon solar cells with pyramidal texture, *Prog. Photovoltaics Res. Appl.* 20 (2012) 51–61.
- [28] Keith R. McIntosh, Malcolm D. Abbotta, Ben A. Sudbury, Ray tracing isotextured solar cells, *Energy Procedia* 92 (2016) 122–129.
- [29] M. Zworski, *Semiclassical Analysis, Graduate Studies in Mathematics vol. 138,* (2012).
- [30] Reinhold Blümel, *Advanced Quantum Mechanics: the Classical-quantum Connection,* Jones & Bartlett Publishers, 2011.
- [31] Janez Krc, Franc Smole, Marco Topic, One-dimensional semi-coherent optical model for thin film solar cells with rough interfaces, *Inf. MIDEM: J. Microelectron., Electron. Compon. Mater.* 32 (1) (2002) 6–13.
- [32] Eugen Merzbacher, *Quantum Mechanics,* second ed. edition, Wiley, New York, 1970.
- [33] L.D. Landau, *Electrodynamics of Continuous Media, Volume 8 of Course of Theoretical Physics, second ed., Pergamon, Oxford, 1984 revised and enlarged by E.M. Lifshitz and L.P. Pitaevskii.* edition.
- [34] Jichi Ma, Jeff Chiles, Yagya D. Sharma, Sanjay Krishna, Sasan Fathpour, Two-photon photovoltaic effect in gallium arsenide, *Optic Lett.* 39 (18) (2014) 5297–5300.
- [35] Sasan Fathpour, Kevin K. Tsia, Bahram Jalali, Two-photon photovoltaic effect in silicon, *IEEE J. Quant. Electron.* 43 (12) (2007) 1211–1217.
- [36] V.E. Ferry, J.N. Munday, H.A. Atwater, Design considerations for plasmonic photovoltaics, *Adv. Mater.* 22 (43) (2010) 4794–4808.
- [37] Richard Phillips Feynman, *QED: The Strange Theory of Light and Matter,* Princeton University Press, 2006.
- [38] J.S. Townsend, *Quantum Physics: a Fundamental Approach to Modern Physics,* University Science Books, 2010.
- [39] David J. Griffiths, *Introduction to Electrodynamics,* third ed. edition, Prentice Hall,

- Upper Saddle River, N.J, 1999.
- [40] R. Blümel, T.M. Antonsen, B. Geogort, E. Ott, R.E. Prange, Ray splitting and quantum chaos, *Phys. Rev. E* 53 (Apr 1996) 3284–3302.
- [41] A. Kohler, R. Blümel, Weyl formulas for quantum ray-splitting billiards, *Ann. Phys.* 267 (1998) 249–280.
- [42] R. Blümel, P.M. Koch, L. Sirko, Ray-splitting billiards, *Found. Phys.* 31 (2001) 269–281.
- [43] Martin C. Gutzwiller, *Chaos in Classical and Quantum Mechanics*, first ed. edition, Springer, 1990.
- [44] L. Sirko, P.M. Koch, R. Blümel, Experimental identification of non-Newtonian orbits produced by ray splitting in a dielectric-loaded microwave cavity, *Phys. Rev. Lett.* 78 (Apr 1997) 2940–2943.
- [45] Y. Hlushchuk, A. Kohler, Sz Bauch, L. Sirko, R. Blümel, M. Barth, H.-J. Stockmann, Autocorrelation function of level velocities for ray-splitting billiards, *Phys. Rev. E* 61 (1) (2000) 366.
- [46] N. Savvitskiy, A. Kohler, Sz Bauch, R. Blümel, L. Sirko, Parametric correlations of the energy levels of ray-splitting billiards, *Phys. Rev. E* 64 (3) (2001) 036211.
- [47] A. Kohler, R. Blümel, Annular ray-splitting billiard, *Phys. Lett. A* 238 (4–5) (1998) 271–277.
- [48] A. Kohler, R. Blümel, Weyl formulas for quantum ray-splitting billiards, *Ann. Phys.* 267 (2) (1998) 249–280.
- [49] A. Kohler, R. Blümel, Test of semiclassical amplitudes for quantum ray-splitting systems, *Phys. Rev. E* 59 (6) (1999) 7228.
- [50] B. Riemann, Über die Darstellbarkeit einer Function durch eine trigonometrische Reihe, Dieterich, 1867.
- [51] Stewart Galanor, Riemann's rearrangement Theorem, *Math. Teach.* 80 (8) (1987) 675–681.
- [52] Seok-Joo Byun, Seok Yong Byun, Jangkyo Lee, Jae Wan Kim, Taek Sung Lee, Won Mok Kim, Young Kyu Park, Kyuman Cho, An optical simulation algorithm based on ray tracing technique for light absorption in thin film solar cells, *Sol. Energy Mater. Sol. Cell.* 95 (1) (2011) 408–411.
- [53] H.S. Carslaw, A historical note on Gibbs' phenomenon in Fourier's series and integrals, *Bull. Am. Math. Soc.* 31 (8) (10 1925) 420–424.
- [54] A. Nuttall, Some windows with very good sidelobe behavior, *IEEE Trans. Acoust. Speech Signal Process.* 29 (1) (Feb 1981) 84–91.
- [55] Josefine K. Selj, David Young, Sachit Grover, Optimization of the antireflection coating of thin epitaxial crystalline silicon solar cells, *Energy Procedia* 77 (2015) 248–252 5th International Conference on Silicon Photovoltaics, SiliconPV 2015.
- [56] A. Martin, Green. Self-consistent optical parameters of intrinsic silicon at 300K including temperature coefficients, *Sol. Energy Mater. Sol. Cell.* 92 (11) (2008) 1305–1310.
- [57] D.T. Pierce, W.E. Spicer, Electronic structure of amorphous Si from photoemission and optical studies, *Phys. Rev. B* 5 (Apr 1972) 3017–3029.
- [58] Tobias A.F. König, Petr A. Ledin, Justin Kerszulis, Mahmoud. A. Mahmoud, Mostafa A. El-Sayed, John R. Reynolds, Vladimir V. Tsukruk, Electrically tunable plasmonic behavior of nanocube-polymer nanomaterials induced by a redox-active electrochromic polymer, *ACS Nano* 8 (6) (2014) 6182–6192 PMID: 24870253.
- [59] Reference solar spectral irradiance: Air mass 1.5. <http://rredc.nrel.gov/solar/spectra/am1.5>. (Accessed 19 April 2018).
- [60] Max Born, E. Wolf, *Principles of Optics: Electromagnetic Theory of Propagation, Interference and Diffraction of Light*, fourth ed. edition, Pergamon Press, Oxford, 1970.
- [61] John David Jackson, *Classical Electrodynamics*, second ed. edition, John Wiley & Sons, New York, 1970.
- [62] Richard P. Feynman, *Quantum Mechanics and Path Integrals*, International Series in Pure and Applied Physics, McGraw-Hill, New York, 1965.
- [63] R. Blümel, Yu. Dabaghian, R.V. Jensen, Explicitly solvable cases of one-dimensional quantum chaos, *Phys. Rev. Lett.* 88 (4) (January 2002).
- [64] Yu. Dabaghian, R. Blümel, Explicit analytical solution for scaling quantum graphs, *Phys. Rev. E* 68 (Nov 2003) 055201.
- [65] Yu. Dabaghian, R. Blümel, Explicit spectral formulas for scaling quantum graphs, *Phys. Rev. E* 70 (Oct 2004) 046206.
- [66] Jiabao Zheng, Robert A. Barton, Dirk Englund, Broadband coherent absorption in chirped-planar-dielectric cavities for 2d-material-based photovoltaics and photodetectors, *ACS Photonics* 1 (9) (2014) 768–774.
- [67] Jessica R. Piper, Shanhuai Fan, Broadband absorption enhancement in solar cells with an atomically thin active layer, *ACS Photonics* 3 (4) (2016) 571–577.
- [68] Yilei Li, Alexey Chernikov, Xian Zhang, Rigosi Albert, Heather M. Hill, Arend M. van der Zande, Daniel A. Chenet, En-Min Shih, James Hone, Tony F. Heinz, Measurement of the optical dielectric function of monolayer transition-metal dichalcogenides: Mos 2, mo s e 2, ws 2, and ws e 2, *Phys. Rev. B* 90 (20) (2014) 205422.
- [69] Dario Cozza, Carmen M. Ruiz, David Duche, Sergio Giraldo, Edgardo Saucedo, Jean Jaques Simon, Ludovic Escoubas, Optical modeling and optimization of Cu₂ZnSnSe₄ solar cells using the modified transfer matrix method, *Optic Express* 24 (18) (2016) A1201–A1209.
- [70] R. Blümel, Comment on 'quantum chaos in elementary quantum mechanics' by Yu. Dabaghian and R. Jensen, *Eur. J. Phys.* 27 (1) (2006) L1.
- [71] I.S. Gradshteyn, I.M. Ryzhik, *Table of Integrals, Series and Products*, fifth ed., Academic Press, 1994.

Appendix B

Paper II



Chaos: A new mechanism for enhancing the optical generation rate in optically thin solar cells

Cite as: Chaos 29, 093132 (2019); <https://doi.org/10.1063/1.5111042>

Submitted: 22 May 2019 . Accepted: 06 September 2019 . Published Online: 30 September 2019

E. Seim , A. Kohler , R. Lukacs , M. A. Brandsrud , E. S. Marstein , E. Olsen , and R. Blümel 



View Online



Export Citation



CrossMark



Scilight Highlights of the best new research
in the physical sciences

LEARN MORE!



Chaos: A new mechanism for enhancing the optical generation rate in optically thin solar cells

Cite as: Chaos 29, 093132 (2019); doi: 10.1063/1.5111042

Submitted: 22 May 2019 · Accepted: 6 September 2019 ·

Published Online: 30 September 2019



View Online



Export Citation



CrossMark

E. Seim,^{1,a)} A. Kohler,¹ R. Lukacs,¹ M. A. Brandsrud,¹ E. S. Marstein,^{2,3} E. Olsen,¹ and R. Blümel⁴

AFFILIATIONS

¹RealTek, Norwegian University of Life Sciences, Ås 1430, Norway

²Department of Solar Energy, Institute of Energy Technology, Kjeller 2007, Norway

³Department of Technology Systems, University of Oslo, Oslo 0371, Norway

⁴Department of Physics, Wesleyan University, Middletown, CT 06457, USA

^{a)}e.seim.es@gmail.com

ABSTRACT

The photogenerated current of solar cells can be enhanced by light management with surface structures. For solar cells with optically thin absorbing layers, it is especially important to take advantage of this fact through light trapping. The general idea behind light trapping is to use structures, either on the front surface or on the back, to scatter light rays to maximize their path length in the absorber. In this paper, we investigate the potential of chaotic scattering for light trapping. It is well known that the trajectories close to the invariant set of a chaotic scatterer spend a very long time inside of the scatterer before they leave. The invariant set, also called the chaotic repeller, contains all rays of infinite length that never enter or leave the region of the scatterer. If chaotic repellers exist in a system, a chaotic dynamics is present in the scatterer. As a model system, we investigate an elliptical dome structure placed on top of an optically thin absorbing film, a system inspired by the chaotic Bunimovich stadium. A classical ray-tracing program has been developed to classify the scattering dynamics and to evaluate the absorption efficiency, modeled with Beer-Lambert's law. We find that there is a strong correlation between the enhancement of absorption efficiency and the onset of chaotic scattering in such systems. The dynamics of the systems was shown to be chaotic by their positive Lyapunov exponents and the noninteger fractal dimension of their scattering fractals.

© 2019 Author(s). All article content, except where otherwise noted, is licensed under a Creative Commons Attribution (CC BY) license (<http://creativecommons.org/licenses/by/4.0/>). <https://doi.org/10.1063/1.5111042>

Chaotic scattering of light rays is a feature of many types of surface-structured solar cells. Scattering structures that lead to chaotic scattering have an invariant set of infinitely long-lived trajectories. In this paper, we illustrate how concepts and methods from the field of chaos can provide valuable insights for further developments in a vastly different field: light management in optically thin solar cells.

I. INTRODUCTION

Photovoltaic solar cells (PV) are an increasingly important source of renewable energy. In order to increase the competitiveness of solar electricity, it is desirable to reduce the material costs of solar cells and modules further. Thin solar cells are less prone to bulk recombination and can exhibit larger voltages than their

thicker counterparts. In addition, they require less absorber materials, which can reduce cost and environmental footprint further. Reducing the thickness of solar cells requires low surface recombination, as well as an efficient light-trapping scheme to avoid excessive transmission and/or reflection losses. Silicon-based solar cells represent by far the most widespread solar cell technology today. However, silicon exhibits an indirect electronic band gap, which results in weak absorption. This makes the development of surface structures with efficient light-trapping properties even more important for thin silicon solar cells. Additionally, commercial silicon-based PV production has become so refined that the theoretical maximal efficiency of 29.8%¹ might soon be a limiting factor. This further motivates to look to more efficient alternatives like thin film PV.

A number of different mechanisms for absorption efficiency enhancement are discussed in the scientific literature and some

of them are already implemented in solar cell technology. These efforts range from plasmonics² to surface-structured light-trapping designs with either ordered structures or random surfaces.^{3–9} In light-trapping designs, the aim is to establish surface structures that keep as many of the incoming light rays as long as possible in the absorber. This maximizes the chance of absorption before the rays can leave the solar cell. The maximal enhancement factor for intensity with respect to the incident intensity is $4n^2$, where n is the index of refraction of the solar cell, a limit shown by Yablonoitch in 1982, commonly called the Yablonoitch limit.¹⁰ To show this, Yablonoitch theorized that a truly random surface texture applied to both sides of a film would randomize the direction of the rays interacting with the surface, thus effectively trapping the light rays by maximizing the chance of total internal reflection to occur.

Ray trapping is a phenomenon that has been extensively investigated in the context of chaotic scattering systems. Chaotic scattering systems have been studied for quantum wave systems and the corresponding classical ray systems, and several textbooks have been published in this field.^{11–13} Chaos is a mature field of research with a rich set of tools to study dynamics both classically, using rays, and quantum mechanically, using waves. Chaotic systems were originally studied by Henri Poincaré, who investigated the three-body problem in the 1890s.¹⁴ In the 1960s, Lorenz modeled the atmosphere for weather prediction using three coupled nonlinear ordinary differential equations.¹⁵ The famous butterfly effect originates from this work. Both Poincaré and Lorenz found systems that exhibit extreme sensitivity to the initial conditions. The study of dynamical billiards started in 1898 when Hadamard showed that all trajectories in a Hadamard billiard diverge exponentially, thus proving for the first time the existence of what nowadays is called “deterministic chaos” in a dynamical system.¹⁶ Later, in the 1970s and 1980s, Bunimovich also studied dynamical billiards and proved that the dynamics of the “Bunimovich stadium,” a special dynamical billiard [Fig. 1(a)],^{17–19} is chaotic. The class of dynamical billiards that is important for this work are those where we consider a frictionless particle (a model photon) moving on a flat surface in the presence of some additional structures that reflect, transmit, and refract the particle, akin to the dynamics in a dielectric cavity,^{20,21} such as the dielectric-loaded Bunimovich stadium.²² Chaotic scattering systems were for the first time studied in the late 1980s. By the early 1990s, many different chaotic scattering systems had been studied:²³ three-disk scattering,²⁴ celestial mechanics,^{25,26} charged-particle trajectories in electric and magnetic fields,²⁷ and scattering in atomic and nuclear physics.^{28–30} To name only a few. A review of new developments was written by Seoane and Sanjuán.³¹

In this study, we investigate if chaotic scattering can be considered as a mechanism for absorption enhancement and eventually used as a guide for designing efficient solar cell surfaces for thin solar cells. As a model system, we use a dome structure consisting of half an ellipse and a rectangular slab mimicking the solar cell absorber. The shape chosen is similar to the dielectric-loaded Bunimovich stadium,²³ which is a stadium that is cut in half along the middle of the long side. We call our model system film + dome. The film + dome system has mirrors at the bottom and on the sides. The model system we have chosen is thus a model for dome-shaped surface-structured solar cells. This is a two-dimensional model, but we imagine a third dimension, orthogonal to the two-dimensional

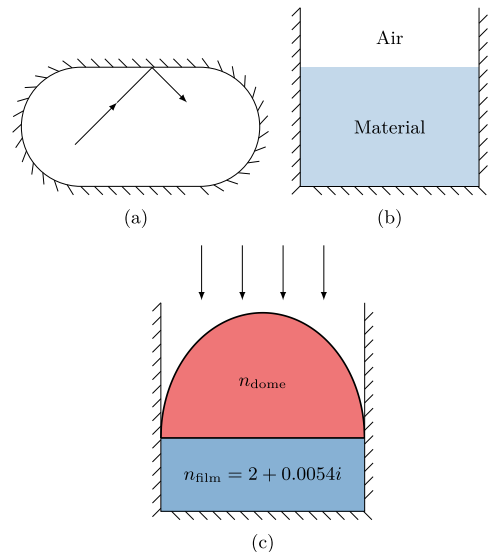


FIG. 1. (a) The Bunimovich stadium is a dynamical billiard extensively studied in the context of chaos. (b) The open system is comprised of three mirrors arranged in a bucketlike shape. The energy converting material in a solar cell can be modeled by a complex refractive index. (c) A $3.46 \mu\text{m}$ tall dome on top of a $2 \mu\text{m}$ thick film. The width of the film and dome is $5 \mu\text{m}$. The arrows show how incident rays are sent toward the surface.

plane of our model, in which our two-dimensional model is continuous with cylindrical symmetry. Thus, our two-dimensional model reflects the dynamics of the three-dimensional cylindrically symmetric system on a cut orthogonal to its cylinder axis. There are two ray-splitting surfaces present; the elliptical air-dome interface and the flat dome-film interface.

Outside of the film + dome, the refractive index is equal to one. Ray-splitting systems have been extensively studied in the field of quantum chaos.^{32–38} In ray-splitting systems, rays impinging on the surface of the film + dome are transmitted and reflected according to probabilities, which in electrodynamics are calculated by the Fresnel equations.

Since the mechanisms of chaos have to our knowledge so far attracted very little attention in the context of absorption enhancement,³⁹ we start this paper with a brief account of classical chaos, highlighting aspects of chaos of relevance for the understanding of this paper. We then introduce our classical ray-tracing model for studying dynamical scattering systems. We demonstrate and discuss the relevance of chaos in the context of absorption enhancement due to surface structuring of solar cells. Finally, we compare our classical ray-tracing simulations with finite difference time domain (FDTD) electromagnetic (E&M) wave calculations.

II. CLASSICAL CHAOS

Chaotic dynamical systems are extremely sensitive to initial conditions. In practice, this means that although chaotic systems are governed by purely deterministic laws, they do not have closed-form solutions. Lorenz puts it this way: "Chaos: When the present determines the future, but the approximate present does not approximately determine the future," which expresses the fact that while the classical dynamics of deterministic chaos is in principle predictable, small deviations lead to a completely different dynamics. The sensitivity to initial conditions can be quantified by the Lyapunov exponent. Consider two rays started from almost the same initial conditions in phase space. If the rays are started from and evolve in a chaotic region in phase space, they will, after some point in time, evolve on dramatically different trajectories. Before this happens, the two rays will diverge exponentially fast away from each other. The Lyapunov exponent is a measure of the rate of this divergence. It is given as

$$s(t) = e^{\lambda t} s(0), \quad (1)$$

where λ is the Lyapunov exponent, $s(0)$ is the initial separation distance in phase space, and $s(t)$ is the separation at a time t . A positive Lyapunov exponent means that the divergence is exponentially fast. Thus, a positive Lyapunov exponent is a signature of classical chaos. The separation at $t \neq 0$ can be measured in a Poincaré surface of section (PSOS), which is a section of the total phase space. A PSOS may be used as a way to visualize a trajectory via an intersection surface in physical space.

In dynamical billiards and scattering systems, rays can follow periodic trajectories, also called periodic orbits. However, in scattering systems, periodic orbits can never escape the system; otherwise, they would not be periodic. These rays make up a part of the invariant set of infinitely long-lived trajectories; the other part is made up of nonescaping, nonperiodic trajectories.^{40,41} The geometry of the invariant set can be visualized in phase space. If the invariant set has a fractal geometric structure in phase space, it is a sign of sensitivity with respect to initial conditions, thus a sign of chaos. Fractal invariant sets in scattering systems are also called chaotic repellers. It is known that when a trajectory is started near a chaotic repeller, it takes a very long time to move away from the chaotic repeller when the phase space is a mix of chaotic and regular regions.⁴²

The notion of fractals and fractal dimensions was first discussed by Mandelbrot in 1967, although the actual terms were introduced later, in 1975.⁴³ The fractal dimension of the invariant set can be found using a standard method called box counting,^{44,45} which we will also use in our paper to estimate the fractal dimension of the phase space. The procedure is to cover the phase space with boxes and count how many boxes contain parts of the invariant set at different scales. We define the fractal dimension d as

$$d = \lim_{M \rightarrow \infty} \frac{\log N}{\log M}, \quad (2)$$

where N is the number of boxes that contain a part of the invariant set at a scale M . In a numerical approximation of d , however, M is finite.

III. A MODEL FOR STUDYING CHAOS

A solar cell is a scattering system. Electromagnetic radiation enters the system and may be completely or partially absorbed. We may describe the electromagnetic radiation and its interaction with a solar cell by a ray model in the following way. Light rays enter the solar cell through the front surface. Light that is not absorbed may be reflected from the metallic back contacts and eventually leave the solar cell. The absorption of electromagnetic radiation by the solar cell can be taken into account by associating the rays with amplitudes that are decreasing according to the attenuation described by the Beer-Lambert law. In this paper, we simulate a solar cell by introducing a model system with a defined geometry and enclosing it in a "bucket" of perfect mirrors, see Fig. 1(b). With this constraint, the rays can only leave through the front side. Although real mirrors have some degree of absorption and transmission, we neglect these effects in our simulations and, for the sake of simplicity, treat all mirrors in our simulations as perfect mirrors. In our open bucket, we study chaotic and regular ray dynamics with the help of classical ray tracing and use our simulations to compare systems exhibiting chaotic phase-space structures with systems exhibiting more regular phase-space structures.

It is known that circular, rectangular, and triangular billiards are regular systems with no chaotic dynamics. However, introducing a stepped potential inside such billiards produces chaos.^{46,47} This is analogous to placing a material with an index of refraction larger than 1 in our mirror bucket. Our model system, which we place in the bucket, is a structure comprised of a flat film with a dome placed on top as seen in Fig. 1(c). The dome structure is half an ellipse and the film is a rectangular slab. The shape is similar to a Bunimovich stadium cut in half along the middle of the long side, which, similar to our ellipses, has semicircles attached to its rectangular middle section. We name our model system film + dome. We explore film + dome systems, where we keep the refractive index in the film at a constant value of $n_{\text{film}} = 2 + 0.0054i$ and vary the refractive index in the dome n_{dome} to look for a transition from regular to chaotic scattering dynamics. The imaginary part of n_{film} is chosen to be the same value as for silicon at 800 nm,⁴⁸ truncated to four decimals. Silicon is not a very good light absorber at this wavelength. Thus, the value is a good choice when looking to improve absorption properties.

A. Classical ray tracing

In principle, if properly equipped with phases, Maxwell's equations may be solved exactly using classical rays. We illustrated this wave-ray equivalence recently by solving the wave equation of a one-dimensional, dissipative, and layered solar cell exactly with the help of classical rays that were properly equipped with phases.⁴⁹ An equivalently exact ray-tracing theory for two-dimensional dissipative systems has not yet been described. However, in the geometric-optic limit, where the wavelength is small compared to the scattering structures, it is common practice in the literature to consider optical rays. Following this practice, we will use a classical ray-tracing approach, neglecting proper inclusion of phases. Since we know that the inclusion of phases is essential to obtain a one-to-one correspondence with Maxwell's equations, we accept that our results are approximations. However, quantities computed as averages over ensembles of rays

may still be quite accurate, since statistical averaging tends to cancel out phases.

We wrote a numerical ray-tracing code to study classical chaos where Snell's law is the physical principle used to determine the evolution of a ray, i.e.,

$$n_1 \sin(\theta_1) = n_2 \sin(\theta_2). \tag{3}$$

Here, n_1 and n_2 are the real parts of the index of the refraction of either side of an interface and θ_1 and θ_2 are the incident and refracted angles, respectively. Each ray is given an initial "intensity," $I_0 = 1$. There are three mechanisms that affect the intensity: reflection at and transmission through a boundary between two materials and absorption along the path of the ray, which we will model with the Beer-Lambert law. To calculate the intensity I , when a ray crosses an interface between different materials, we need reflection and transmission coefficients. The transverse electric (TE) Fresnel equations correspond to the case where the polarization of the electric field is perpendicular to the plane of incidence. For the one-dimensional case, there are no separate Fresnel equations for TE and transverse magnetic (TM). This is because the incoming ray vector coincides with the interface normal, and thus there is no plane of incidence. For the exact one-dimensional case,⁴⁹ there are no separate Fresnel equations for TE and TM. This is because the incoming ray vector coincides with the interface normal, and thus there is no plane of incidence. The reflection and transmission amplitudes of the transverse electric (TE) case are given by

$$r_{TE} = \frac{\cos \theta_1 - \sqrt{n'^2 - \sin^2 \theta_1}}{\cos \theta_1 + \sqrt{n'^2 + \sin^2 \theta_1}}, \tag{4}$$

$$t_{TE} = \frac{2 \cos \theta_1}{\cos \theta_1 + \sqrt{n'^2 - \sin^2 \theta_1}}, \tag{5}$$

where $n' = n_2/n_1$. The choice of using the TE Fresnel equations ensures that a scalar wave equation is exact when evaluating electromagnetic systems in two dimensions, or equivalently, three-dimensional systems with cylinder symmetry. The polarization of light does not change when it moves across an interface if the polarization is perpendicular to the plane of incidence. For later comparisons, our ray model was equipped with these specific Fresnel equations. These equations govern how much of the intensity is reflected and how much is transmitted. The corresponding reflection and transmission coefficients are

$$\mathcal{R} = |r_{TE}|^2, \tag{6}$$

$$\mathcal{T} = \frac{\sqrt{n'^2 - \sin^2 \theta_1}}{\cos \theta_1} |t_{TE}|^2. \tag{7}$$

We consider materials with a small absorption coefficient n_i and, therefore, neglect the fact that absorption turns homogeneous into inhomogeneous plane waves in absorptive media.^{50,51} Whenever Snell's law is referred to, it is the familiar law stated in Eq. (3).

Whenever a ray crosses an interface between two materials, it splits into a reflected ray and a transmitted ray. The practical implication of this is that calculations must be truncated because of run time. As long as we have splitting rays, there will be branches of the original ray that are inside the scatterer forever. We implemented a

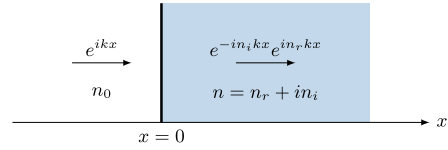


FIG. 2. A plane wave enters an absorbing material with a complex index of refraction $n = n_r + in_i$. The intensity of the wave decays exponentially with a factor of $e^{-4\pi n_i x/\lambda}$.

truncation condition that stops the simulation of a particular branch when $I_b < 10^{-5}$, where I_b is the intensity in that branch. The effect of the truncation threshold was thoroughly investigated by calculating the average intensity lost due to terminating the rays early, i.e., the truncation loss. For $n_{\text{dome}} \leq 2$, this value never exceeded 0.037% of the total average intensity. When $n_{\text{dome}} > 2$, the truncation loss was higher, but it never exceeded 0.74% of the total average intensity.

Whenever a ray splits, the intensity in the resulting two branches is determined according to the Fresnel coefficients stated in Eqs. (4) and (5). The subsequent absorption in the material is governed by the Beer-Lambert law explained in Sec. III B.

B. Beer-Lambert law of absorption

We use the Beer-Lambert law of absorption to provide an approximate measure of the absorption efficiency of our model, which we call the Beer-Lambert efficiency. It is an approximation because the classical ray model does not take diffraction into account as an electromagnetic simulation would do. The extinction coefficient in the Beer-Lambert law determines how fast the intensity of incoming radiation is decaying. Consider a plane wave e^{ikx} , incident on a slab of absorbing materials (see Fig. 2). Inside the material, the index of refraction, $n = n_r + in_i$, is complex, and the wave is

$$e^{ikx} = e^{i(n_r + in_i)kx} = e^{-n_i kx} e^{in_r kx}, \tag{8}$$

where $k = 2\pi/\lambda$ denotes the wave vector and x is the penetration-depth into the material. To obtain the intensity of the wave, we must take the absolute square value

$$|e^{-n_i kx} e^{in_r kx}|^2 = e^{-4\pi n_i x/\lambda}. \tag{9}$$

We now see that the intensity is decaying exponentially as a function of the path length inside of the absorbing material and the imaginary part of the refractive index of the material. In order to use our classical ray tracing approach, a transition from waves to rays is needed. We have chosen to assign each incoming ray an initial intensity of 1, which is reduced as a function of the path length only, since n_i is kept constant in the absorbing material.

IV. THE TRANSITION FROM REGULAR TO CHAOTIC DYNAMICS ENHANCES ABSORPTION EFFICIENCY

In this section, we discuss how the film + dome system transitions from regular to chaotic scattering dynamics and establish our central result, the correlation between the onset of chaos and the

rapid increase in the Beer-Lambert efficiency that systematically follows. We present results that show the transition from regular to chaotic dynamics in three different ways as a function of n_{dome} :

1. computation of the fractal dimension of the invariant set of infinitely long-lived trajectories;
2. the chaotic nature of Newtonian rays entering the system from the outside;
3. calculation of the absorption cross section, averaged over the wavelength in an electromagnetic simulation using a commercial finite-difference time-domain (FDTD) solver.⁵²

To corroborate and confirm that the correlation between the onset of chaos and the enhancement of the Beer-Lambert efficiency is not specific to a certain special film thickness but a structurally stable phenomenon, we repeated the three routes we use to show the transition to chaos five times for varying film thicknesses. The only exceptions to this procedure are the electromagnetic simulations, which were studied only in the case of the $2\ \mu\text{m}$ film. We start by showing the onset of chaos and its signatures for the system in Fig. 1(c), which has a $3.46\ \mu\text{m}$ tall elliptical dome on top of a $2\ \mu\text{m}$ thick film as an example, and end the section by showing the structural stability of the connection between the onset of chaos and the onset of absorption enhancement.

A. Scattering fractals and periodic orbits

A signature of chaos is the existence of chaotic repellers.⁵³ We, therefore, look for chaotic repellers in the invariant set of infinitely long-lived trajectories. We choose the bottom mirror of the bucket-shaped system as our PSOS and send nonabsorbing Newtonian rays from 10 080 equispaced positions in the spatial interval $x \in (0, 5)$, spanning the full width of the system, and from 10 080 equispaced angles in the interval $\theta \in (-\pi, \pi)$. The lifetime of these Newtonian rays is characterized by the number of collisions they make with the PSOS. This characterization ensures that a trapped ray may not simply live a long time in the scatterer, but has to return to the back mirror, thus spending a portion of its lifetime in the absorbing film, in order to be trapped. Rays with the initial angle π or $-\pi$ are omitted since they would bounce back and forth between the right and left mirrors forever. Figure 3 shows a visualization of the initial conditions of the rays, color-coded according to their lifetimes, ranging from deep blue for short lifetimes to yellow for long lifetimes, for four different indices of refraction of the dome. Since many subsets of these visualizations have fractal dimensions, we refer to these visualizations as scattering fractals. The horizontal axis of the scattering fractals corresponds to x , while the vertical axis corresponds to θ .

The lifetime of each ray is measured by the number of bounces it makes with the PSOS, in this case the rear mirror. The fractal dimension of each scattering fractal for n_{dome} between 1 and 2.5 in steps of 0.1 is found by the box counting method, see Fig. 7. In general, the transition to chaos may or may not be abrupt. In the case where it is not abrupt but gradual, more and more of the phase space will be chaotic during the transition. The film + dome system has a gradual transition to chaos. We have opted to define the onset of chaos in terms of n_{dome} as the cases where the calculated

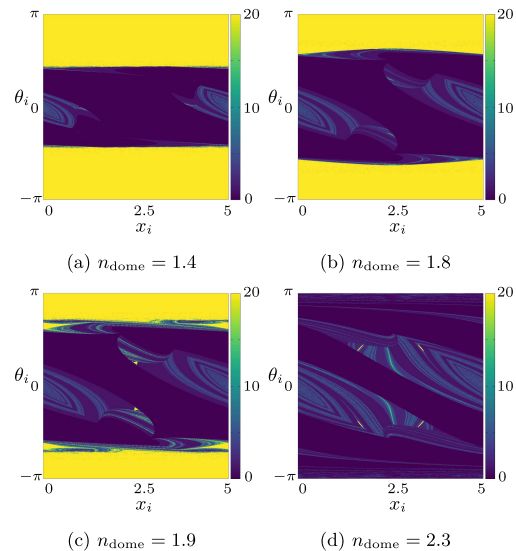


FIG. 3. Scattering fractals for four different film + dome systems for four different values of n_{dome} , respectively. In the case of (a), where $n_{\text{dome}} = 1.4$, the fractal dimension is ≈ 2 . Hence, it is essentially a regular system. In (b) ($n_{\text{dome}} = 1.8$), (c) ($n_{\text{dome}} = 1.9$), and (d) ($n_{\text{dome}} = 2.3$), the fractal dimensions are less than the threshold value of 1.95. The scattering fractals show the lifetime in terms of the number of collisions with the PSOS. The initial angles, θ_i , and the initial positions, x_i , of the rays, cover the PSOS.

fractal dimension dropped below 1.95. In general, the scattering fractals will not behave as self-similar monofractals with simple scaling rules. The box-counting method was, therefore, used carefully and only on scattering fractals which did not exhibit multiple scaling rules. When computing scattering fractals for chaotic systems, one must also respect that the extreme sensitivity of chaos means that calculation precision can degrade quickly. The rays used for calculating fractal dimensions are cut off at 20 bounces on the PSOS to prevent this problem. This limit is the only truncation of the lifetime of the rays since absorption was turned off for the calculation of the scattering fractals. The example of the $2\ \mu\text{m}$ thick film shows a fractal dimension below 1.95 when $n_{\text{dome}} \approx 1.5$, as indicated by the horizontal dashed line in Fig. 7(c).

When n_{dome} is exactly 1, it is equivalent to no dome at all, only the flat film, which must have fully regular dynamics. As expected, the fractal dimension is integer, $d = 2$. This is because rays started from the inside at shallow angles will be trapped forever due to the total internal reflection. There is a sharp transition from being trapped forever and escaping immediately in this case. When n_{dome} is increased, the geometry of the scattering fractal changes [Fig. 3(a)]. No longer is there a sharp transition between the trapped and the escaping rays. The border exhibits a fractal geometry and the lifetime of rays is

sensitive to the initial coordinate and angle. Further increase in n_{dome} yields an even more complex border where the lifetime of the rays is very sensitive to their initial conditions [Figs. 3(b) and 3(c)]. These complex borders are fractal, meaning that rays which enter the region near them might stay for a very long time in the system.⁴²

When n_{dome} is increased beyond the index of refraction of the film, the invariant set gets drastically smaller [Fig. 3(d)]. The total internal reflection is now a possibility at the dome-film interface and thus rays are ejected from the chaotic repeller much earlier. Moreover, triangularlike regions of trapped rays start to appear in the scattering fractals for values of n_{dome} around 2 near the center of the scattering fractal. This can be seen as the small yellow regions in Figs. 3(c), 3(d), and 4(a), which shows an enlargement of the upper small yellow region in Fig. 3(c). To more clearly bring out the ray dynamics in the vicinity of the regular island shown in Fig. 4(a), Fig. 4(b) shows the phase-space portrait of rays that were sent out from the initial conditions of Fig. 4(a) and, to accurately represent the relatively long trajectories that linger in the vicinity of the regular island, the cut-off is now at 200 bounces instead of 20. The phase-space portrait in Fig. 4(b) shows a stable island surrounded by hyperbolas that close in on the three corners of the stable island. The orbit corresponding to the center of the stable island is shown in Fig. 4(c). This orbit is totally reflected at the air-dome interface. In the case of the total internal reflection, the full intensity of the ray is reflected, which is very beneficial from a light-trapping perspective. The fact that we are not looking to calculate the fractal dimension, but periodic orbits at this point, justifies the cut-off limit of 200 bounces on the bottom mirror. A ray launched from the initial condition pinched by the hyperbolas produces an orbit with period three, as seen in Figs. 4(d) and 4(e).

B. Newtonian rays sent in from the outside

The onset of chaos can also be inferred from Newtonian rays sent in from the outside. When we model surface-structured solar cells with rays, we send the rays in straight down from the outside. Such rays behave very predictably for values of n_{dome} up to 1.65 as seen in Figs. 5(a) and 5(b). There is no sign of sensitivity with respect to the initial position above the film + dome system. In Figs. 5(c) and 5(d), we let $n_{\text{dome}} = 1.70$ and $n_{\text{dome}} = 1.75$, respectively, and we see that some of the rays start to take wildly different paths compared to their neighboring rays. This indicates the onset of chaos.

It is important to note that Fig. 5 shows Newtonian rays. Figure 5(a) does not show the trajectories of non-Newtonian rays, which are used for calculating the Beer-Lambert efficiency. The rays shown in Fig. 5(a) are Newtonian rays sent in from the outside. Despite the simplicity of this visualization, it captures the emergence of sensitivity to the initial positions of the rays.

Chaos in dynamical ray systems is often defined by a positive Lyapunov exponent. We calculated the Lyapunov exponent of Newtonian rays sent normally toward the dome-film interface from the outside. Figure 6 shows the Lyapunov exponents as a function of the initial starting positions, x_i , of the rays above the film + dome ($2\ \mu\text{m}$ thick film) system. Like in Fig. 5, we see a change when increasing n_{dome} beyond 1.65. At $n_{\text{dome}} = 1.7$, some of the rays exhibit a positive Lyapunov exponent. The number of rays with a positive

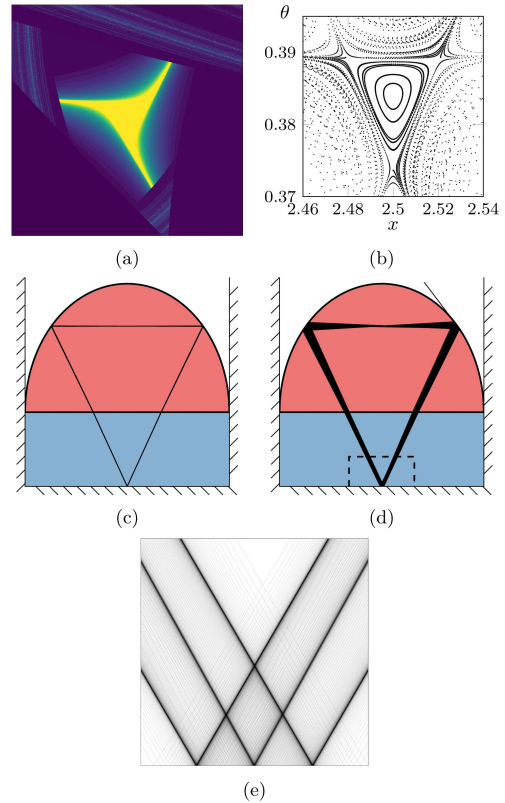


FIG. 4. (a) A chaotic repeller in the scattering fractal of the film + dome system for $n_{\text{dome}} = 1.9$. (b) The phase-space portrait generated by rays started for initial conditions in (a). (c) An orbit started near a fixed point. (d) An orbit started near a period three orbit. (e) A crop of the dashed area in (d) showing that the orbit is indeed a period three orbit.

Lyapunov exponent increases with n_{dome} . This result is consistent with the behavior of the scattering fractals and the results shown in Fig. 5.

C. Beer-Lambert efficiency

We simulate incoming sunlight by sending 5000 non-Newtonian rays in from the top as shown in Fig. 1(c) and average over the efficiency of each individual initial ray in order to calculate the Beer-Lambert efficiency. We chose to use $\lambda = 500\ \text{nm}$ in Eq. (9) for comparison with FDTD calculations, which will be presented in Sec. IV D. The initial conditions of the 5000 rays are evenly spread over the interval $x \in (0, 5)$. Since only the film is absorbing, the

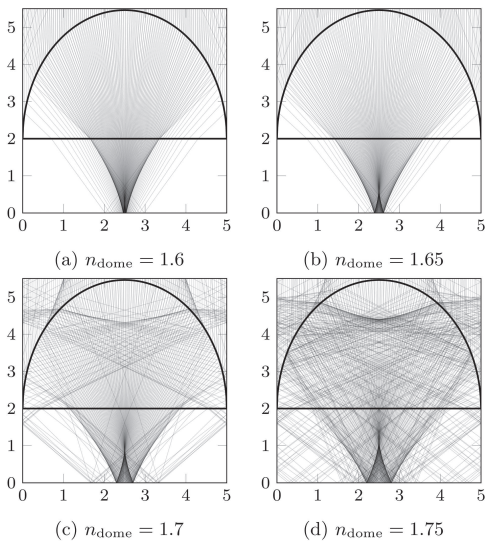


FIG. 5. Newtonian rays sent from the outside for different values of n_{dome} . At the breakpoint value $n_{\text{dome}} = 1.7$, the rays become sensitive to their initial condition.

trajectories will have to spend a long time inside of it, not only in the dome structure, in order to deposit their intensity. This motivates the desire for long-lived trajectories, which could be provided by chaotic ray dynamics. Figure 7 shows that the Beer-Lambert efficiency increases monotonically as a function of n_{dome} before it falls off for $n_{\text{dome}} > 2.1$. Using the $2\ \mu\text{m}$ thick film in Fig. 7(c) as an example, the increase in the Beer-Lambert efficiency starts slowly for $n_{\text{dome}} < 1.6$ and then increases rapidly after a critical value $n_{\text{dome}} = 1.6$. There is a systematic tendency of a slow increase for small values of n_{dome} , followed by a rapid increase at a critical value for all film thicknesses, although it is not so pronounced in the $0.5\ \mu\text{m}$ thick film example, Fig. 7(a). The reason why the Beer-Lambert efficiency falls off at about $n_{\text{dome}} > 2.1$ is due to the total internal reflection at the dome-film interface, which prevents rays from coming back into the absorbing film. This effect starts at $n_{\text{dome}} \gtrsim 2$, but the real impact on the Beer-Lambert efficiency is when $n_{\text{dome}} > 2.1$. This effect is more dramatic for the thicker film examples because the path-length difference between a ray going straight down into the film and one coming in at an angle is greater than for a very thin film layer. At this point, the box counting method loses its usefulness. The invariant set is small and sparse, so the fractal dimension of the scattering fractal looks to be dependent on the scale. This is why there are no data points for the fractal dimension in Fig. 7 for $n_{\text{dome}} > 2.1$.

Both the fractal dimension and the Beer-Lambert efficiency are shown in Fig. 7. We see a striking correlation between the onset of chaos and the start of the rapid increase in the Beer-Lambert efficiency. The proposed explanation of this correlation is

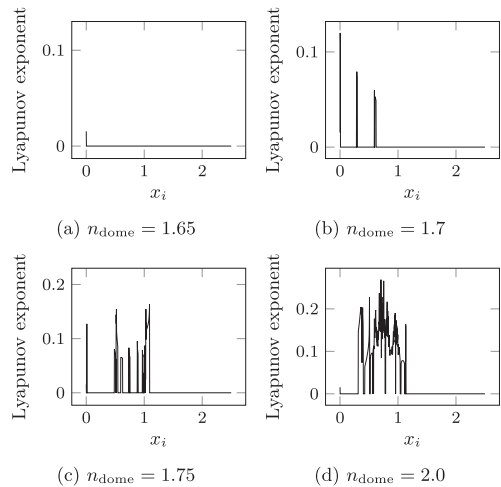


FIG. 6. Lyapunov exponents of Newtonian rays sent from the outside perpendicular with respect to the dome-film interface.

that the properties of chaotic scattering dynamics are beneficial for absorption efficiency modeled with the Beer-Lambert law because chaotic scattering, in conjunction with sticking to the chaotic repeller, leads to long trajectories inside of the absorbing film, which enhances the absorption. In addition, we demonstrated that chaos in the system leads to the spreading out of rays entering from the outside, a beneficial feature, which, again, leads to long trajectories with accompanying enhanced absorption, complex fractal boundaries in the invariant set as seen in the scattering fractals, which are “sticky,” and the existence of stable periodic orbits. The most notable periodic orbit that was found is the period-three orbit, as shown in Fig. 4(b). It leads to “slow hyperbolic corners” in which the movement of the trajectories in the PSOS slows down tremendously [as seen from the closeness of successive points in Fig. 4(b)] as they approach, and ultimately round, the period-three corners of the stable islands.

It must be noted that the sole purpose of plotting the fractal dimension together with the Beer-Lambert efficiency in Fig. 7 is to show that the fractal dimension drops below the threshold value 1.95 for the same n_{dome} as the Beer-Lambert efficiency starts to increase more rapidly. There is no one-to-one relationship between the two quantities.

D. FDTD simulations of the electric field

The classical ray model that we presented provides us with an approximation of the amount of absorbed energy in a dielectric material. A real solar cell has complex physical processes that are not taken into account and take place starting from when light first enters the device, to the point when electric power is produced. Our model aims to predict and explain the efficiency enhancement due to light

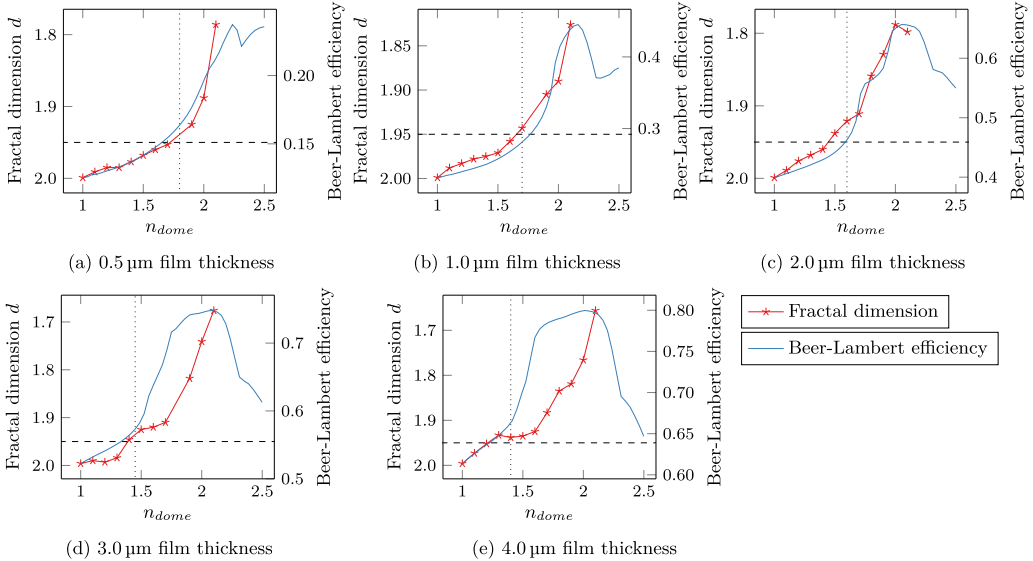


FIG. 7. Visualization of the fractal dimension (red) and the Beer-Lambert efficiency (blue). The onset of chaos is determined by the first data point below a fractal dimension of 1.95, indicated by a horizontal dashed line. The rapid increase of the Beer-Lambert efficiency is indicated by a vertical dotted line.

trapping, i.e., the increase in $1 - R$, on the basis of classical trajectory simulations. To prove that our ray-based results are relevant, we show here that full electromagnetic wave calculations, in the form of FDTD simulations of the film + dome system, corroborate what we have found in our classical simulations.

Our FDTD simulations are conducted in the following way. First, we chose our system, consisting of a dome of height $3.5 \mu\text{m}$ and an absorbing film of width $5 \mu\text{m}$, a thickness of $2 \mu\text{m}$, and a fixed index of refraction of $n_{\text{film}} = 2 + 0.0054i$. For this film + dome system, for each value of n_{dome} of a relatively dense set of n_{dome}

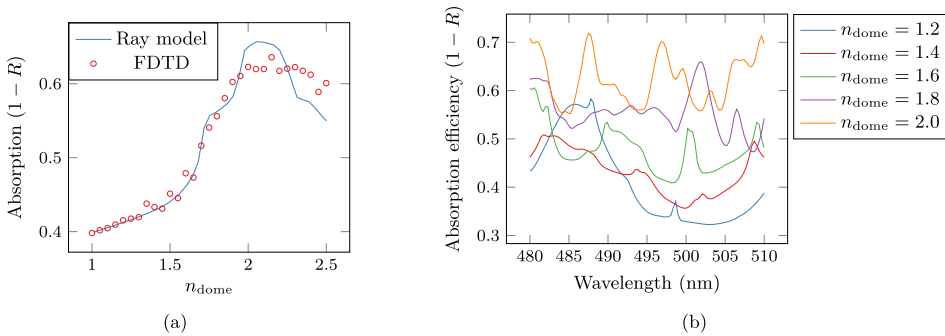


FIG. 8. (a) Absorption efficiency calculated with a commercial FDTD solver compared to the Beer-Lambert absorption efficiency calculated by rays. (b) Absorption efficiency as a function of wavelength calculated with FDTD for a range of n_{dome} . The number of resonances increases as n_{dome} increases.

values, ranging from $n_{\text{dome}} = 1$ in steps of $\Delta n_{\text{dome}} = 0.05$ to $n_{\text{dome}} = 2.5$, we computed the FDTD absorption value $1 - R$, and averaged $1 - R$ over wavelengths ranging from 480 nm in steps of 0.3 nm to 510 nm. The averaging mimics the fact that in practice solar cells are never irradiated with monochromatic light of a specific wavelength, but are irradiated with solar radiation, which is spread out over a range of wavelengths. As an additional, welcome benefit, the averaging smoothes over accidental wave resonances in our system, wave features that are clearly not present in our classical simulations. The result of our averaged FDTD simulations is shown in Fig. 8(a). We see that our classical simulations are very close to the full FDTD wave calculations, which shows that our classical ray simulations capture most of the (average) wave phenomena in our model solar cell. In addition, our FDTD simulations confirm the existence of the roughly three regions already presented and discussed in connection with Fig. 7, i.e., a slowly increasing region for $n_{\text{dome}} < 1.6$, a rapidly increasing region for $1.6 < n_{\text{dome}} < 2.1$, and a decreasing region for $n_{\text{dome}} > 2.1$. We explain the good agreement between the full-E&M FDTD calculations and our classical simulations on the basis that the wavelength of the incoming light

is much smaller than the system size. Therefore, the classical ray model approximates the full E&M wave solution very well, as seen in Fig. 8(a). While, as mentioned in Sec. III A, complete agreement between classical and wave calculations can be expected only if the classical rays are properly equipped with phases, which are neglected in our classical simulations, the averaging of our FDTD results over different wavelengths clearly contributes to de-emphasize the importance of phases, an expected result according to our discussion in Sec. III A.

For some selected values of n_{dome} , Fig. 8(b) shows the FDTD-computed resonance structures in the absorption $1 - R$ as a function of wavelength that we averaged over in Fig. 8(a). As the value of n_{dome} increases, the number of resonances in the selected frequency interval is seen to increase. This is easily understood on the basis that, for increasing n_{dome} , the effective wavelength inside of the dome material becomes shorter ($\lambda_{\text{dome}} = \lambda_{\text{vacuum}}/n_{\text{dome}}$), allowing more resonances to exist inside the fixed dome geometry.

An additional corroboration for the chaos transition at $n_{\text{dome}} \sim 1.5$ can be obtained by directly inspecting the wavefunctions in the film + dome system. To this end, we used the FDTD solver to compute the absolute square value, $|E|^2$, of the electric field, for four different values of n_{dome} (see Fig. 9). For small values of n_{dome} [Figs. 9(a) and 9(b)], the electric field behaves predictably. We see that, reminiscent of the behavior of the rays shown in Fig. 5, the dome is focusing the incoming light into the absorbing film, where a plane-wave-like resonance forms. For larger values of n_{dome} [see Figs. 9(c) and 9(d)], we see a distinct qualitative difference in the structure of $|E|^2$, showing complex wave patterns and so-called scarlets⁵⁴ that are a signature of chaos. In addition, whenever there is a transition from regular to chaotic dynamics, it is expected that at the transition to chaos the electric field starts to spread out over the entire available scattering volume. This phenomenon can, to some degree, also be seen directly in the $|E|^2$ patterns in Fig. 9.

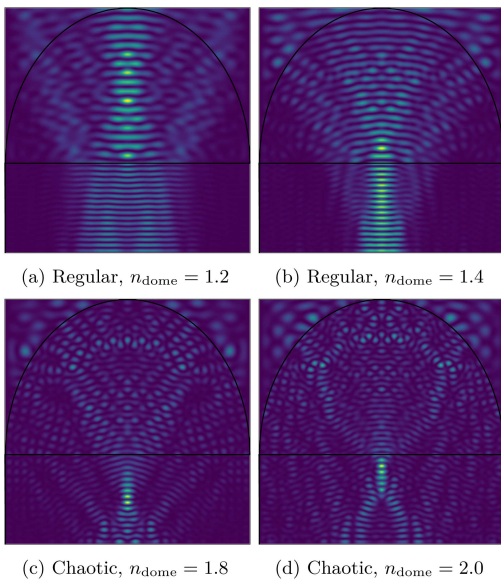


FIG. 9. FDTD simulations of the electric field inside the film + dome system for several values of n_{dome} . The black-line overlays show the shape of the film + dome system. The colors are chosen for the sole purpose of making clear visuals and to bring out the patterns in the electric field. Thus, the assignment of colors to electric field intensities is not necessarily the same for all four frames. Since only the structure of the field is of interest here, not the specifics of the intensities, color bars that would reflect the assignments of electric field intensities to colors are omitted.

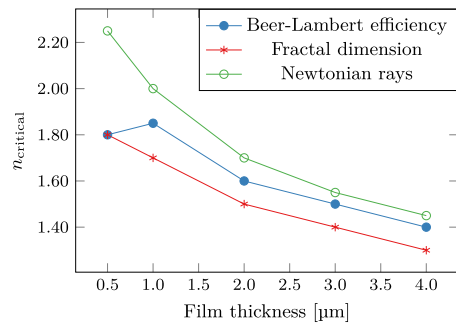


FIG. 10. The n_{critical} is the value for when the Beer-Lambert efficiency (blue) starts to increase more rapidly, the fractal dimension (red) is below 1.95, and the Newtonian rays sent from the outside directly downwards (green) visually start to behave sensitively on the initial condition. n_{critical} can be directly read off from Figs. 5 and 7. The lines between the dots are there to guide the eyes.

E. Structural stability

In Fig. 10, we summarize our results across the five film + dome systems we investigated, where film thickness was the independent parameter. The onset of chaos has been determined from the fractal dimension of the scattering fractals (see Fig. 7) and from visually inspecting the sensitivity of Newtonian rays to their initial conditions (see Fig. 5). There is a clear trend that shows that the onset of chaos correlates with the onset of the rapid enhancement of the Beer-Lambert efficiency.

V. CONCLUSION

We have evaluated absorption enhancement in a scattering system exhibiting a transition between regular and chaotic classical dynamics. The model system mimics a structured solar cell and was obtained by placing an elliptical dome structure on top of a flat absorbing film. A classical ray-tracing code was developed for modeling surface-structured optically thin solar cells. The Beer-Lambert law was used to model the absorption of light in the dielectric material.

We found that increasing the index of refraction inside the dome structure leads to a transition of the system from one that scatters regularly, to one with chaotic scattering dynamics. The scattering dynamics was investigated by calculating Lyapunov exponents and the fractal dimension of scattering fractals. We demonstrate that this transition from regular to chaotic dynamics goes along with an enhancement of the absorption efficiency in the film. Enhancing absorption efficiency by surface structuring is not new and is already well documented. However, in this paper, we have demonstrated that the onset of chaotic scattering dynamics is clearly correlated with absorption enhancement.

We, therefore, suggest to actively use the mechanism of chaos in the design of surface structures for solar cells. The classical ray model approximation presented in this paper represents one strategy for the establishment of a connection between chaotic scattering and absorption enhancement. It allows one to exploit this connection as a powerful guide for designing surface structures with a very high light-trapping efficiency for use in optically thin solar cells.

ACKNOWLEDGMENTS

This work was supported by the grant "Development of a new ray model for understanding the coupling between dielectric spheres for photovoltaics with higher efficiency" (No. 250678) financed by The Research Council of Norway. High-performance computing resources were provided by UNINETT Sigma2 through Grant No. NN9516K.

REFERENCES

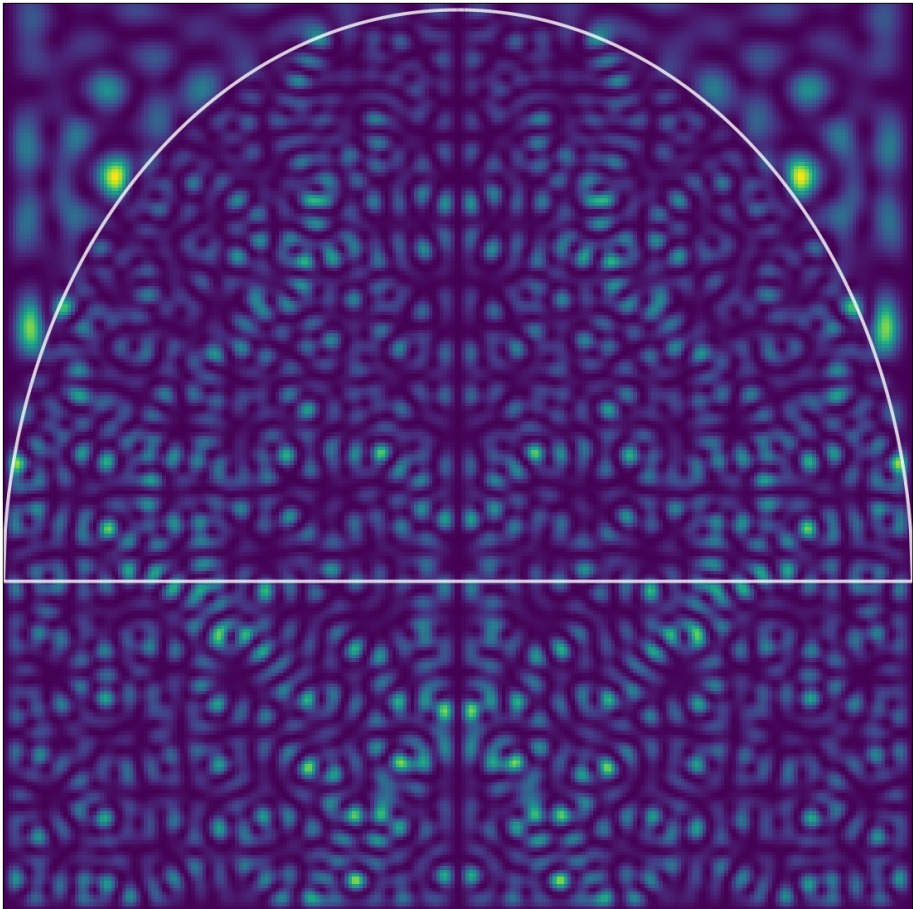
- ¹T. Tiedje, E. Yablonovitch, G. D. Cody, and B. G. Brooks, "Limiting efficiency of silicon solar cells," *IEEE Trans. Electron Dev.* **31**, 711–716 (1984).
- ²H. A. Atwater and A. Polman, "Plasmonics for improved photovoltaic devices," *Nat. Mater.* **9**, 205 (2010).
- ³J. Gjessing, E. S. Marstein, and A. Sudbø, "2D back-side diffraction grating for improved light trapping in thin silicon solar cells," *Opt. Express* **18**, 5481–5495 (2010).

- ⁴J. Gjessing, A. Sudbø, and E. Marstein, "A novel back-side light-trapping structure for thin silicon solar cells," *J. Eur. Opt. Soc. Rapid Publ.* **6**, 11020 (2011).
- ⁵C. Battaglia, C.-M. Hsu, K. Söderström, J. Escarré, F.-J. Haug, M. Charrière, M. Boccard, M. Despeisse, D. T. L. Alexander, M. Cantoni, Y. Cui, and C. Ballif, "Light trapping in solar cells: Can periodic beat random?," *ACS Nano* **6**, 2790–2797 (2012).
- ⁶P. Kowalczycki, M. Liscidini, and L. C. Andreani, "Light trapping in thin-film solar cells with randomly rough and hybrid textures," *Opt. Express* **21**, A808–A820 (2013).
- ⁷Q. Tang, H. Shen, H. Yao, K. Gao, Y. Jiang, Y. Li, Y. Liu, L. Zhang, Z. Ni, and Q. Wei, "Superiority of random inverted nanopillar as efficient light trapping structure in ultrathin flexible c-Si solar cell," *Renew. Energy* **133**, 883–892 (2019).
- ⁸Y. Xu and Y. Xuan, "Photon management of full-spectrum solar energy through integrated honeycomb/cone nanostructures," *Opt. Commun.* **430**, 440–449 (2019).
- ⁹J. Grandier, D. M. Callahan, J. N. Munday, and H. A. Atwater, "Light absorption enhancement in thin-film solar cells using whispering gallery modes in dielectric nanospheres," *Adv. Mater.* **23**, 1272–1276 (2011).
- ¹⁰E. Yablonovitch, "Statistical ray optics," *J. Opt. Soc. Am.* **72**, 899–907 (1982).
- ¹¹F. Haake, *Quantum Signatures of Chaos*, 3rd ed. (Springer, Berlin, 2010).
- ¹²H.-J. Stockmann, *Quantum Chaos: An Introduction* (Cambridge University Press, Cambridge, 2000).
- ¹³M. C. Gutzwiller, *Chaos in Classical and Quantum Mechanics* (Springer, New York, 1990).
- ¹⁴H. Poincaré, "Introduction," *Acta Math.* **13**, 5–7 (1890).
- ¹⁵E. N. Lorenz, "Deterministic nonperiodic flow," *J. Atmos. Sci.* **20**, 130–141 (1963).
- ¹⁶I. Hadamard, "Les surfaces à courbures opposées et leurs lignes géodésiques," *J. Math. Pures Appl.* **4**, 27–74 (1898).
- ¹⁷L. A. Bunimovich, "On the ergodic properties of nowhere dispersing billiards," *Commun. Math. Phys.* **65**, 295–312 (1979).
- ¹⁸L. A. Bunimovich, "On ergodic properties of certain billiards," *Funct. Anal. Appl.* **8**, 254–255 (1974).
- ¹⁹L. A. Bunimovich, "Decay of correlations in dynamical systems with chaotic behavior," *Zh. Eksp. Teor. Fiz.* **89**, 1452–1471 (1985).
- ²⁰H. Cao and J. Wiersig, "Dielectric microcavities: Model systems for wave chaos and non-Hermitian physics," *Rev. Mod. Phys.* **87**, 61–111 (2015).
- ²¹E. G. Altmann, J. S. E. Portela, and T. Tél, "Leaking chaotic systems," *Rev. Mod. Phys.* **85**, 869–918 (2013).
- ²²L. Sirko, P. M. Koch, and R. Blümel, "Experimental identification of non-Newtonian orbits produced by ray splitting in a dielectric-loaded microwave cavity," *Phys. Rev. Lett.* **78**, 2940–2943 (1997).
- ²³E. Ott and T. Tél, "Chaotic scattering: An introduction," *Chaos* **3**, 417–426 (1993).
- ²⁴P. Gaspard and S. A. Rice, "Scattering from a classically chaotic repeller," *J. Chem. Phys.* **90**, 2225–2241 (1989).
- ²⁵J. Hietarinta and S. Mikkola, "Chaos in the one-dimensional gravitational three-body problem," *Chaos* **3**, 183–203 (1993).
- ²⁶P. T. Boyd and S. L. W. McMillan, "Chaotic scattering in the gravitational three-body problem," *Chaos* **3**, 507–523 (1993).
- ²⁷A. A. Chernikov and G. Schmidt, "Chaotic scattering and acceleration of particles by waves," *Chaos* **3**, 525–528 (1993).
- ²⁸K. Richter and D. Wintgen, "Analysis of classical motion on the Wannier ridge," *J. Phys.: At. Mol. Opt. Phys.* **23**, L197–L201 (1990).
- ²⁹T. Yamamoto and K. Kaneko, "Helium atom as a classical three-body problem," *Phys. Rev. Lett.* **70**, 1928–1931 (1993).
- ³⁰C. F. Hillermeier, R. Blümel, and U. Smilansky, "Ionization of H Rydberg atoms: Fractals and power-law decay," *Phys. Rev. A* **45**, 3486–3502 (1992).
- ³¹J. M. Seoane and M. A. F. Sanjuán, "New developments in classical chaotic scattering," *Rep. Progress Phys.* **76**, 016001 (2012).
- ³²A. Kohler and R. Blümel, "Annular ray-splitting billiard," *Phys. Lett. A* **238**, 271–277 (1998).
- ³³A. Kohler and R. Blümel, "Signature of periodic lateral-ray orbits in a rectangular ray-splitting billiard," *Phys. Lett. A* **247**, 87–92 (1998).

- ³⁴A. Kohler and R. Blümel, "Test of semiclassical amplitudes for quantum ray-splitting systems," *Phys. Rev. E* **59**, 7228–7230 (1999).
- ³⁵A. Kohler, G. H. M. Killesreiter, and R. Blümel, "Ray splitting in a class of chaotic triangular step billiards," *Phys. Rev. E* **56**, 2691–2701 (1997).
- ³⁶A. Kohler and R. Blümel, "Weyl formulas for quantum ray-splitting billiards," *Ann. Phys.* **267**, 249–280 (1998).
- ³⁷N. Savitskiy, A. Kohler, S. Bauch, R. Blümel, and L. Sirko, "Parametric correlations of the energy levels of ray-splitting billiards," *Phys. Rev. E* **64**, 036211 (2001).
- ³⁸Y. Hlushchuk, A. Kohler, S. Bauch, L. Sirko, R. Blümel, M. Barth, and H.-J. Stöckmann, "Autocorrelation function of level velocities for ray-splitting billiards," *Phys. Rev. E* **61**, 366–370 (2000).
- ³⁹M. Mariano, G. Kozyreff, L. G. Gerling, P. Romero-Gomez, J. Puigdollers, J. Bravo-Abad, and J. Martorell, "Intermittent chaos for ergodic light trapping in a photonic fiber plate," *Light Sci Appl.* **5**, e16216 (2016).
- ⁴⁰R. Blümel and W. P. Reinhardt, *Chaos in Atomic Physics* (Cambridge University Press, 1997).
- ⁴¹P. Cvitanović, R. Artuso, R. Mainieri, G. Tanner, and G. Vattay, *Chaos: Classical and Quantum* (Niels Bohr Institute, Copenhagen, 2016).
- ⁴²L. P. Kadanoff and C. Tang, "Escape from strange repellers," *Proc. Natl. Acad. Sci. U.S.A.* **81**, 1276–1279 (1984).
- ⁴³B. Mandelbrot, "How long is the Coast of Britain? Statistical self-similarity and fractional dimension," *Science* **156**, 636–638 (1967), see <http://science.sciencemag.org/content/156/3775/636.full.pdf>.
- ⁴⁴B. Klinkenberg, "A review of methods used to determine the fractal dimension of linear features," *Math. Geol.* **26**, 23–46 (1994).
- ⁴⁵T. Smith, G. Lange, and W. Marks, "Fractal methods and results in cellular morphology—Dimensions, lacunarity and multifractals," *J. Neurosci. Methods* **69**, 123–136 (1996).
- ⁴⁶A. Kohler, G. H. M. Killesreiter, and R. Blümel, "Ray splitting in a class of chaotic triangular step billiards," *Phys. Rev. E* **56**, 2691–2701 (1997).
- ⁴⁷A. Kohler, "Classical and quantum implications of ray splitting," Ph.D. thesis (Albert-Ludwigs-Universität Freiburg i.Br., 1998).
- ⁴⁸M. A. Green, "Self-consistent optical parameters of intrinsic silicon at 300 K including temperature coefficients," *Solar Energy Mater. Solar Cells* **92**, 1305–1310 (2008).
- ⁴⁹M. Brandsrud, E. Seim, R. Lukacs, A. Kohler, E. Marstein, E. Olsen, and R. Blümel, "Exact ray theory for the calculation of the optical generation rate in optically thin solar cells," *Physica E* **105**, 125–138 (2019).
- ⁵⁰P. C. Chang, J. Walker, and K. Hopcraft, "Ray tracing in absorbing media," *J. Q. Spectrosc. Radiat. Transf.* **96**, 327–341 (2005).
- ⁵¹M. A. Dupertuis, M. Proctor, and B. Acklin, "Generalization of complex Snell–Descartes and Fresnel laws," *J. Opt. Soc. Am. A* **11**, 1159–1166 (1994).
- ⁵²Lumerical Inc., see lumerical.com for "FDTD Solutions" (2019).
- ⁵³E. Ott, *Chaos in Dynamical Systems* (Cambridge University Press, Cambridge, 1993).
- ⁵⁴E. J. Heller, "Bound-state eigenfunctions of classically chaotic Hamiltonian systems: Scars of periodic orbits," *Phys. Rev. Lett.* **53**, 1515–1518 (1984).

Appendix C

Paper III



Wave chaos enhanced light trapping in optically thin solar cells

E. Seim,^{1, a)} A. Kohler,¹ R. Lukacs,¹ M. A. Brandsrud,¹ E. S. Marstein,^{2, 3} E. Olsen,¹ and R. Blümel⁴

¹⁾RealTek, Norwegian University of Life Sciences, Ås, 1430, Norway

²⁾Department of Solar Energy, Institute of Energy Technology, Kjeller, 2007, Norway

³⁾Department of Technology Systems, University of Oslo, Oslo, 0371, Norway

⁴⁾Department of Physics, Wesleyan University, Middletown, CT 06457, USA

(Dated: 18 October 2019)

Enhancing the energy output of solar cells increases their competitiveness as a source of energy. Producing thinner solar cells is attractive, but a thin absorbing layer demands excellent light management in order to keep transmission related losses of incoming photons at a minimum. We maximize absorption by trapping light rays to make the mean average path length in the absorber as long as possible. In chaotic scattering systems there are ray trajectories with very long lifetimes. In this paper we investigate the scattering dynamics of waves in a model system using principles from the field of quantum chaotic scattering. We quantitatively find that the transition from regular to chaotic scattering dynamics correlates with the enhancement of the absorption cross section, and propose the use of an autocorrelation function to assess the average path length of rays as a possible way to verify the light-trapping efficiency experimentally.

Classical chaotic scattering lead to trapped rays with long lifetimes which are of importance in improving light management for more efficient solar cells. In this paper we study the wave dynamics in solar cell models with proven chaotic dynamics on the classical level. We show a connection between the emergence of wave chaos and enhancement of absorption efficiency due to light trapping.

material a weak absorber. To mitigate the losses from creating thinner solar cells, smart management of light is required. If the incoming light is effectively trapped within a solar cell, the transmission and reflection losses are minimized, thus maximizing the efficiency. Moreover, thinner solar cells entail additional benefits by being less prone to bulk recombination and having better voltage characteristics.

The concept of light-trapping is often analyzed from the perspective of geometric optics. The goal is to force photons from the incoming sunlight into rays that stay long enough in the absorbing layer of the solar cell to excite electrons and holes. To achieve long-lived ray trajectories, one must control the dynamics of the incoming light rays. In general, improved light trapping is engineered by creating or adding structures or textures. They can be on the surface, on the back side of the solar cell or they may be realized as advanced plasmonic structures^{6–13}.

Solar cells are ray-splitting systems since the surface of the solar cells acts as a ray-splitting boundary where rays are reflected or transmitted according to probabilities given by the Fresnel equations¹⁴. Ray-splitting dynamics has been studied extensively in the context of chaotic scattering^{15–18}, in which ray splitting^{19–25} and ray trapping^{26,27} play a major role. Both concepts are of central relevance to light trapping in solar cell applications. Ray trapping is connected to the defining property of a system exhibiting chaotic dynamics, which is the hypersensitivity to initial conditions. The presence of chaotic dynamics has interesting implications in the context of absorption in solar cells. Bunimovich showed that dynamics in a Bunimovich billiard, a bounded dynamical system, is ergodic^{28,29}, meaning that the whole energetically accessible phase space of the system is visited by a generic ray, i.e., a ray started with initial conditions that are not too special. If ergodic rays are present in a solar cell, it means that incoming rays are deflected away from the vertical direction, resulting in a longer average

I. INTRODUCTION

The demand for renewable energy is driven by the need for producing clean energy to meet climate and sustainability goals. Photovoltaic solar cells is a rapidly growing technology which has resulted in a tremendous increase in photovoltaics (PV) energy production over the last decade. From 2010 to 2018 the world-wide total installed capacity increased more than tenfold from 40 GW_p to over 500 GW_p¹. The share of PV is now 2.6% of the total electricity generated globally and covers 4.3% of European energy demand. To become even more competitive, the price per GW_p needs to be lowered. The efficiency of solar cells is the most important metric to improve in this regard. Single-junction silicon-based technology is by far the most commonly used technology today. This technology has matured to the point that the theoretical Shockley–Queisser limit of 29% is almost realized^{2,3} as shown by the current demonstrated PV cell record for crystalline Si of 26.7%^{4,5}. However, producing thin solar cells reduces the cost and environmental footprint at the expense of efficiency, since the absorbing layer is less likely to absorb light than a thicker cell would, and, in the case of silicon, the indirect band gap makes the

^{a)}eivind.seim@nmbu.no

path lengths³⁰. There are few reports of the benefits of chaotic scattering dynamics in solar cells. Mariano *et al.*³¹ report experimental and computational findings that a solar cell integrated on a special photonic fiber plate leads to an optically ergodic system and a greatly enhanced light absorption. Using classical ray tracing calculations and verifying the results with a commercial finite-difference time-domain (FDTD) solver, Seim *et al.*³² recently showed that the transition from regular to chaotic scattering dynamics correlates with the enhancement of the absorption efficiency. The result was proven for a model system with a shape akin to a Bunimovich billiard, where the transition from regular to chaotic scattering was controlled by a single parameter. It was also shown that the result was structurally stable, i.e., it was not sensitive with respect to the system parameters chosen. This is a very important property for the successful technical realization of such a system: If the phenomenon was only valid for a special, exactly realized shape, one could never expect to be able to reproduce the shape in the lab, let alone in a large-scale industrial process.

While in systems of any dimension geometrical ray optics and electromagnetic (E&M) wave simulations produce comparable results in the short wavelength limit, in two or more dimensions there is not a general ray theory known to the authors that is exact for systems that cannot be considered to be within the geometrical optics limit. However, in effectively one-dimensional systems, for instance a stack of planar films, an exact ray theory exists³³. In higher-dimensional systems we are therefore in need of E&M wave calculations for simulating optical systems and obtaining their optical properties accurately. A solar cell is an inherently wave-mechanical scattering system. In terms of scattering dynamics, the dynamics on the wave level “feel” the underlying classical dynamics¹⁷, but chaos on the classical level does not necessarily imply chaos on the wave level, more commonly called *wave chaos*. The aim of this paper is to confirm the findings of Seim *et al.*³² by applying techniques from the fields of quantum and wave chaos to extend our knowledge of how chaos can improve the light-trapping properties in surface-structured solar cells.

We start out by presenting a very brief account of the aspects of classical and quantum chaos that are relevant in the context of this paper, enhancing the light trapping in solar cells. The next section explains the model system and the numerical methods used. Then the results are presented in two parts, the first highlights the appearance of chaotic signatures and the enhancement of the absorption efficiency as an effect of varying a system parameter. The second part shows that these effects are tied to the transition from the regular to the chaotic scattering regime. The results and usefulness to light trapping are summarized in the conclusions at the end of the paper.

II. CLASSICAL AND QUANTUM CHAOS

Chaos is a phenomenon that is seen in certain dynamical systems. The defining trait of chaotic systems is that the dynamical motion is strongly dependent on the initial conditions. Chaos is divided into two separate, but connected fields, classical chaos and wave chaos.

A. Classical chaos

Classical chaos started with Jacques Hadamard in 1898 with his study of exponential divergence of rays in a dynamical billiard. The rays in dynamical billiards are the trajectories they trace out as particles move on a surface bounded by reflecting walls. Dynamical billiards are therefore closed systems. Various closed systems with chaotic dynamics have been studied in great detail, with the perhaps most extensively studied being the Sinai and Bunimovich billiards^{34,35}. The open counterpart to bounded billiard systems are called scattering systems¹⁶. Classical chaos in ray systems is often characterized by how two rays with very similar initial conditions separate from each other in phase space as a function of time. In regular systems without chaos, the separation is linear in time, while in irregular chaotic systems the separation is exponential. The Lyapunov exponent λ gives the rate of divergence

$$s(t) = e^{\lambda t} s(0), \quad (1)$$

where $s(0)$ is the initial separation distance, and $s(t)$ is the separation at a time t . A positive Lyapunov exponent is needed for exponential divergence and is therefore used as a tool to diagnose chaos in a system.

B. Quantum chaos

Quantum chaos, or more generally wave chaos, is a dynamical phenomenon that may occur quite generally in all wave systems. Wave chaos can appear in real, complex, as well as vector fields, and the governing wave equations can be linear equations such as the Schrödinger equation or Maxwell’s equations, or they can be non-linear such as the Gross-Pitaevskii equation³⁶.

In 1955 Wigner introduced random matrices to model the spectra of heavy atomic nuclei^{37,38}. Together with Dyson, Mehta, and others, random matrix theory was developed^{36,39}. One of the central results is the Wigner surmise. It postulates the probability density function, $P(s)$, of a sequence of nearest neighbor spacings between energy levels in heavy nuclei. It is given by

$$P(s) = \frac{\pi s}{2} e^{-\pi s^2/4}, \quad (2)$$

where $s = s'/D$ with s' being a particular nearest neighbor spacing and D being the mean distance between

neighboring energy levels. Eq. (2) is commonly referred to as the Wigner surmise or the Wigner distribution. The class of random matrices that this particular version of the Wigner distribution is universal for is called the Gaussian orthogonal ensemble (GOE)^{40,41}. Later, it was conjectured by Bohigas, Giannoni, and Schmit that all chaotic systems have the universality of the Wigner distribution predicted by random matrix theory⁴². Confidence in the conjecture was built over the years by a large amount of evidence^{36,39,43}. It is generally agreed upon that (generic) regular systems have Poissonian level distributions⁴⁴⁻⁴⁶, and that (generic, time-reversal invariant) chaotic systems have level distributions fitting the Wigner surmise^{42,47,48}.

The transition from regular to chaotic dynamics has been studied in the context of universality in the S matrix fluctuations^{44,49}. Berry and Robnik⁵⁰, and Brody^{51,52} have developed models to make quantitative predictions for the level statistics as a system gradually becomes more irregular. These models are interpolations between the Poisson and Wigner distributions. The Berry-Robnik distribution is

$$P_{BR}(S, \rho) = \rho^2 e^{-\rho S} \operatorname{erfc}(\sqrt{\pi} \bar{\rho} S/2) + (2\rho \bar{\rho} + \pi \bar{\rho}^3 S/2) e^{-\rho S - \pi \bar{\rho}^2 S^2/4}, \quad (3)$$

where $\bar{\rho} = 1 - \rho$ is the fraction of chaos in the available phase space. Brody's distribution is

$$P_B(S, \omega) = \alpha(\omega + 1) S^\omega e^{-\alpha S^{\omega+1}}, \quad (4)$$

where

$$\alpha = \left[\Gamma\left(\frac{\omega + 2}{\omega + 1}\right) \right]^{\omega+1}, \quad (5)$$

and ω is a measure of the level repulsion. Thus, $\omega = 0$ yields the Poisson distribution and $\omega = 1$ yields the Wigner surmise. However, the ω in the Brody distribution does not have a rigorous physical interpretation like the ρ has in the Berry-Robnik distribution. We use these distributions later on as tools to quantify the onset of chaos in a model system by comparing them to histograms of level statistics.

III. THE FILM+DOME SYSTEM

The model system shown in Fig. 1a is a scattering system. It is comprised of three mirrors arranged like a bucket (left, bottom, and right), while the system is open at the top, where it has a non-absorbing dome structure placed on top of a light-absorbing film. Both structures, i.e., film and dome, are characterized by their index of refraction, $n_{\text{film}} \in \mathbb{C}$ and $n_{\text{dome}} \in \mathbb{R}$ respectively. We call this the film+dome system. Because our aim is to study the effects of wave chaos in an optically thin surface-structured solar cell, we model the absorption capabilities of the solar cell by the imaginary part of the index

of refraction alone, without any additional device modeling. Thus, the approach chosen is well suited to study scattering phenomena. The aim is not to predict the I-V characteristics of an experimental realization of the same system. We have previously investigated the classical dynamics of the same system³².

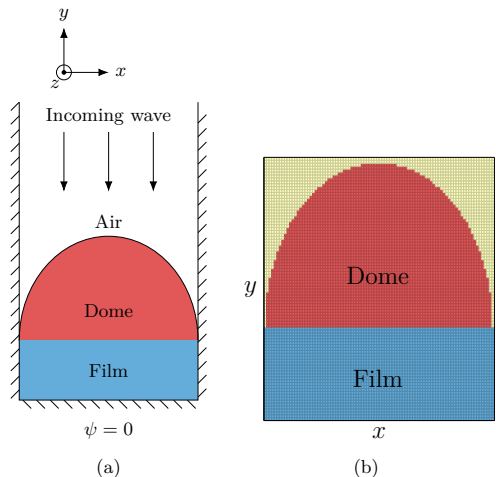


FIG. 1: (a) The film+dome scattering system is enclosed in a mirror-shaped bucket. (b) The discretized film+dome system.

The scattering problem depicted in Fig. 1a is two-dimensional, but equivalent to the three-dimensional problem where the structure is extended out of the two-dimensional plane of the picture, i.e., we assume cylindrical symmetry along the z -axis. In this geometry it is convenient to assume that the polarization of the incoming radiation is pointing along the z direction of the extended structure, since this allows for a two-dimensional description of the associated E&M wave problem. As a consequence of this assumption, the polarization is always perpendicular to the plane of incidence. In this case the E&M wave equation is the Helmholtz equation. It is interesting to note that the problem is completely analogous to the time-independent Schrödinger equation if the solutions are assumed to be separable in time and space. We solve the Helmholtz equation to get the steady state solutions of the scattering problem

$$(\nabla^2 + n^2 K^2)\psi = 0, \quad (6)$$

where n is the complex index of refraction in the two-dimensional region enclosed by the mirrors, $x \in [0, w]$ and $y \in [0, \infty]$. We opt to solve the Helmholtz equation by using the Green's function method. The Green's func-

tion, $G(x, x', y, y'; K)$, obeys the boundary conditions

$$\psi(x, 0) = 0, \quad (7a)$$

$$\psi(0, y) = \psi(w, y) = 0, \quad (7b)$$

and is thus constructed by the normalized eigenfunctions

$$\phi_{mk}(x, y) = \frac{2}{\sqrt{\pi w}} \sin\left(\frac{m\pi x}{w}\right) \sin(ky), \quad (8)$$

where $k \in \mathbb{R}$ and $m \in \mathbb{N}$. $G(x, x', y, y'; K)$ is now constructed according to

$$G(x, x', y, y'; K) = \sum_{m=-\infty}^{\infty} \int_0^{\infty} \frac{\phi_{mk}(x, y) \phi_{mk}(x', y') dk}{K^2 - \frac{\pi^2 m^2}{w^2} - k^2}. \quad (9)$$

The full derivation of $G(x, x', y, y'; K)$ can be found in Appendix VI. Depending on whether K is real or complex, we split $G(x, x', y, y'; K)$ into two branches, the open and closed channels

$$K^2 - \frac{\pi^2 m^2}{w^2} > 0, \quad \text{Open channels}, \quad (10)$$

$$K^2 - \frac{\pi^2 m^2}{w^2} < 0, \quad \text{Closed channels}, \quad (11)$$

respectively. The complete Green's function is divided into two expressions

$$G_{open} = \sum_{m=1}^M \frac{i}{wB_m} \sin\left(\frac{m\pi x}{w}\right) \sin\left(\frac{m\pi x'}{w}\right) \times \left[e^{iB_m(y+y')} - e^{iB_m|y-y'|} \right], \quad (12)$$

$$G_{closed} = \sum_{m=M+1}^{\infty} \frac{1}{wA_m} \sin\left(\frac{m\pi x}{w}\right) \sin\left(\frac{m\pi x'}{w}\right) \times \left[e^{-A_m(y+y')} - e^{-A_m|y-y'|} \right], \quad (13)$$

with $A_m = \sqrt{\frac{\pi^2 m^2}{w^2} - K^2}$, $B_m = \sqrt{K^2 - \frac{\pi^2 m^2}{w^2}}$, and M is the number of open channels available given by the floor function

$$M = \left\lfloor \frac{Kw}{\pi} \right\rfloor. \quad (14)$$

The allowed incoming waves are plane waves traveling along the y -axis in the negative direction, weighted by a sine function in the x -direction. They are of the form

$$\psi_{in} = e^{-ik_y y} \sin(k_x x), \quad (15)$$

where $k_x = p\pi/w$, and p is a positive integer. For each value of p there is an open channel associated with an incoming wave. The wavelength λ of the incoming wave is given by $k_y = 2\pi/\lambda$, and K is defined in relation to k_y and k_x in the following way:

$$K^2 = k_y^2 + k_x^2. \quad (16)$$

Three film+dome systems were evaluated in order to ensure that the results are not dependent on special system parameters, i.e., to ensure structural stability. All three film+dome systems investigated consist of a $5 \mu\text{m}$ wide absorbing film with index of refraction $n_{\text{film}} = 2 + 0.0054i$. The three films are $1 \mu\text{m}$, $2 \mu\text{m}$, and $3 \mu\text{m}$ thick, while the dome is $3.46 \mu\text{m}$ tall and $5 \mu\text{m}$ wide. The index of refraction in the dome, n_{dome} , is the variable parameter. Silicon is not a very good light absorber at 800 nm , the imaginary part of n_{film} was therefore set to the refractive index of silicon at 800 nm , truncated to four decimals. The value should therefore be a good choice when looking to improve absorption properties.

A. Absorption cross section

The solution of the non-free Helmholtz equation can be found using the Lippmann-Schwinger formula

$$\psi_p(x, y) = \phi_p(x, y) - \int G(K, x, x', y, y') K^2 \times [1 - n(x', y')^2] \psi_p(x', y') dx' dy', \quad (17)$$

where $\phi(x, y)$ is one of the M free solutions, meaning no dielectric material in the bucket-shaped mirror configuration. The free solution for each open channel available to the system is differing only in the sine envelope, which is controlled by the parameter p ; hence the subscript in Eq (17). This formula can be reformulated into a matrix problem of the form $Ax = b$ for obtaining a quick numerical solution. The absorption cross section, which previously has been shown to be $1 - R$, with R being the reflectivity³³, is calculated directly from the wave function ψ according to

$$\sigma = \frac{4\pi}{\lambda w} \int n_r(x, y) n_i(x, y) \psi(x, y) dx dy, \quad (18)$$

where n_r and n_i are the real and imaginary parts of the complex index of refraction, respectively. In addition to the Green's function method, the absorption cross section was also calculated using a commercial FDTD solver⁵³. The wave function in Eq. 18 is then substituted with the electrical field obtained from the FDTD solver when the system reaches the steady state. Note that these programs differ in how the calculation is performed. In the Green's function method incoming waves with correct shape according to ((15)) are injected into the bucket, while in the FDTD solver a plane wave is sent towards a bucket with an infinite height. These two methods, however, are equivalent to a high degree of accuracy since the incoming plane wave in the FDTD solver, once hits the mirrors of the bucket, very quickly adjusts to the correct mirror boundary conditions.

B. Computing the scattering matrix

For an incoming wave in channel p , the solution of the free problem is

$$\phi_p = (e^{-ik_y y} - e^{ik_y y}) \sin\left(\frac{p\pi x}{w}\right) \quad (19)$$

and we expect the scattered wave function to be a mixture of all possible waves allowed in the system, which is of the form

$$\psi_p = \sum_{m=1}^M S_{p \rightarrow m} e^{iB_m y} \sin\left(\frac{p\pi x}{w}\right) \quad (20)$$

in the asymptotic limit, i.e. $y \rightarrow \infty$. $S_{p \rightarrow m}$ denotes the scattering amplitude from the initial channel p to the final channel m . In this limit the open-channel Green's function is

$$\begin{aligned} \lim_{y \rightarrow \infty} G_{open} &= G_{open}^{(y \rightarrow \infty)} = \sum_{m=1}^M \frac{-2}{w B_m} \sin\left(\frac{m\pi x}{w}\right) \\ &\times \sin\left(\frac{m\pi x'}{w}\right) e^{iB_m y} \sin(B_m y'). \end{aligned} \quad (21)$$

Now, inserting $G_{open}^{(y \rightarrow \infty)}$ into the Lippmann-Schwinger equation yields

$$\begin{aligned} \psi_p &= \phi_p^{(y \rightarrow \infty)} + \int G_{open}^{(y \rightarrow \infty)}(x, x', y, y') K^2 \\ &\times [1 - n(x', y')^2] \Psi_p(x', y') dx' dy', \end{aligned} \quad (22)$$

from which, by comparing with (20), we can read off the scattering matrix elements

$$\begin{aligned} S_{p \rightarrow q} &= -\delta_{pq} - \frac{2K^2}{w B_q} \int \sin\left(\frac{q\pi x'}{w}\right) \sin(B_q y') \\ &\times [1 - n(x', y')^2] \psi_p(x', y') dx' dy'. \end{aligned} \quad (23)$$

IV. RESULTS AND DISCUSSION

A. Enhancement of the absorption cross section

We calculated the absorption cross section according to Eq. (18) for the film+dome system as a function of the index of refraction, n_{dome} , for three film+dome systems. Figure 2 shows a comparison of the average absorption cross section $\langle \sigma \rangle_\lambda$, resulting from an average over a wavelength range spanning from 480 nm to 510 nm, between FDTD, $\langle \sigma_{FDTD} \rangle$, and the Green's function method, $\langle \sigma_{GF} \rangle$. The Beer-Lambert efficiency, obtained from classical ray calculations is also shown. These classical ray calculations were carried out using a ray-tracer software written specifically for the purpose of classical ray simulations. The details of the calculations can be found in³². The FDTD and ray results agree very

well. We expect this since the systems are close to the geometrical optics limit with the wavelengths being about ten times smaller than the total width of the systems. The $\langle \sigma_{GF} \rangle$ data are computed using the first channel wave function, which has the form $e^{-ik_y y} \sin(k_x x)$. The agreement with $\langle \sigma_{FDTD} \rangle$ is therefore not expected to be one-to-one since the incoming wave forms used in the two wave calculations (FDTD and Green's function method) are different. A plane wave is used in the FDTD calculation. However, the point here is not to make a direct comparison between the FDTD solver and the Green's function calculations, but to qualitatively search for the same behavior in $\langle \sigma \rangle_\lambda$ as a function of n_{dome} using rays, FDTD, and the Green's function approach. The agreement between the full wave FDTD and the first-channel Green's function calculation is good, despite the difference mentioned previously between the two programs.

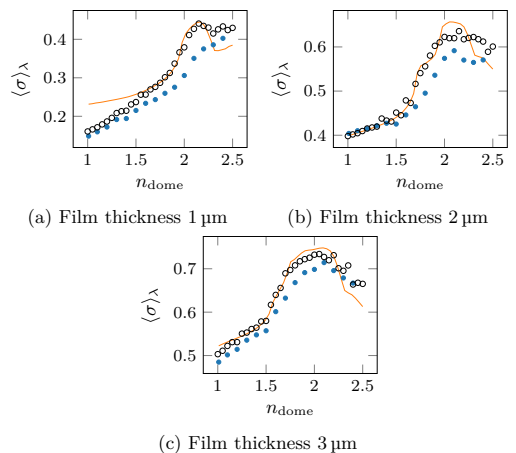


FIG. 2: Average absorption cross section $\langle \sigma \rangle_\lambda$, obtained by averaging $\sigma(\lambda)$ over a wavelength interval from 480 nm to 510 nm, calculated using FDTD (black circles) and a Green's function approach (blue dots). For all three film thicknesses a rapid increase in $\langle \sigma \rangle_\lambda$ is seen when n_{dome} is sufficiently large. The orange curve shows the efficiency calculated by geometric rays, including ray splitting, using Beer-Lambert's law to model absorption³².

All three models show an increase in the average absorption efficiency, $\langle \sigma \rangle_\lambda$, as n_{dome} is increased, with a maximum between 2.0 and 2.3. This holds true for all the systems with different film thicknesses. More importantly, at a certain n_{dome} , $\langle \sigma \rangle_\lambda$ rapidly increases, hinting at a change of the dynamical behavior. This critical point is seen at about $n_{dome} = 1.85$, $n_{dome} = 1.6$ and $n_{dome} = 1.5$ for the systems with film thicknesses 1 μm , 2 μm , and 3 μm , respectively, with respect to the classical ray data (orange curve in Fig. 2). In other words, the phenomenon of the critical point with increasingly

rapid enhancement of $\langle\sigma\rangle_\lambda$ is structurally stable, i.e., it does not depend on a strict choice of system parameters. However, the value of n_{dome} for which the critical point occurs does depend on the relative size difference of the film and dome. For instance, in the 1 μm thick film, the effect appears at a higher n_{dome} compared to the 3 μm thick film and is also stronger.

This specific wavelength range, 480 nm to 510 nm, was chosen because it contains a large part of the solar spectrum while keeping the number of open channels available, dictated by Eq. (14), in the system as large as possible. Care must be taken when calculating $\langle\sigma\rangle_\lambda$ over finite wavelength intervals. The rule of thumb is that the interval must be broad enough to cover the average of σ to get a good agreement between the FDTD and classical ray calculations, which are not dependent on the wavelength in the same way as in FDTD. Using the 2 μm thick film as an example, we see, in Fig. 3a, that roughly one “period” of σ is included in the chosen interval. Generally, σ is not expected to look periodic, but for small values of n_{dome} , the system is essentially just a film, which shows smooth, rolling fluctuations. One “period” of these fluctuations captures the average of σ . In Fig. 3d, where n_{dome} is larger, and σ is more packed with resonances, the calculated values are not so sensitive to the choice of interval. There is a transition from slow (Fig. 3a and Fig. 3b) to rapid fluctuations (Fig. 3c and Fig. 3c), which hints at a change of the dynamics present in the scatterer. The high density of resonances we observe is also a feature of a Ericson fluctuations, which are frequently associated with quantum chaotic scattering^{54,55}. To prove that we are in the Ericson regime falls outside the scope of this paper. However, such an investigation would be of interest to the topic.

B. Signatures of chaos in the scattered wave function

In this section we present evidence of chaos by inspecting the scattered wave functions visually. We look for two signatures of chaos in the distribution of the wave function field strength: scars⁵⁶, and scarlets⁵⁷. These signatures provide straightforward and intuitive “litmus tests” for whether chaos is present in a dynamical wave system or not. Scarlets are highly irregular patterns which manifests themselves as wrinkly filaments in the wave function field distribution arising in chaotic systems. Originally scarlets were discussed in the context of quantum chaos, but since then experimental studies have shown the presence of scarlets in other wave systems such as acoustic resonators⁵⁸, and in water waves⁵⁹. Thus, scarlets and scars are believed to be general wave phenomena. As we have come to expect for a chaotic system, Fig. 4c and Fig. 4d show scarlets in the wave function, while Fig. 4a and Fig. 4b show ordered patterns. This indicates that the scattering dynamics in the two latter cases are more regular than chaotic. These are strong indications that the film+dome system undergoes a transition from reg-

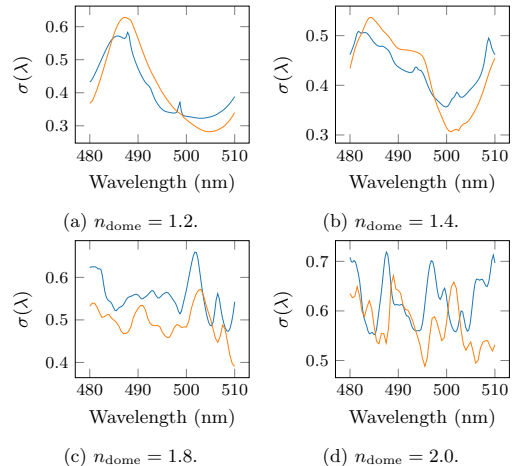


FIG. 3: Comparison of the spectral absorption cross section as calculated by FDTD (blue) and the first channel wave function from the Green’s function approach (orange).

ular to chaotic scattering dynamics, and is in agreement with the findings in Sec. IV A.

Related to the work on eigenvalues and periodic-orbit theory by Gutzwiller⁶⁰, Berry and Tabor^{48,61}, and Balian and Bloch⁶², Heller⁵⁶ found that unstable periodic orbits have a very visible effect on the eigenfunctions of classically chaotic systems. In some wave functions the classical path of the periodic orbits can be seen directly in cases where the fluctuations in the wave function have higher density along the path. Figure 5 shows two wave functions that are scarred by periodic orbits. In Fig. 5b a triangular orbit is scarring the wave function. This scarring surrounds a periodic orbit of similar shape. Additionally, the phase space contains periodic orbits that zig-zag across the x -axis, such as the one shown in Fig 5d. From a ray-trapping perspective, the existence of such orbits can be very important. The rays move in an almost horizontal fashion, resulting in a long path length in the absorbing film. This motion is very desirable in light-trapping schemes. However, the periodic rays of a scattering system cannot be reached by rays coming from outside of the scatterer, but they can get arbitrarily close, thus being effectively trapped considering their finite lifetimes due to absorption.

An arrow-shaped pattern can be seen in Fig. 4b, which resembles a scar. An orbit undergoing a total internal reflection at that angle is not possible for $n_{\text{dome}} = 1.2$. These scar-like patterns are due to ray splitting, i.e. rays that split into a reflected and transmitted component at the boundary at the air-dome interface.

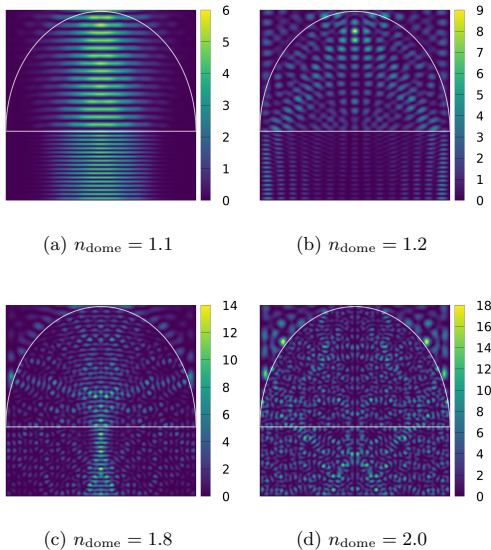


FIG. 4: Irregularities in the scattered wave function become more and more prevalent with increasing n_{dome} . This is a signature of chaos.

C. Transition to chaotic scattering dynamics

Assuming the Bohigas-Giannoni-Schmit conjecture, the distribution of the nearest-neighbor spacings, $P(s)$, of the eigenangles of the eigenvalues $e^{i\epsilon}$ of the S matrix, are universal. We will now look closely at these distributions for the film+dome system as a function of n_{dome} .

When the dome is completely removed from the film+dome model, the system is fully integrable and an analytic closed-form solution can easily be found. An integrable scattering system has fully regular scattering dynamics with uncorrelated levels which follow Poissonian statistics, see Fig. 6a. In Fig. 6b we see that a depression at small s appears. Placing the dome structure on top of the film destroys the integrability of the system, even with a very low index of refraction $n_{\text{dome}} = 1.01$. For values of n_{dome} close to 1, the system is said to be pseudo-integrable. In this case, the system has no classically chaotic counterpart and there is no global universality for $P(s)$ to explain the shape of the distribution⁶³. At $n_{\text{dome}} = 1.1$ and $n_{\text{dome}} = 1.2$ the level distribution is clearly not a Poissonian, but has not fully developed into a Wigner distribution either. There is level repulsion shown in the distributions, but the peak is skewed to the left of what the Wigner surmise predicts.

In the event where an integrable system is perturbed, a smooth transition to mixed dynamics is expected^{44,64,65}. This is contrary to the abrupt transition to chaos of an

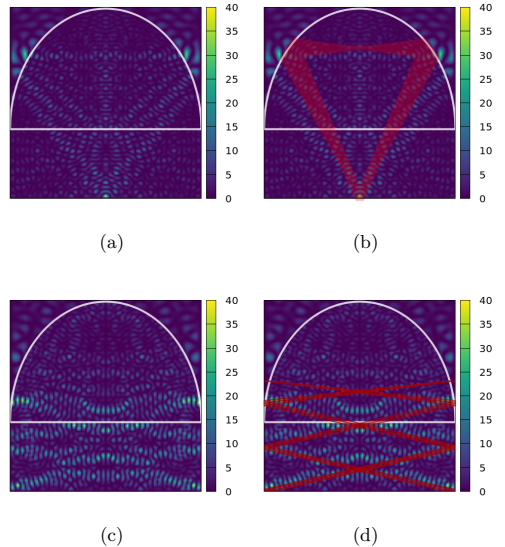


FIG. 5: a) and c) show scars in the scattered wave function, which trace the path of a periodic orbit. In b) and d) the scarred orbits are superposed. The two examples are from the film+dome system with a $1\ \mu\text{m}$ thick film and $n_{\text{dome}} = 2.0$.

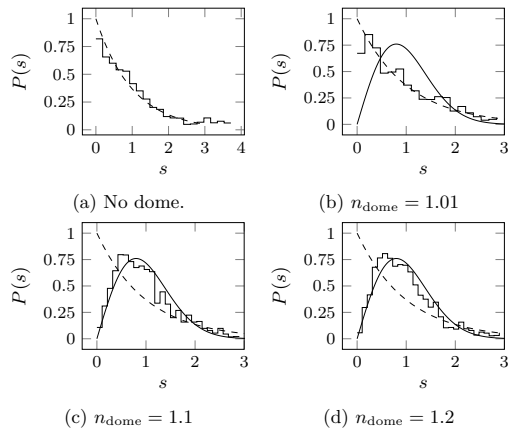


FIG. 6: The dashed line is the Poisson distribution, $P(s) = e^{-s}$ and the solid line is the Wigner surmise. For low values of n_{dome} the film+dome system is pseudo-integrable. At n_{dome} equal to 1.1 and 1.2 the distributions are between the pseudo-integrable and Wigner case.

integrable Hamiltonian that is made ergodic⁶³. We expect our system to be the former. It is therefore difficult to see the onset of chaos by visually comparing the distributions with the Wigner surmise. We apply an objective statistical test to quantify exactly where the transition from regular to chaotic dynamics occurs. The χ^2 goodness of fit test, which we used, is described in more detail in Sec. VII.

The χ^2 test shows the probability of obtaining a histogram that gives a higher χ^2 value when compared to a certain distribution. Lower χ^2 values are better. Both the Berry-Robnik distribution and the Brody distribution were used in the χ^2 test against the histograms of the level statistics. By varying the ‘‘chaoticity parameters’’, $\bar{\rho}$ and ω , for the Berry-Robnik and Brody distributions respectively, in the interval $[0, 1]$, we find the best fitting distributions. Fig. 7 shows histograms of level spacing distributions as n_{dome} is increased in steps of 0.1. The best fitting Berry-Robnik and Brody distributions are plotted on top of the histograms. The level statistics were gathered for wavelengths in the intervals 457 nm to 474 nm and 477 nm to 497 nm for a total of 3129 nearest-neighbor level spacings for the film thickness $2\ \mu\text{m}$. For the $1\ \mu\text{m}$ and $3\ \mu\text{m}$ thick films, only the interval 477 nm to 497 nm with 1620 nearest-neighbor level spacings were used.

First, by visually inspecting Fig. 7, we see that the Berry-Robnik and Brody distributions start to fit better to the histograms for $n_{\text{dome}} = 1.6$ and higher, indicating that the onset of chaos starts around this value. There are statistical fluctuations present in the level statistics histograms due to the sample size and the size of the S matrices. We assume, that a histogram agrees well with the distribution it is compared to, if the probability is higher than some limit. If the probability is lower than the limit, the deviation from the distribution is said to be statistically significant. We chose to use 5% as the limit in our statistical tests. Figure 8 shows the probabilities obtained from the χ^2 test for each value of n_{dome} . The smooth transition of the level statistics from an integrable system (no dome), to the pseudo-integrable, to chaotic, makes it difficult for the histograms to pass strictly the statistical test we apply. We therefore expect only the cases with well-developed chaos to pass the test. The test is passed for n_{dome} values 1.9, 1.6, 1.5 (passing values) and above for the film+dome systems with $1\ \mu\text{m}$, $2\ \mu\text{m}$ and $3\ \mu\text{m}$ thick films, respectively. However, due to the statistical fluctuations present, there are some outliers. The passing values match closely with the critical points 1.85, 1.6, 1.5 for the $1\ \mu\text{m}$, $2\ \mu\text{m}$ and $3\ \mu\text{m}$ thick films, respectively, which are the n_{dome} values where a rapid enhancement of the absorption cross section is observed.

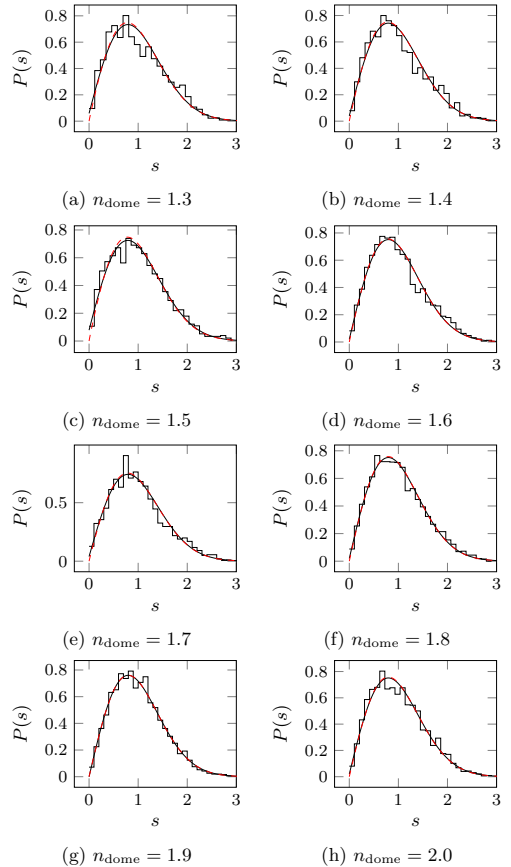


FIG. 7: The histograms shows the level statistics of the different film+dome systems. The smooth black line is the best-fitting Berry-Robnik distribution and the red, dashed line is the best-fitting Brody distribution.

D. Chaos-enhanced light trapping

The autocorrelation function of an S matrix element is defined as

$$\mathcal{A}(\lambda) = \frac{\int \tilde{S}_{i,j}^*(\lambda) \tilde{S}_{i,j}(\lambda + \Delta\lambda) d\lambda}{\int \tilde{S}_{i,j}^*(\lambda) \tilde{S}_{i,j}(\lambda) d\lambda}, \quad (24)$$

where $\tilde{S}_{i,j}(\lambda)$ is the fluctuating part of the S matrix element $S_{i,j}$, i.e., the mean background is removed. It measures the correlation of the S matrix elements as a function of the wavelength of the incoming wave, λ . The half-width at half-maximum of the autocorrelation function in energy is inversely proportional to the classical

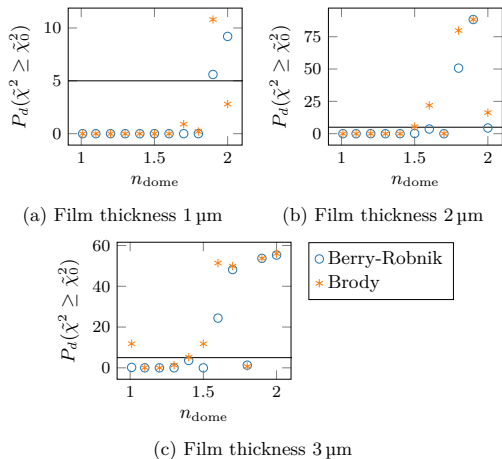


FIG. 8: P_d is the probability of finding a χ^2 higher than χ_0^2 , which corresponds to the best fit. The 5% limit is shown as a horizontal line. The best-fitting Berry-Robnik and Brody distributions are found by maximizing P_d .

lifetime τ of rays⁵⁴,

$$\tau = \frac{1}{v\Delta k}, \quad (25)$$

where v is the speed and

$$\Delta k = \frac{2\pi}{\lambda^2} \Delta\lambda. \quad (26)$$

Thus, from (25) we get an approximation of the lifetime of the rays, $\langle L_A \rangle$, in the classically analog systems to the quantum film+dome system. Using the 2 μm thick film+dome system as an example, we subtract the mean background from the scattering matrix. Then, (24) can be used to calculate the autocorrelation function \mathcal{A} as a function of $\Delta\lambda$. This analysis was done in three different ways, 1) using the $S_{2,1}$ element of the even-parity S matrix of the film+dome system, 2) averaging over 16 off-diagonal S-matrix elements, and 3), averaging over all diagonal S-matrix elements (see open orange, green, and blue circles in Fig. 9a, respectively). The analysis was done for each value of n_{dome} . The autocorrelation functions are shown in Fig. 9b. By tracing 10000 non-Newtonian rays (NNR), the average geometric path length for the classical rays, $\langle L_{\text{NNR}}^{\text{geo}} \rangle$, was also computed (see solid blue line in Fig. 9b). Non-Newtonian rays can split into a transmitted and reflected ray for each encounter with a ray-splitting boundary with the appropriate probability weights according to the Fresnel equations. As a consequence, the trajectories propagate through the film+dome scatterer, and split such that their probability goes towards zero. The average

path lengths computed from the autocorrelation functions, $\langle L_A \rangle$, and classical rays, $\langle L_{\text{NNR}}^{\text{geo}} \rangle$, are increasing as a function of n_{dome} ; they are shown in Fig. 9a. There is remarkably good agreement between the classical ray calculations and the quantum wave calculations.

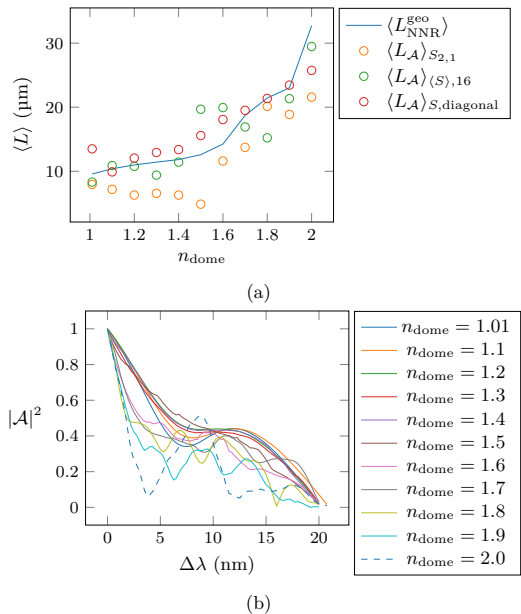


FIG. 9: a) Average geometric path length calculated by ray-tracing 10000 Non-Newtonian rays (blue full line), derived from the width of the autocorrelation function, using $S_{2,1}$ (orange open circles), using an average over 16 off-diagonal S-matrix elements (green open circles), and averaging over all diagonal S-matrix elements (red open circles). b) Autocorrelation function, $|\mathcal{A}(\lambda)|^2$, of $S_{2,4}$. The half-width at half-maximum decreases as n_{dome} increases. This correlates the transition to chaotic dynamics with longer classical path lengths present in the system.

The connection between experimentally optimizing light-trapping by surface structures and the results presented here, is the average path length of rays. Knowing how the average path length of rays depends on various system parameters is very useful, but the average path length can not be measured directly. However, as we have seen, it can be extracted from the autocorrelation function, which can be measured. Thus, the fact that the autocorrelation function can be measured experimentally²⁵ makes it a powerful diagnostic tool that can be used to optimize the light-trapping capabilities of new surface structure designs.

V. CONCLUSION

We have observed the existence of a critical region in n_{dome} where the absorption cross section starts to increase rapidly in a solar cell model with a light-trapping surface structure. By changing the index of refraction in the light-trapping structure, the scattering dynamics of the system makes a transition from regular scattering to the irregular, chaotic scattering regime at a critical value of n_{dome} . We show that there is a three-way correlation between the onset of chaotic scattering, the increase of the average path length of rays in the scatterer, and the increase of the absorption cross section.

The implications are of substantial importance. Researchers are already making thinner solar cells to improve voltage characteristics and lowering the cost, but the lowered efficiency that comes with thin solar cells is a major obstacle, which, to be overcome, demands smart management of light. The three-way correlation shows that chaos can be used as a design guide for computationally prototyping surface structures. All the tools needed to evaluate a given structure and the degree of chaos it induces in a system are readily available. By measuring the autocorrelation function presented, the increase in the average path length can be verified experimentally.

ACKNOWLEDGMENTS

This work was supported by the grant ‘‘Development of a new ray model for understanding the coupling between dielectric spheres for photovoltaics with higher efficiency’’ - No: 250678, financed by The Research Council of Norway. High-performance computing resources were provided by UNINETT Sigma2 through grant No: NN9516K.

VI. APPENDIX A: GREEN'S FUNCTION APPROACH TO SOLVING THE HELMHOLTZ EQUATION

We solve the Helmholtz equation

$$(\nabla^2 + n^2 K^2)\psi = 0 \quad (27)$$

by using the Green's function method. To construct the Green's function we choose eigenfunctions that satisfy the boundary conditions which are defined by our model system. The model is defined in a 2D region where $x \in [0, w]$ and $y \in [0, \infty]$ such that

$$\psi(x, 0) = 0, \quad (28a)$$

$$\psi(0, y) = \psi(w, y). \quad (28b)$$

We choose eigenfunctions on the form

$$\phi_{mk}(x, y) = \mathcal{N}_{mk} \sin\left(\frac{m\pi x}{w}\right) \sin(ky), \quad (29)$$

where $k \in \mathbb{R}$, $m \in \mathbb{I}$ and \mathcal{N}_{mk} is the normalization constant.

The eigenfunctions are normalized:

$$\int_0^w \int_0^\infty \phi_{mk}(x, y) \phi_{m'k'}(x, y)^* dx dy = 1, \quad (30)$$

$$\mathcal{N}_{mk} \mathcal{N}_{m'k'} \int_0^w \int_0^\infty \sin\left(\frac{m\pi x}{w}\right) \sin\left(\frac{m'\pi x}{w}\right) \times \sin(ky) \sin(k'y) dx dy = 1. \quad (31)$$

We can do the integrals separately

$$\int_0^\infty \sin(ky) \sin(k'y) dy = \frac{\pi}{2} \delta(k - k'). \quad (32)$$

The integral

$$\int_0^w \sin\left(\frac{m\pi x}{w}\right) \sin\left(\frac{m'\pi x}{w}\right) dx, \quad (33)$$

or equivalently

$$-\frac{1}{2} \int_0^w \left[\cos\left((m+m')\frac{\pi x}{w}\right) - \cos\left((m-m')\frac{\pi x}{w}\right) \right] dx, \quad (34)$$

can be split into two cases:

$$\frac{1}{2} \int_0^w 1 dx = \frac{w}{2}, \quad m = m', \quad (35)$$

$$-\frac{1}{2} \int_0^w \left[\cos\left((m+m')\frac{\pi x}{w}\right) - \cos\left((m-m')\frac{\pi x}{w}\right) \right] dx = 0, \quad m \neq m'. \quad (36)$$

With $m = m'$ and $k = k'$ the two normalization integrals gives

$$\mathcal{N}_{mk} = \frac{2}{\sqrt{\pi w}}, \quad (37)$$

thus the eigenfunctions are

$$\boxed{\phi_{mk}(x, y) = \frac{2}{\sqrt{\pi w}} \sin\left(\frac{m\pi x}{w}\right) \sin(ky)}. \quad (38)$$

The Green's function is defined as

$$\mathcal{D}_{xy} G(x, x', y, y'; K) = \delta(x - x') \delta(y - y'), \quad (39)$$

where the 2D operator \mathcal{D}_{xy} is

$$\mathcal{D}_{xy} = \frac{\partial^2}{\partial x^2} + \frac{\partial^2}{\partial y^2} + K^2. \quad (40)$$

We can expand the Green's function in terms of the eigenfunctions $\phi_{mk}(x, y)$

$$G(x, x', y, y'; K) = \sum_{m=-\infty}^{\infty} \int_0^{\infty} c_{mk}(x', y') \phi_{mk}(x, y) dk, \quad (41)$$

and find the expansion coefficients $c_{mk}(x', y')$ by doing

$$\mathcal{D}_{xy} G(x, x', y, y'; K) = \delta(x - x') \delta(y - y'), \quad (42)$$

$$\mathcal{D}_{xy} \sum_{m=-\infty}^{\infty} \int_0^{\infty} c_{mk}(x', y') \phi_{mk}(x, y) dk = \delta(x - x') \delta(y - y'). \quad (43)$$

\mathcal{D}_{xy} only operates on ϕ_{mk} so we get

$$\mathcal{D}_{xy} \phi_{mk}(x, y) = \phi_{mk}(x, y) \left(K^2 - \frac{\pi^2 m^2}{w^2} - k^2 \right). \quad (44)$$

Before we insert into (43), we rewrite the delta functions

$$\delta(x - x') = \frac{2}{w} \sum_{m=1}^{\infty} \sin\left(\frac{m\pi x}{w}\right) \sin\left(\frac{m\pi x'}{w}\right), \quad (45)$$

$$\delta(y - y') = \frac{2}{\pi} \int_0^{\infty} \sin(ky) \sin(ky') dk. \quad (46)$$

Now (43) has the form

$$\begin{aligned} & \sum_{m=-\infty}^{\infty} \int_0^{\infty} c_{mk}(x', y') \phi_{mk}(x, y) \left(K^2 - \frac{\pi^2 m^2}{w^2} - k^2 \right) dk = \\ & \frac{4}{\pi w} \sum_{m=-\infty}^{\infty} \sin\left(\frac{m\pi x}{w}\right) \sin\left(\frac{m\pi x'}{w}\right) \int_0^{\infty} \sin(ky) \sin(ky') dk, \end{aligned} \quad (47)$$

and we see directly that

$$c_{mk}(x', y') = \frac{\phi_{mk}(x', y')}{K^2 - \frac{\pi^2 m^2}{w^2} - k^2}. \quad (48)$$

We arrive at the bilinear form of G

$$G(x, x', y, y'; K) = \sum_{m=-\infty}^{\infty} \int_0^{\infty} \frac{\phi_{mk}(x, y) \phi_{mk}(x', y') dk}{K^2 - \frac{\pi^2 m^2}{w^2} - k^2}. \quad (49)$$

Next, we carry out the integral where only the y -dependent part of G contains k , thus the integral we need to consider is

$$\int_0^{\infty} \frac{\sin(ky) \sin(ky') dk}{K^2 - \frac{\pi^2 m^2}{w^2} - k^2 + i\epsilon}, \quad (50)$$

where the $i\epsilon$ is an infinitesimal size added to do the complex integration. Two cases must be considered;

$$K^2 - \frac{\pi^2 m^2}{w^2} > 0, \quad \text{for open channels}, \quad (51)$$

$$K^2 - \frac{\pi^2 m^2}{w^2} < 0, \quad \text{for closed channels}. \quad (52)$$

We let

$$A_m = \sqrt{\frac{\pi^2 m^2}{w^2} - K^2}, \quad (53)$$

$$B_m = \sqrt{K^2 - \frac{\pi^2 m^2}{w^2}}. \quad (54)$$

Since $2 \sin(ky) \sin(ky') = \cos[k(y - y')] - \cos[k(y + y')]$ we only consider the following integrals for the open channel case:

$$\int_0^{\infty} \frac{\cos[k(y - y')]}{B_m^2 - k^2 + i\epsilon} dk = -\frac{\pi i}{2B_m} e^{iB_m|y - y'|}, \quad (55)$$

$$-\int_0^{\infty} \frac{\cos[k(y + y')]}{B_m^2 - k^2 + i\epsilon} dk = -\frac{\pi i}{2B_m} e^{iB_m(y + y')}, \quad (56)$$

and the following for the closed channel case:

$$\int_0^{\infty} \frac{\cos[k(y - y')]}{-A_m^2 - k^2} dk = -\frac{\pi}{2A_m} e^{-A_m|y - y'|}, \quad (57)$$

$$-\int_0^{\infty} \frac{\cos[k(y + y')]}{-A_m^2 - k^2 + i\epsilon} dk = -\frac{\pi}{2A_m} e^{-A_m(y + y')}. \quad (58)$$

The number of open channels, M , is decided by the summation index m . From Eq. (51) we get

$$M = \left\lfloor \frac{Kw}{\pi} \right\rfloor. \quad (59)$$

Now we can write down the complete expression for the

Green's function

$$\begin{aligned}
 G_{open} &= \sum_{m=1}^M \frac{i}{wB_m} \sin\left(\frac{m\pi x}{w}\right) \sin\left(\frac{m\pi x'}{w}\right) \\
 &\quad \times \left[e^{iB_m(y+y')} - e^{iB_m|y-y'|} \right], \\
 G_{closed} &= \sum_{m=M+1}^{\infty} \frac{1}{wA_m} \sin\left(\frac{m\pi x}{w}\right) \sin\left(\frac{m\pi x'}{w}\right) \\
 &\quad \times \left[e^{-A_m(y+y')} - e^{-A_m|y-y'|} \right].
 \end{aligned}$$

(60)

VII. APPENDIX B: BINNING AND χ^2 GOODNESS OF FIT TEST

The χ^2 goodness of fit test was performed as described in Taylor's book *An Introduction to Error Analysis*⁶⁶. For our purposes, eigenangles were extracted from the S matrix samples and then binned before applying the χ^2 test. The bin width was determined using the Freedman-Diaconis rule⁶⁷, i.e. the bin width is dependent on N , the size of the data set. The Freedman-Diaconis bin width b_w is defined as

$$b_w = \frac{2\text{IQR}}{\sqrt[3]{N}}, \quad (61)$$

where IQR is the interquartile range of the data set.

χ^2 is a measure of the agreement between an observed distribution O_k and an expected distribution E_k . It is defined as

$$\chi^2 = \sum_{k=1}^N \frac{(O_k - E_k)^2}{E_k}. \quad (62)$$

In the unlikely event that there is a perfect agreement, χ^2 will be 0. However, if the fit is good, it is expected that χ^2 will be on the same order as N or smaller. If the fit is bad, χ^2 will be much larger than N . In order to say something about the quality of the fit, we look at how likely it is to find some value χ_0^2 for a given data set and expected distribution. Specifically, We calculate the probability for finding a χ^2 greater than the χ_0^2 found from the data. This probability is given as

$$\text{Prob}_d(\tilde{\chi}^2 \geq \tilde{\chi}_0^2) = \frac{2}{2^{d/2}\Gamma(d/2)} \int_{\chi_0}^{\infty} x^{d-1} e^{-x^2/2} dx, \quad (63)$$

where d is the number of degrees of freedom, $d = N - c$, the number of observations minus the number of constraints. $\tilde{\chi}^2 = \chi^2/d$, is called the reduced chi squared.

- ¹International Energy Agency, "IEA a snapshot of global PV," <http://www.iea-pvps.org/index.php?id=266> (2019), accessed: 2019-08-05.
- ²T. Tiedje, E. Yablonovitch, G. D. Cody, and B. G. Brooks, "Limiting efficiency of silicon solar cells," IEEE Transactions on Electron Devices **31**, 711–716 (1984).
- ³L. C. Andreani, A. Bozzola, P. Kowalczewski, M. Liscidini, and L. Redorici, "Silicon solar cells: toward the efficiency limits," Advances in Physics: X **4**, 1548305 (2019), <https://doi.org/10.1080/23746149.2018.1548305>.
- ⁴M. A. Green, Y. Hishikawa, E. D. Dunlop, D. H. Levi, J. Hohl-Ebinger, and A. W. Ho-Baillie, "Solar cell efficiency tables (version 51)," Progress in Photovoltaics: Research and Applications **26**, 3–12 (2018), <https://onlinelibrary.wiley.com/doi/pdf/10.1002/pip.2978>.
- ⁵K. Yoshikawa, H. Kawasaki, W. Yoshida, T. Irie, K. Konishi, K. Nakano, T. Uto, D. Adachi, M. Kanematsu, H. Uzu, and K. Yamamoto, "Silicon heterojunction solar cell with interdigitated back contacts for a photoconversion efficiency over 26%," Nature Energy **2**, 17032 EP – (2017), article.
- ⁶J. Gjessing, E. S. Marstein, and A. Sudbø, "2d back-side diffraction grating for improved light trapping in thin silicon solar cells," Opt. Express **18**, 5481–5495 (2010).
- ⁷J. Gjessing, A. Sudbø, and E. Marstein, "A novel back-side light-trapping structure for thin silicon solar cells," Journal of the European Optical Society - Rapid publications **6** (2011).
- ⁸C. Battaglia, C.-M. Hsu, K. Söderström, J. Escarré, F.-J. Haug, M. Charrière, M. Boccard, M. Despeisse, D. T. L. Alexander, M. Cantoni, Y. Cui, and C. Ballif, "Light trapping in solar cells: Can periodic beat random?" ACS Nano **6**, 2790–2797 (2012), <http://dx.doi.org/10.1021/nn300287j>.
- ⁹P. Kowalczewski, M. Liscidini, and L. C. Andreani, "Light trapping in thin-film solar cells with randomly rough and hybrid textures," Opt. Express **21**, A808–A820 (2013).
- ¹⁰Q. Tang, H. Shen, H. Yao, K. Gao, Y. Jiang, Y. Li, Y. Liu, L. Zhang, Z. Ni, and Q. Wei, "Superiority of random inverted nanopyramid as efficient light trapping structure in ultrathin flexible c-si solar cell," Renewable Energy **133**, 883 – 892 (2019).
- ¹¹Y. Xu and Y. Xuan, "Photon management of full-spectrum solar energy through integrated honeycomb/cone nanostructures," Optics Communications **430**, 440 – 449 (2019).
- ¹²J. Grandidier, D. M. Callahan, J. N. Munday, and H. A. Atwater, "Light absorption enhancement in thin-film solar cells using whispering gallery modes in dielectric nanospheres," Advanced Materials **23**, 1272–1276 (2011).
- ¹³H. A. Atwater and A. Polman, "Plasmonics for improved photovoltaic devices," Nature Materials **9**, 205 (2010), review Article.
- ¹⁴F. L. Pedrotti, L. M. Pedrotti, and L. S. Pedrotti, *Introduction to Optics*, 3rd ed. (Pearson Education, inc., 2007).
- ¹⁵J. M. Seoane and M. A. F. Sanjuán, "New developments in classical chaotic scattering," Reports on Progress in Physics **76**, 016001 (2012).
- ¹⁶E. Ott and T. Tél, "Chaotic scattering: An introduction," Chaos: An Interdisciplinary Journal of Nonlinear Science **3**, 417–426 (1993), <https://doi.org/10.1063/1.165949>.
- ¹⁷R. Blümel and W. P. Reinhardt, *Chaos in Atomic Physics* (Cambridge University Press, 1997).
- ¹⁸P. Cvitanović, R. Artuso, R. Mainieri, G. Tanner, and G. Vattay, *Chaos: Classical and Quantum* (Niels Bohr Inst., Copenhagen, 2016).
- ¹⁹A. Kohler and R. Blümel, "Annular ray-splitting billiard," Physics Letters A **238**, 271–277 (1998).
- ²⁰A. Kohler and R. Blümel, "Signature of periodic lateral-ray orbits in a rectangular ray-splitting billiard," Physics Letters A **247**, 87 – 92 (1998).
- ²¹A. Kohler and R. Blümel, "Test of semiclassical amplitudes for

- quantum ray-splitting systems,” *Phys. Rev. E* **59**, 7228–7230 (1999).
- ²²A. Kohler, G. H. M. Killesreiter, and R. Blümel, “Ray splitting in a class of chaotic triangular step billiards,” *Phys. Rev. E* **56**, 2691–2701 (1997).
- ²³A. Kohler and R. Blümel, “Weyl formulas for quantum ray-splitting billiards,” *Annals of Physics* **267**, 249–280 (1998).
- ²⁴N. Savvitsky, A. Kohler, S. Bauch, R. Blümel, and L. Sirko, “Parametric correlations of the energy levels of ray-splitting billiards,” *Phys. Rev. E* **64**, 036211 (2001).
- ²⁵Y. Hlushchuk, A. Kohler, S. Bauch, L. Sirko, R. Blümel, M. Barth, and H.-J. Stöckmann, “Autocorrelation function of level velocities for ray-splitting billiards,” *Phys. Rev. E* **61**, 366–370 (2000).
- ²⁶L. P. Kadanoff and C. Tang, “Escape from strange repellers,” *Proceedings of the National Academy of Sciences of the United States of America* **81**, 1276–1279 (1984).
- ²⁷P. Gaspard and S. A. Rice, “Scattering from a classically chaotic repeller,” *The Journal of Chemical Physics* **90**, 2225–2241 (1989), <https://doi.org/10.1063/1.456017>.
- ²⁸L. A. Bunimovich, “On the ergodic properties of nowhere dispersing billiards,” *Communications in Mathematical Physics* **65**, 295–312 (1979).
- ²⁹L. A. Bunimovich, “On ergodic properties of certain billiards,” *Functional Analysis and Its Applications* **8**, 254–255 (1974).
- ³⁰E. Yablonoitch, “Statistical ray optics,” *J. Opt. Soc. Am.* **72**, 899–907 (1982).
- ³¹M. Mariano, G. Kozyreff, L. G. Gerling, P. Romero-Gomez, J. Puigdollers, J. Bravo-Abad, and J. Martorell, “Intermittent chaos for ergodic light trapping in a photonic fiber plate,” *Light Sci Appl.* **5**, e16216 (2016).
- ³²E. Seim, A. Kohler, R. Lukacs, M. A. Brandsrud, E. S. Marstein, E. Olsen, and R. Blümel, “Chaos: A new mechanism for enhancing the optical generation rate in optically thin solar cells,” *Chaos: An Interdisciplinary Journal of Nonlinear Science* **29**, 093132 (2019), <https://doi.org/10.1063/1.5111042>.
- ³³M. Brandsrud, E. Seim, R. Lukacs, A. Kohler, E. Marstein, E. Olsen, and R. Blümel, “Exact ray theory for the calculation of the optical generation rate in optically thin solar cells,” *Physica E: Low-dimensional Systems and Nanostructures* **105**, 125 – 138 (2019).
- ³⁴N. Chernov and R. Markarian, *Chaotic billiards* (American Mathematical Soc., 2006).
- ³⁵G. Gallavotti, “Lectures on the billiard,” in *Dynamical Systems, Theory and Applications: Battelle Seattle 1974 Rencontres* (Springer Berlin Heidelberg, Berlin, Heidelberg, 1975) Chap. 7, pp. 236–295.
- ³⁶F. Haake, *Quantum Signatures of Chaos*, 3rd ed. (Springer, Berlin, 2010).
- ³⁷E. P. Wigner, “Characteristic vectors of bordered matrices with infinite dimensions,” *Annals of Mathematics* **62**, 548–564 (1955).
- ³⁸A. M. Lane, R. G. Thomas, and E. P. Wigner, “Giant resonance interpretation of the nucleon-nucleus interaction,” *Phys. Rev.* **98**, 693–701 (1955).
- ³⁹M. L. Mehta, *Random Matrices and the Statistical Theory of Energy Levels*, 2nd ed. (Academic press, 1991).
- ⁴⁰M. V. Berry, “Classical chaos and quantum eigenvalues,” in *Order and Chaos in Nonlinear Physical Systems* (Springer US, Boston, MA, 1988) Chap. 11, pp. 341–348.
- ⁴¹M. L. Mehta and J. Des Cloizeaux, “The probabilities for several consecutive eigenvalues of a random matrix,” *Indian Journal of Pure & Applied Mathematics* **3** (1972).
- ⁴²O. Bohigas, M. J. Giannoni, and C. Schmit, “Characterization of chaotic quantum spectra and universality of level fluctuation laws,” *Phys. Rev. Lett.* **52**, 1–4 (1984).
- ⁴³H.-J. Stöckmann, *Quantum Chaos: An Introduction* (Cambridge University Press, Cambridge, 2000).
- ⁴⁴D. Wintgen and H. Friedrich, “Classical and quantum-mechanical transition between regularity and irregularity in a hamiltonian system,” *Phys. Rev. A* **35**, 1464–1466 (1987).
- ⁴⁵M. V. Berry, M. Tabor, and J. M. Ziman, “Level clustering in the regular spectrum,” *Proceedings of the Royal Society of London. A. Mathematical and Physical Sciences* **356**, 375–394 (1977).
- ⁴⁶G. Casati, B. Chirikov, and I. Guarneri, “Energy-level statistics of integrable quantum systems,” *Physical review letters* **54**, 1350 (1985).
- ⁴⁷S. W. McDonald and A. N. Kaufman, “Spectrum and eigenfunctions for a hamiltonian with stochastic trajectories,” *Phys. Rev. Lett.* **42**, 1189–1191 (1979).
- ⁴⁸M. Berry, “Quantizing a classically ergodic system: Sinai’s billiard and the kkr method,” *Annals of Physics* **131**, 163 – 216 (1981).
- ⁴⁹M. Robnik, “The energy level statistics of hamiltonian systems between integrability and chaos: The semiclassical limit,” *Mathematics and Computers in Simulation* **40**, 159 – 179 (1996).
- ⁵⁰M. V. Berry and M. Robnik, “Semiclassical level spacings when regular and chaotic orbits coexist,” *Journal of Physics A: Mathematical and General* **17**, 2413 (1984).
- ⁵¹T. A. Brody, “A statistical measure for the repulsion of energy levels,” *Lettere al Nuovo Cimento* (1971-1985) **7**, 482–484 (1973).
- ⁵²T. A. Brody, J. Flores, J. B. French, P. A. Mello, A. Pandey, and S. S. M. Wong, “Random-matrix physics: spectrum and strength fluctuations,” *Rev. Mod. Phys.* **53**, 385–479 (1981).
- ⁵³Lumerical Inc., “FDTD Solutions,” lumerical.com (2019).
- ⁵⁴R. Blümel and U. Smilansky, “Classical irregular scattering and its quantum-mechanical implications,” *Phys. Rev. Lett.* **60**, 477–480 (1988).
- ⁵⁵R. Blümel and U. Smilansky, “A simple model for chaotic scattering: Ii. quantum mechanical theory,” *Physica D: Nonlinear Phenomena* **36**, 111–136 (1989).
- ⁵⁶E. J. Heller, “Bound-state eigenfunctions of classically chaotic hamiltonian systems: Scars of periodic orbits,” *Physical Review Letters* **53**, 1515–1518 (1984).
- ⁵⁷P. O’Connor, J. Gehlen, and E. J. Heller, “Properties of random superpositions of plane waves,” *Phys. Rev. Lett.* **58**, 1296–1299 (1987).
- ⁵⁸P. A. Chinnery and V. F. Humphrey, “Experimental visualization of acoustic resonances within a stadium-shaped cavity,” *Physical Review E* **53**, 272 (1996).
- ⁵⁹R. Blümel, I. Davidson, W. Reinhardt, H. Lin, and M. Sharnoff, “Quasilinear ridge structures in water surface waves,” *Physical Review A* **45**, 2641 (1992).
- ⁶⁰M. C. Gutzwiller, “Periodic orbits and classical quantization conditions,” *Journal of Mathematical Physics* **12**, 343–358 (1971), <https://doi.org/10.1063/1.1665596>.
- ⁶¹M. V. Berry, M. Tabor, and J. M. Ziman, “Closed orbits and the regular bound spectrum,” *Proceedings of the Royal Society of London. A. Mathematical and Physical Sciences* **349**, 101–123 (1976), <https://royalsocietypublishing.org/doi/pdf/10.1098/rspa.1976.0062>.
- ⁶²R. Balian and C. Bloch, “Solution of the schrödinger equation in terms of classical paths,” *Annals of Physics* **85**, 514 – 545 (1974).
- ⁶³M. Robnik, “A note on the level spacings distribution of the hamiltonians in the transition region between integrability and chaos,” *Journal of Physics A: Mathematical and General* **20**, L495–L502 (1987).
- ⁶⁴M. Robnik, “Quantising a generic family of billiards with analytic boundaries,” *Journal of Physics A: Mathematical and General* **17**, 1049–1074 (1984).
- ⁶⁵H.-D. Meyer, E. Haller, H. Koppel, and L. S. Cederbaum, “On the connection between irregular trajectories and the distribution of quantum level spacings,” *Journal of Physics A: Mathematical and General* **17**, L831–L836 (1984).
- ⁶⁶J. R. Taylor, *An introduction to error analysis: the study of uncertainties in physical measurements* (University Science Books, 1997).
- ⁶⁷D. Freedman and P. Diaconis, “On the histogram as a density estimator: I2 theory,” *Zeitschrift für Wahrscheinlichkeitstheorie und Verwandte Gebiete* **57**, 453–476 (1981).

Errata

Page	Location on page	Correction
6	Sec. 1.2, line 3	four smaller tasks. to three smaller tasks.
8	Line 15	see Fig 2.2c to see Fig. 2.2b
8	Line 16	see Fig 2.2b to see Fig. 2.2c
8	Line 21	in Fig 2.3 to in Fig. 2.3
9	Line 13	Sec. 2.4 to section 2.4
10-11	Eq. (2.6), (2.7), (2.8)	Film thickness a was corrected to m
11	Eq. (2.9)	$t_l e^{4ink_a} e^{2i\pi} t_r$ to $t_l e^{4ink_a} e^{2i\pi} r_r t_r$
18	Line 10	simulation to simulations
18	Line 16	lifetime is to lifetimes are
19	Caption of Fig. 2.11	Captions for a) and b) have been exchanged
22	Line 4	κ_i to K_i
22	Line 8	K^2 to K_i^2
30	Line 10	in Fig 3.5 to in Fig. 3.5
32	Caption of Fig. 3.8	blue to blue
32	Caption of Fig. 3.8	orange to orange
32	Caption of Fig. 3.8	green to green
32	Caption of Fig. 3.8	red to red

ISBN: 978-82-575-1670-3

ISSN: 1894-6402



Norwegian University
of Life Sciences

Postboks 5003
NO-1432 Ås, Norway
+47 67 23 00 00
www.nmbu.no